VANADIUM DIOXIDE BASED RADIO FREQUENCY TUNABLE DEVICES

Dissertation

Submitted to

The School of Engineering of the

UNIVERSITY OF DAYTON

In Partial Fulfillment of the Requirements for

The Degree of

Doctor of Philosophy in Engineering

By

Kuan-Chang Pan

Dayton, Ohio

December, 2018

VANADIUM DIOXIDE BASED RADIO FREQUENCY TUNABLE DEVICES

Name: Pan, Kuan-Chang

APPROVED BY:

Guru Subramanyam, Ph.D. Advisory Committee Chairman Professor Electrical and Computer Engineering	Partha P. Banerjee, Ph.D. Committee Member Professor and Chair Electro-Optics and Photonics
Monish R. Chatterjee, Ph.D. Committee Member Professor Electrical and Computer Engineering	Robert P. Penno, Ph.D. Committee Member Professor Electrical and Computer Engineering
Robert J. Wilkens, Ph.D., P.E. Associate Dean for Research and Innovation Professor School of Engineering	Eddy M. Rojas, Ph.D., M.A., P.E. Dean, School of Engineering

ABSTRACT

VANADIUM DIOXIDE BASED RADIO FREQUENCY TUNABLE DEVICES

Name: Pan, Kuan-Chang
University of Dayton

Advisor: Dr. Guru Subramanyam

Phase change materials (PCMs) have always been an interesting topic for scientists. The materials with tunable electrical properties can be used in various microwave devices such as antennas, phase shifters and varistors. Vanadium dioxide (VO_2) is a unique phase change material (PCM) that shows a transition from insulator to metal above a transition temperature of 68℃. By doping different ratios of tungsten with vanadium dioxide, the transition temperature of tungsten-doped vanadium dioxide (W-doped VO_2) can be lower than 68 ℃ which gives the researchers more flexibilities for designing tunable radio frequency (RF) devices. Therefore, the purpose of this dissertation is to design tunable microwave devices such as RF switches and antennas using the phase change material (PCM) VO_2 and W-doped VO_2.

This dissertation reports different topics of VO_2 thin films. First, the fabrication process of undoped and W-doped VO_2 thin films. The pulsed laser deposition (PLD) was used to fabricate the undoped, 0.34 at. % W-doped, 0.54 at. % W-doped and 1.1 at. % W-doped VO_2 thin films on sapphire substrates. Second, the measurements and analysis of undoped and W-doped VO_2 thin films. Scanning electron microscope (SEM), X-ray diffraction (XRD) analysis and electrical resistivity of different W-doped VO_2 thin films have been provided. Third, undoped and W-doped VO_2 thin films based RF switches and reconfigurable antennas are reported. The single pole single throw (SPST) switches and reconfigurable antenna have been designed, fabricated and characterized for undoped and W-doped VO_2 thin films integrated into those devices. The SPST switches are designed using coplanar waveguide (CPW) transmission lines, and the switches can be turned on or off by adjusting the temperature. At room temperature (20°C), the switch is in off state, and when the temperature is above 68°C, the switch is in the on state. The return loss (S_{11}) of the switch is less than 1 dB at 20 °C, and it is better than 20 dB at 80°C. The isolation of the switch (S_{21}) is better than 30 dB at 20 °C in the off state, and the insertion loss in the on state is less than 4 dB at 80 °C. The radio frequency (7 GHz) and W-band (93 GHz) CPW reconfigurable antennas have been demonstrated, and the wafers with undoped and tungsten-doped (0.1% to 1% tungsten) VO_2 integrated with these antennas have been fabricated and tested. For the 0.54 at. % W-doped VO_2 thin film based CPW bowtie antenna, the frequency tuning range is from 6.753 GHz with S_{11} -25.25 dB (10℃) to 6.346 GHz with S_{11} -30.26 dB (30℃), and the antenna is inactive when the temperature is above 40℃. For the 93 GHz antenna, when the W-doped VO_2 is in low conductivity, the simulation shows that the resonant frequency of the antenna is at 92.9 GHz with S_{11} -51.4dB. When the W-doped VO_2 is in high conductivity, the resonant frequency shifts to 91.4 GHz with S_{11} -43.03dB.

The analyses of the undoped and W-doped VO_2 thin films have been provided in this dissertation. The simulations and measurements successful demonstrated the tunability and the applications of the undoped and W-doped VO_2 thin films.

Dedicated to my daughter, my wife,
and my parents.

ACKNOWLEDGEMENTS

First, I would like to take this opportunity to express my gratitude to my supervisor and chair of my doctoral committee, Professor Guru Subramanyam who provided the time and resources necessary for the work contained herein, and for directing this dissertation and bringing it to its conclusion with patience and expertise. Professor Guru Subramanyam is an extremely patient and intelligent person. When I have questions, he is always willing to help, and his knowledge always helps me find the best answer and arousing my interest in the field of microwave devices. He also has lots of ideas to create new device structures which can be used in practice. I really want to express my deep appreciation to him.

I would also like to thank my committee members Professor Partha P. Banerjee, Professor Monish R. Chatterjee and Professor Robert P. Penno. They always asked me lots of questions during my qualifier exam and proposal presentation. Without those questions, I would not ask myself to work harder and find the answers for this research. I really appreciate them spending their time and helping me to do better.

I would like to show my appreciation to Dr. Weisong Wang who helped me to get the measured results of the antenna patterns and S parameters from the Wright Patterson Air Force Research Laboratory. Dr. Wang also helped me to complete different designs of RF devices, and I learnt a lot from him. His serious academic attitude always impresses me and gives me the correct direction while doing research.

Also, I would like to thank Dr. Eunsung Shin who helped me to understand the fabrication process and fabricated different ratios of tungsten-doped vanadium dioxide thin-films. Because of his hard work, I had the opportunity to get different types of samples, doing measurements, and analyzing the tungsten-doped vanadium dioxide thin film based devices.

I would also like to thank the former colleagues, Dr. Mark Patterson, Dr. Hai Jiang, Dr. Dustin Brown, Dr. Shu Wang, Dr. Hailing Yue and Mr. Chenhao Zhang for helping me to fabricate the devices, taught me a lot of knowledge about the theory of electromagnetics, and helped me to learn better for the simulation software Keysight ADS and NI AWR.

I also would like to thank all of my group mambers, Kelvin Freeman, Devin Spatz, Liangyu Li, Kaushik Annam and Ayesha Zaman for their time and willingness to be part of this study.

Lastly, I would like to thank my family, my father Wangwanchu Pan, my mother Chinfeng Panpeng, my father in law Chihsun Chen, my mother in law Yuchen Pai and my wife Chiawen Chen. Thanks to all of you for supporting me during my Ph.D. studies and helping me to taking care of me and my daughter, so I can focus on my study.

TABLE OF CONTENTS

LIST OF FIGURES

LIST OF TABLES

CHAPTER I

INTRODUCTION

1.1 Motivation

RF (Radio Frequency) technology is getting important in the data transmission, and people hold the wireless devices almost every day, every minute or even every second. Because of RF systems being used widely, there is one technology that has been developing rapidly as well which is the Internet of Things (IOT). The IOT is the electronics in which computers, software, sensors, smart phones, automobiles and alert system are connected together and enable to exchange data and operator each other in network environment [1-9]. For example, when people are in outside and would like to turn on the air conditioner before coming home, the smart phone can be used to control the air conditioner and turn it on through the network environment [1-9].

The IOT is part of the RF systems, and it has been known that the IOT is based on the wireless communications which is also part of the RF systems. The RF sensors are the important components in the whole RF systems and devices, and those sensors include the RF filters, RF switches and microwave antennas. One of the main reasons why the RF systems getting important is that the devices are able to have extremely large data exchanged in short distance, fast operating speed, small size, lower power consumption and non-linear behavior of the semiconductor components.

It is also known that miniaturized devices and the materials with tunable RF properties have good uses in microwave systems. Recent research results have demonstrated applications using Micro-Electro-Mechanical Systems (MEMS) technology and phase change materials (PCMs) for miniaturized RF components, tunable microwave/RF properties, and structure modification [10-14].

MEMS technologies are small electro-mechanical devices ranging from 1 μm ~ 1cm and have been developed for a long time [11]. The micromechanical components are fabricated using compatible "micromachining" processes and commonly use silicon as the substrate. MEMS technologies can be integrated into sensors, actuators, and electronics [10-11], and have been used in many applications such as switches, phase shifters, and reconfigurable antennas. These MEMS based switches have the characteristics of low insertion loss (<1dB), high isolation (>30dB), very low power consumption, good linearity (third order intercept point > 66dBm), and wide frequency bandwidth (dc-40 GHz) [10-11].

A basic MEMS device is composed of a thin-metal “bridge” membrane that can be electrostatically actuated to the RF signal line by applying a DC bias [11]. For example, several wire antenna segments can be integrated with MEMS switches in such a way that the MEMS switches can adjust the length of the antenna. The MEMS switches are used to connect desired antenna segments, making a varying frequency and it can also vary the radiation pattern at one frequency [10]. Even though MEMS technology based devices have many advantages, but they also have several limitations such a low speed, low power handling capabilities, low mechanical lifetime, high actuation voltage, low reliability, high packaging cost, and fabrication complexity [10].

Materials with radio frequency (RF) properties that can be controlled by external stimuli such as voltage or electric field, magnetic field, incident light, and heat are considered as smart materials, and the RF components integrated with these smart materials can have the tunable electrical properties without changing the structure. Materials that have the characteristic of insulator to metal transition, are also known as phase change materials (PCMs) [12-14].

PCMs have become an important research area based on the insulator to metal transition. PCMs rapidly change from an amorphous state to a crystalline state above a transition temperature of 68℃. These materials can be applied in many areas such as reconfigurable antennas, tunable filters, and other RF components [15-21]. Vanadium dioxide (VO_2) is considered as a PCM according to its characteristic of insulator-metal transition, and its structure is in amorphous or in crystalline can be controlled by temperature [12-14].

1.2 Objectives

There are many sensors that have been applied in multiple fields such like temperature sensors, optical detectors, and pressure sensors. Some of the sensors are related to the temperature, humidity, or moisture, some of them related to visible, ultraviolet, and infrared light, and some of them are related to vibration or pressure [22-23].

Vanadium dioxide (VO_2) is a type of phase change material (PCM) that possesses an insulator to metal transition property, and it was first observed by Morin in 1959 [12] and it started getting well-known since the David Adler and Harvey Brooks published the paper [13] in 1967. Pristine VO_2 has a negative temperature coefficient of resistance, and it undergoes an insulator to metal phase change at a transition temperature of 68 °C.

Compared with MEMS based devices, the VO_2 thin film based devices can achieve the miniaturized components and save more space than MEMS reconfigurable devices. Second, the cost to manufacture the VO_2 thin film based devices is lower than MEMS based devices because there are no mechanical parts in the VO_2 thin film based devices which can lead to significant manufacturing savings. Third, MEMS devices are subject to device fatigue limiting the product lifetime in certain applications. The VO_2 thin film based devices do not have such fatigue concerns. In addition, MEMS devices are subject to coupling between sections. Because MEMS devices use switches to connect or disconnect two pieces of metal, when these metals are close enough, they have a coupling effect even when the switch is off. Table 1.1 summarizes the comparison between MEMS devices and VO_2 thin film based devices.

Table 1.1 Performance comparison between MEMS based devices and VO_2 thin film based devices [10-21]

	MEMS based devices	VO_2 thin film based devices
Size	Average	Small
Cost-manufacture	High	Low
Fatigue	Yes	No
Actuation voltage	High (30V)	Low (~10V)

VO_2 thin film could find broad applications in the domain of active thermal coatings or in those of infrared spectroscopy and sensing due to its negative temperature coefficient of resistance, and it undergoes an insulator to metal phase change at a transition temperature of 68℃. However, it is desirable to have a transition temperature of a PCM closer to room temperature. Therefore, tungsten-doped (W-doped) vanadium dioxide became an interesting research topic due to its transition temperature can be controlled to lower than temperature 68℃ and maintained the transition property by doping different ratios of tungsten with vanadium dioxide. The transition temperature of tungsten-doped vanadium dioxide (W-doped VO_2) can be lower than 68 °C which gives the researchers more flexibilities for designing tunable radio frequency (RF) devices. The objective of this research is to design the VO_2 thin film based RF switches, study the transition property of W-doped VO_2 thin film and design the W-doped VO_2 thin film based RF antennas and W-band antennas.

1.3 Contributions

By doping with different percentages of tungsten into VO_2 in different oxygen pressure conditions during fabrication, the transition temperature of VO_2 thin film can be varied. Based on this research result, undoped and W-doped VO_2 thin films have been fabricated and analyzed, and these thin films based shunt switches, series switches and reconfigurable antennas have been designed, fabricated and measured as well. According to the results related to VO_2 thin film that have been gathered, those research results are divided into four contributions as shown below.

- First, vanadium dioxide: The wafers with undoped and tungsten-doped (0.1% to 1% tungsten) vanadium dioxide W–VO_2 ($V_xW_yO_2$) integrated with these devices have been fabricated by pulse laser deposition (PLD), and the undoped and W-doped

VO_2 thin films were measured and analyzed from the scanning electron microscope (SEM), X-ray diffraction (XRD) and electrical resistivity.

- Second, vanadium oxide thin-film variable resistor based RF switches: The shunt and series RF switches have been discussed, and the measurements have proved the switches can be turned on or off by setting the temperature at 20°C or 80°C. Additional, S-parameters of electrical models of switches have also been used to match the measured S-parameters of the switches in order to find out the resistance of the VO_2 thin films based switches.
- Third, vanadium dioxide thin film based CPW fed reconfigurable bowtie antenna: The resonant frequency of radio frequency CPW fed reconfigurable bowtie antennas has been designed in 7 GHz, and the undoped and W-doped VO_2 thin films integrated with these antennas have been fabricated and tested. The best result was found from the 0.54 at. % W-doped VO_2 thin film based CPW bowtie antenna. For this antenna, the frequency tuning range was measured from 6.753 GHz with S_{11} -25.25 dB (10℃) to 6.346 GHz with S_{11} -30.26 dB (30℃), and then, the antenna completely turned out when the temperature was above 40℃. From the results, it is known that the reconfigurable antenna can be achieved by the VO_2 thin films.
- Fourth, vanadium dioxide thin film based W-band CPW fed reconfigurable patch antenna: For the W-band antenna, the simulations showed that the resonant frequency of the antenna is 92.9 GHz with S_{11} -51.4dB when the W-doped VO_2 is in low conductivity, and the resonant frequency shifts to 91.4 GHz with S_{11} -43.03dB when the W-doped VO_2 is in high conductivity. This simulations demonstrate that the VO_2 thin films can also be used for W-band applications.

1.4 Outline

The majority of the research topic focus on the vanadium dioxide based radio frequency and W-band tunable devices, and this research provides the applications of VO_2 thin films. The fabrication process of the W-doped VO_2 has been discussed in this dissertation, and the literature review in the fundamentals and implementations of coplanar waveguide (CPW), simulation tools NI AWR and Keysight Advanced Design System (ADS) and fabrication process of undoped and W-doped VO_2 thin films are addressed in CHAPTER II.

In CHAPTER III, the undoped and W-doped VO_2 thin films are discussed, and their measured electrical resistivity analyzed.

In CHAPTER IV, the applications of VO_2 thin films based devices, vanadium oxide thin film variable resistor based RF switches are demonstrated, and the S-parameters were measured and compared with simulation results.

In CHAPTER V, vanadium dioxide thin film based CPW fed reconfigurable bowtie antenna is demonstrated. The tunability of the antenna, S-parameters and antenna patterns were simulated and measured.

In CHAPTER VI, the performance of vanadium dioxide thin film based W-band CPW fed reconfigurable patch antenna was analyzed.

In CHAPTER VII, the summary, conclusion and future work of this research are included.

CHAPTER II

LITERATURE REVIEW

2.1 Phase Change Materials

Phase change materials (PCMs) have become an important research topic based on the insulator to metal transition and rapidly changed from an amorphous state to a crystalline state. These materials can be applied in many areas like reconfigurable antennas and tunable filters, and RF components [15-21].

Germanium telluride (GeTe) and vanadium dioxide (VO_2) are two commonly used PCMs and they have the characteristic of the insulation to metal transition, and these materials in amorphous structure or in crystalline structure can be controlled by temperature. The basic concepts of the GeTe and VO_2 will be discussed in following sections.

2.2 Germanium Telluride

Germanium telluride (GeTe) is a phase change material based on the insulator to metal transition, and this phase change phenomena of GeTe is according to the material that its atomic structure can be rapidly changed from an amorphous state to a crystalline state by adjusting the temperature or applying external power [24-25].

The crystal structure of GeTe was first investigated by Schubert and Fricke [26-27] who showed the amorphous in low temperature and rhombohedra in high temperature. GeTe and VO_2 have some similarities such an insulator to metal transition at various temperatures, and both GeTe and VO_2 materials have more than three orders of magnitude change between room temperature and crystallization temperature [28]. Even though the GeTe and VO_2 have such similarities, there are some differences between these two materials. The first difference between the GeTe and VO_2 is the transition temperature of thin film VO_2 is at 68℃, but the GeTe is at round 200ºC [28]. Second, unlike the VO_2 is volatile and requires applied electrical power or external heating to maintain the conductive in “ON state”, the GeTe once turns into conductive state which is in crystallization (200℃), and the status of it will keep the same. When the temperature drops down to room temperature, the GeTe is still in conductive state [29]. The GeTe will change from crystalline state to an amorphous state when the temperature is increased from 20℃ to 200℃ again or applied external power.

In the research published in [26], it shows the resistivity of the GeTe films is from 1.4×103 Ω-cm down to 2.28 Ω-cm in a volatile transition, and from 1.4×103 Ω-cm to 2.43×10-3 Ω-cm in a nonvolatile transition when a thermal stimulus was applied. This research also showed the reflectivity of the film increasing over 30% when GeTe films was crystallized.

In paper [30], the resistivity measurement of GeTe thin films starting at room temperature and heated the thin films up to 330℃. Temperature dependence of the sheet resistance of an 80-nm-thick GeTe film measured in van der Pauw geometry [30] on heating and subsequent cooling to room temperature. The crystallization of the initially amorphous GeTe film at 192℃ into the α-phase [31] is accompanied by a distinct drop of resistivity. The crystalline phase shows a TCR>0 and no changes on annealing are observed. In the beginning of the temperature increasing, the resistivity of GeTe thin films started to decrease smoothly, and it drops by several orders of magnitude when the GeTe thin films reached the onset of crystallization. Again it can be seen that the material goes from entirely crystalline to entirely amorphous with only a slight increase in the reset current [24-33].

2.3 Vanadium Dioxide

Vanadium oxides attract researchers attention recently due to the unique property of insulator to metal transition at various temperatures. Since the discovery of MIT by F. J. Morin at Bell Labs in 1959 [12], the research focus was mainly on VOx or combined multiphase vanadium oxides, and the stable forms of vanadium oxides for microelectronic devices are VO, V_2O_3, VO_2, V_2O_5, and VO_3 [34-39]. Research on electrochromic and thermochromic effects have been studied on VOx for electro-optical device applications, initiated by Honeywell in the 1990s [40]. Since then, this material had become one of the promising materials in current uncooled IR imager manufacturing.

Advancement in thin-film deposition, such as pulsed-laser deposition (PLD) during recent decades provided necessary technologies to lay down single-phase vanadium oxide, and the PLD was used to fabricate the VO_2 thin film in this dissertation. The Figure 2.1 shows the resistivity measurements of vanadium oxide thin films on glass substrate deposited at 35 mTorr.

The SEM pictures of the VO_2 grain size are shown in Figure 2.2, and this VO_2 was fabricated on silicon substrate at each oxygen partial pressure. The different oxygen conditions resulted the different grain sizes in the processed films. According to the SEM pictures, the film using 35-mTorr oxygen partial pressure condition has more uniform and finer grains compared with 25 and 45 mTorr conditions. The films at 25 mTorr, the grain size is ~250 nm, at 35 mTorr condition, the grain size is 100 nm, and at 45-mTorr condition, the grain size is around 300~500 nm [41]. The XRD measurements on each sample are shown in Figure 2.3. The VO_2 films were formed in the 25 and 35 mTorr partial oxygen pressure conditions but not in the 45-mTorr condition because the one formed in the 45-mTorr condition is V_2O_5 instead of VO_2. This XRD results present the VO_2 thin film can be obtained from the oxygen partial pressure of 25 and 35 mTorr conditions. Therefore, electrical measurements of these conditions are necessary to distinguish further [41].

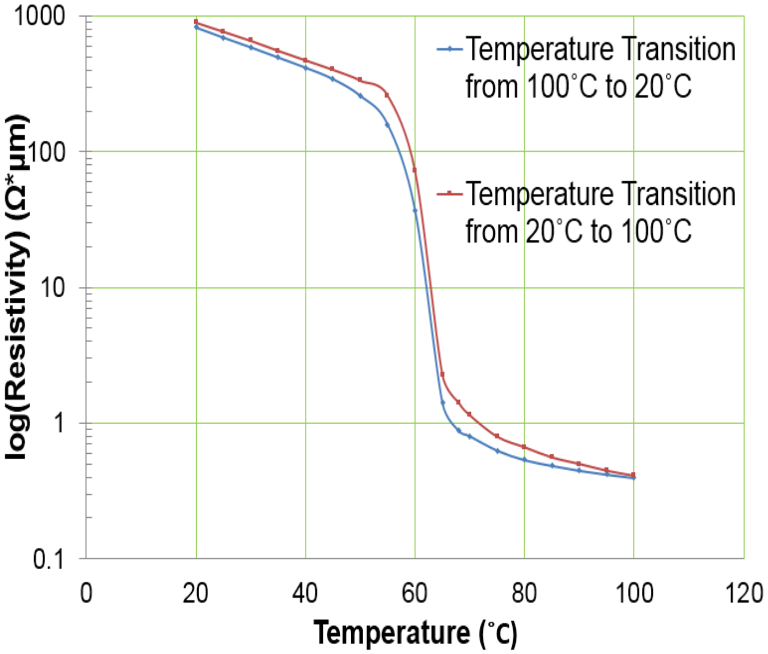

Figure 2.1 Resistivity measurements of vanadium oxide thin films on glass substrate deposited at 35 mTorr [41]

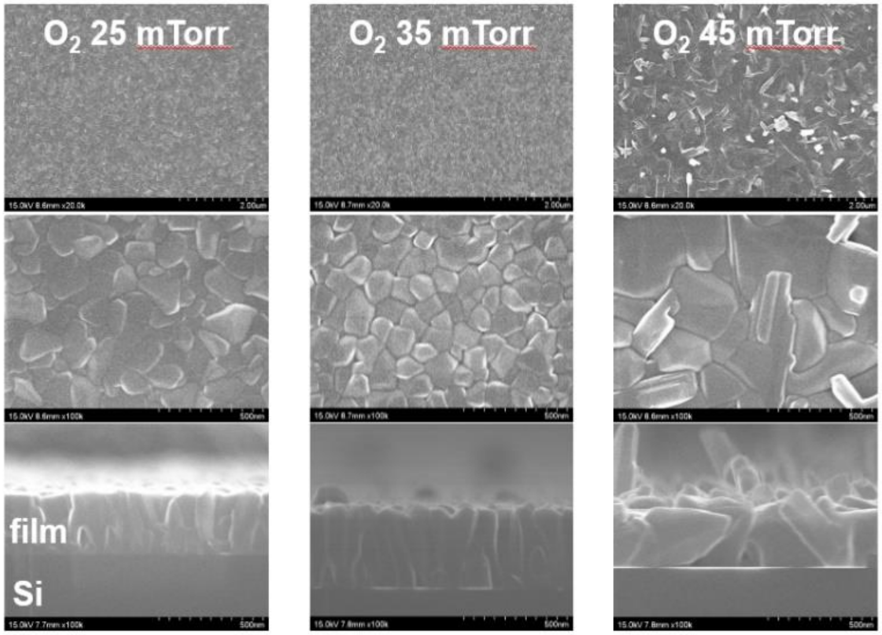

Figure 2.2 The film using 25, 35, 45 mTorr conditions, and the SEM analysis of VO_2 on silicon substrate grain size of oxygen partial pressure [41]

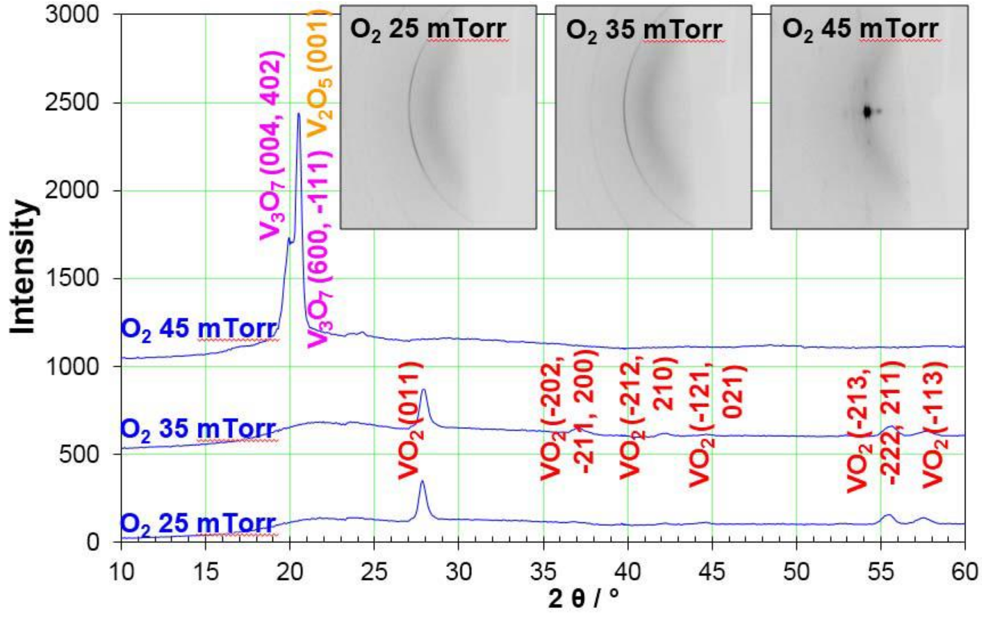

Figure 2.3 XRD measurements of vanadium oxide thin film for different oxygen condition [41]

2.4 Applications in Vanadium Dioxide

Vanadium dioxide (VO_2) is a unique phase change material (PCM) that possesses an insulator to metal transition property. Pristine VO_2 has a negative temperature coefficient of resistance, and it undergoes an insulator to metal phase change at a transition temperature of 68℃. Such a property makes the VO_2 thin films based variable resistor (varistor) a good candidate in reconfigurable electronics to be integrated with different RF devices such as filters, switches, attenuators, actuators and antennas [15-21]. The table 2.1 shows the applications of VO_2 from literature.

Table 2.1 Key References of VO_2 based Devises

Research Sources	**Applications**
(1). R.A. Rodriguez-Solis, "Reconfigurable slotted microstrip patch using VO_2"[15]	VO_2 was used to fill the slot area of the antenna, and the resonant frequency of the antenna would be different when the slot was filled or not [15].
(2) R. A. Rodríguez-Solís, "Cavity Backed Annular Slot Ring Antenna with Reconfigurable Slots Using VO_2" [16]	A cavity-backed annular slot-ring antenna with reconfigurable VO_2 shorts is designed. The resonant frequency of the antenna can be changed from 6.3GHz to 8.25GHz by selectively activating the shorts [16].
(3) T. S. Teeslink, "Reconfigurable Bowtie Antenna Using Metal-Insulator Transition in Vanadium Dioxide", *IEEE Antennas and Wireless Propagation Letters*, VOL. 14, 2015 [17]	VO_2 was used to enable reconfigurable antennas. The dipole length changed by heating and cooling a thin strip of VO_2 [17].
(4) N. Dávila, "Electronically Variable Optical Attenuator Enabled by Self-Sensing in Vanadium Dioxide"[18]	The attenuator is enabled by the strong correlation between the electrical and optical properties in vanadium dioxide thin films across its phase transition [18].

(5) C. Aurelian, “Exploiting the Semiconductor-Metal Phase Transition of VO_2 Materials: a Novel Direction towards Tuneable Devices and Systems for RF-Microwave Applications” [19]	VO_2-based two terminal switch is activated by the current induced heating in a 10% wt. Ni:ta-C pattern situated above it [19].
(6) J. Givernaud, “Tunable band stop filters based on Metal-Insulator Transition in vanadium dioxide thin films” [20]	There are 4 U-shaped resonators in microstrip configuration, and the two extremities of each of the U-type shapes are linked together via a VO_2-based switch in order to achieving the switchable filter [20].
(7) R. Cabrera, “Performance of Electro-Thermally Driven VO_2-Based MEMS Actuators” [21]	The phase transition of VO_2 was induced electro-thermally by resistive heaters monolithically integrated in the MEMS actuator [21].

2.5 Tungsten-Doped Vanadium Dioxide

VO_2 has been observed the insulator to metal transition characteristic at temperature 68℃, and superior resistivity ratio between insulator and metallic phases compared with the other forms of vanadium oxides [42-48]. Therefore, the VO_2 can be used to achieve the flexibility of reconfigurable RF/microwave electronics that can support multiple modes over a wide bandwidth and a variety of communication protocols. These RF/microwave electronic devices include variable capacitors (varactors), variable inductors, and variable resistors (varistors). These adaptive devices could allow the engineers to dynamically match the impedance of power amplifiers, tunable filters, and phase-control circuits [49-50].

However, the transition temperature of VO_2 is 68℃ which is higher than room temperature 25℃. According to this limitation, the tungsten-doped vanadium dioxide (W-doped VO_2) thin film has become another interesting topic for researchers recently due to its transition temperature can be controlled to be closer to room temperature by doping various at. % W in VO_2.

In this research, three different ratios of tungsten-doped vanadium dioxide thin films were used to reach the desired temperature, and these three different W-doped VO_2 films were deposited from the W-wire attached vanadium targets. From the XRD analysis, the measured atomic percentages (at. %) of W in the films deposited with 15, 10, and 5mm of W-wire separation distances were 0.34, 0.54, and 1.1%, and the XRD patterns acquired from the undoped and W-doped VO_2 films deposited on c-cut sapphire wafers are also presented in Figure 2.4.

There are three plots presented in Figure 2.4. First, the patterns shown in Figure 2.4(a) were measured at room temperature, and these patterns indicate that there is no presence of other diffraction peaks besides VO_2 (020) peak. This result indicates that only VO_2 monoclinic (020) crystalline structure exists in the films. Second, the Figure 2.4(b) is the plots of the VO_2 (020) peaks acquired from the films at room temperature. Third, the Figure 2.4 (c) shows the plots of the VO_2 (020) peaks acquired from the films at above phase transition temperature of 90℃, 79℃, 72℃ [51].

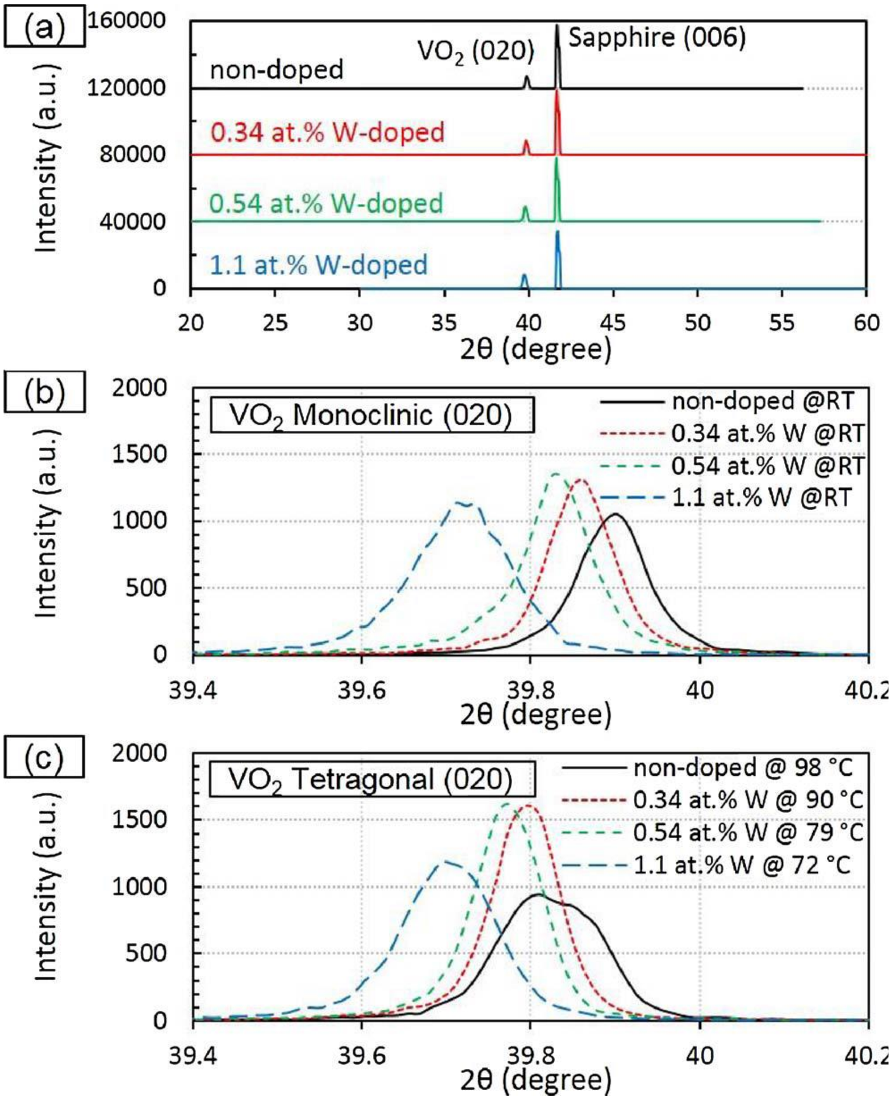

Figure 2.4 XRD measurements of the films deposited on c-cut sapphire: (a) full range patterns at room temperature, and VO_2 (020) peak patterns measured at (b) room temperature and at (c) above phase transition temperature [51]

The SEM analysis of the undoped and W-doped VO_2 grain size is sown in Figure 2.5. These SEM pictures indicate that the grain size of the undoped film was approximately 100 – 200 nm, but the surface roughness and density of the films became smooth and dense as the at.% of W increased. The SEM photo of the 1.1 at.% W-doped film shows this film does not have the characteristics of VO_2, and the behavior is like that of a conductor.

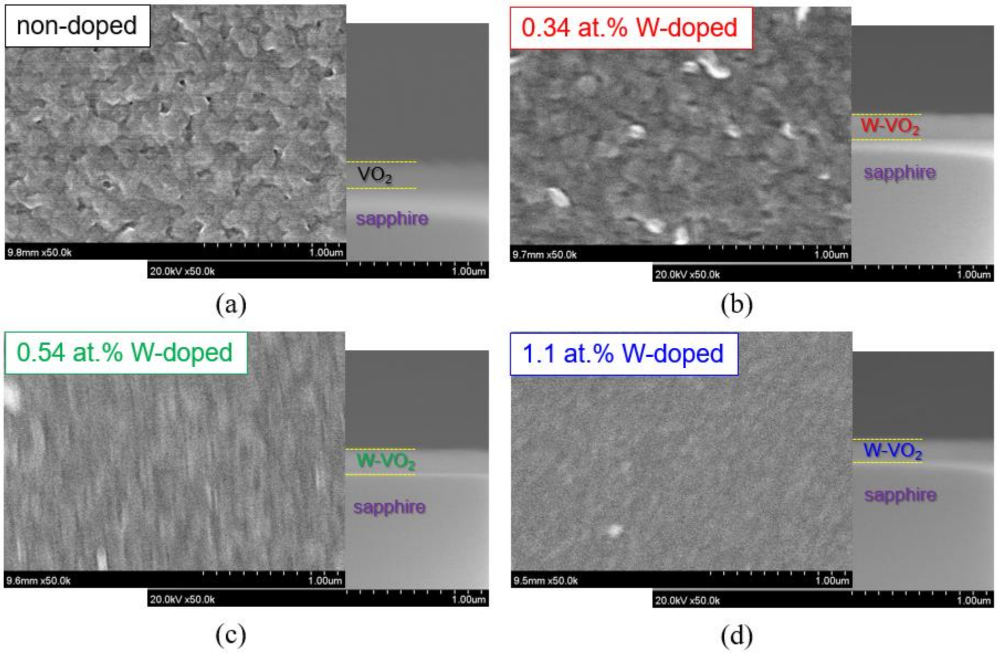

(a) (b)

(c) (d)

Figure 2.5 SEM analysis of the undoped and W-doped VO_2 thin films

In Figure 2.6, the plot proves that incorporation of W into VO_2 crystalline cell leads to a low angle shift of the (020) peak, which suggests the increase of lattice constant b in monoclinic and tetragonal crystalline cells. The plot also shows the linear dependence of calculated cell lattice constant b of the films at room temperature and at above phase transition temperature shows a good consistency with Vegard's law [51].

One thing needed to be addressed is the case of the 1.1 at. % W-doped film. The cell lattice constant b values of it acquired at room temperature (the end of red dot line) and at above the phase transition temperature (the end of blue dot line) are very close. This is an evidence that crystalline structure of this film is almost transformed into tetragonal phase at room temperature [51].

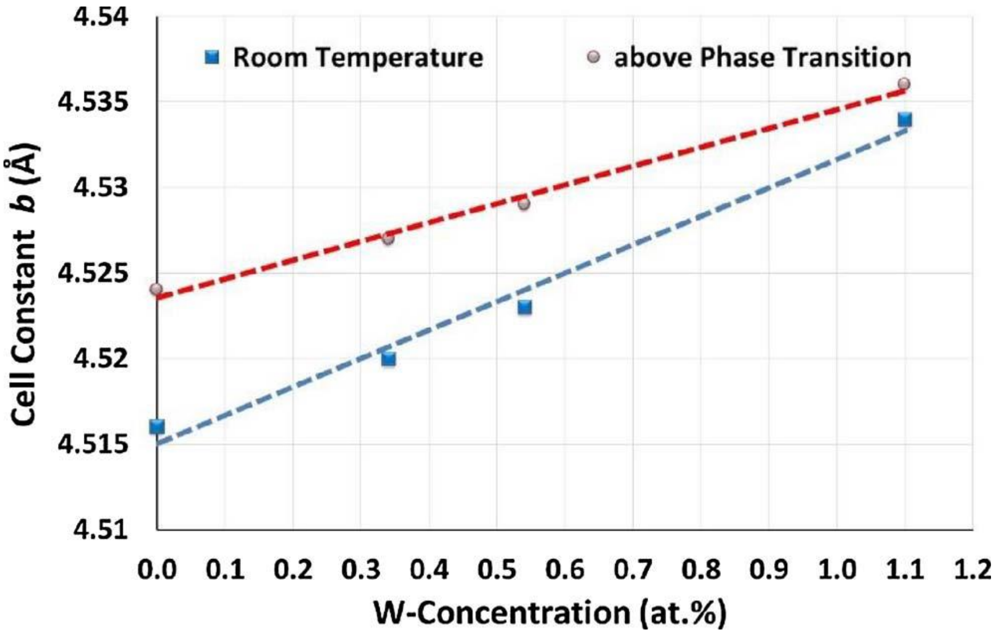

Figure 2.6 Plots of cell lattice constant in W-doped VO_2 thin films [51]

The resistivity plots of various percentages (at. %) of W in the VO_2 thin films is shown in Figure 2.7, and these results were measured from a 2 mm long, 0.1 mm wide, 180 nm thick film stripe of each film, and the measurements were performed in a range of temperatures from 10 to 90 °C. These results clearly show that the phase transition temperature decreases according to the width of transition behavior is broadened as the at. % of W in the film structure increases. Furthermore, the resistivity value of the film measured below the phase transition temperature is also decreased as at. % of W increases. These phenomena are consistent with previous reports [52-55]. The measurements in Figure 2.7 can be summarized in Figure 2.8, the transition temperature versus W concentration of the films. This linear dependence can also support the Vegard’s law. Then, the transition temperature of the 1.1 at. % W-doped VO_2 film near 9°C and the conductivity of the 1.1 at. % W-doped VO_2 film closed to conductor state can be indicated as well [51].

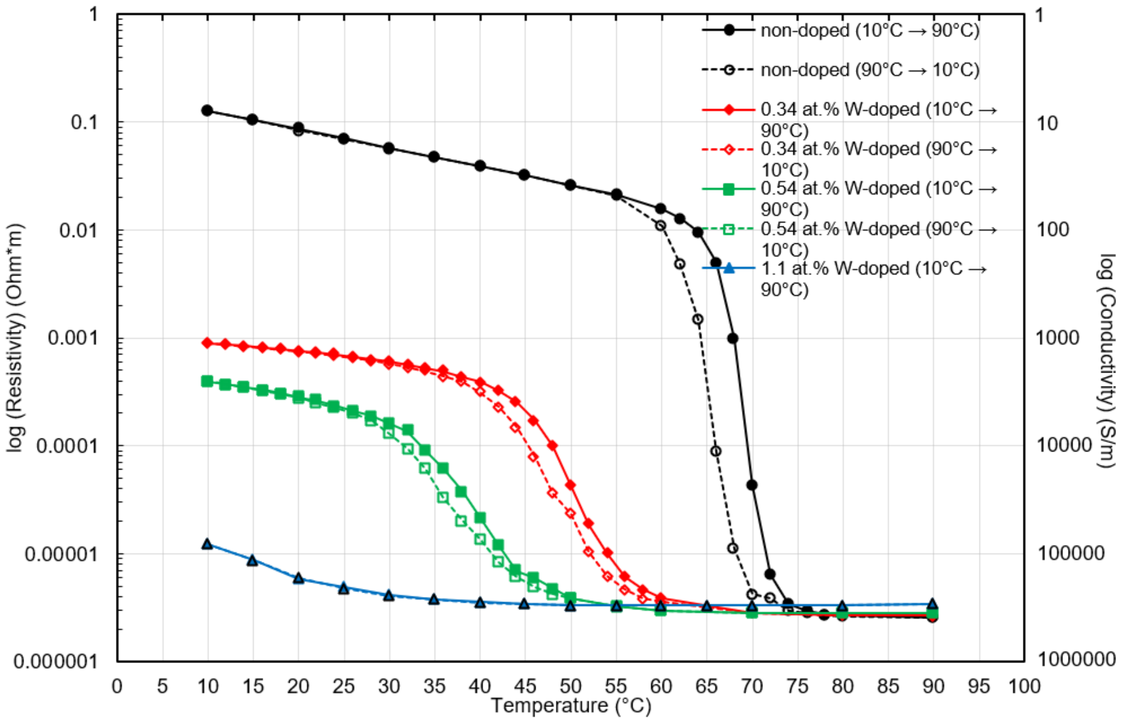

Figure 2.7 Measurements of resistivity versus temperature in different W-doped VO_2 thin-films on sapphire substrate [51]

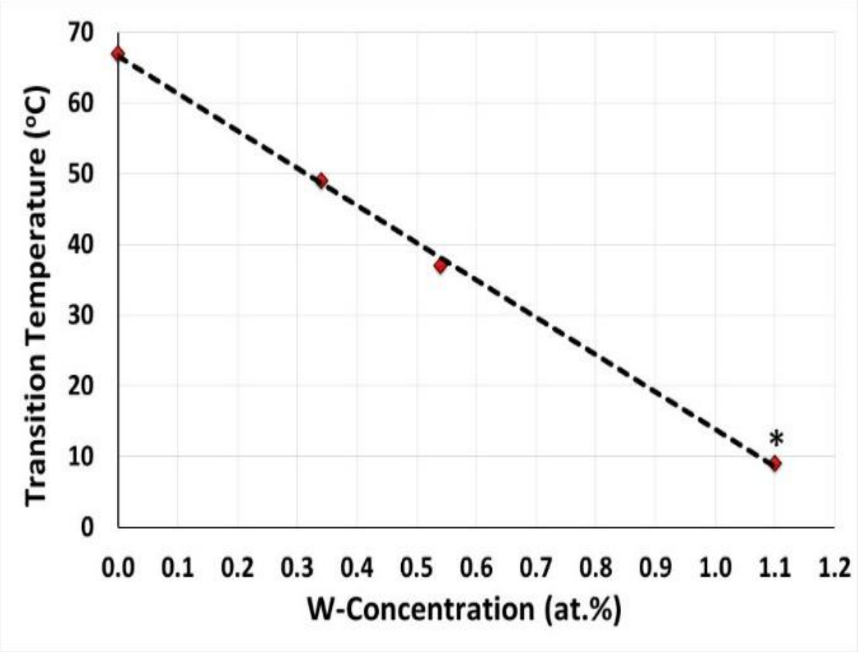

Figure 2.8 Plot of transition temperature as function of W concentration. (*): approximated by Vegard's law [51]

CHAPTER III

METHODOLOGY

3.1 Scattering Parameters

Scattering parameters (S-parameters) are used to describe linear electrical networks, and they are obtained by using matched loads to characterize a linear electrical network. The equations of the reflection coefficient are shown in following, as function of incident voltage (V^{+}) and reflected voltage (V^{-}) of a transmission line: [56]

$$\Gamma = \frac{V^{-}}{V^{+}} \tag{3.1}$$

Γ is reflection coefficient and also related to the impedance Z_L [*11, 24]

$$\Gamma = \frac{Z_L - Z_o}{Z_L + Z_o} \tag{3.2}$$

The equation of voltage standing wave ration (VSWR) shows below:[24]

$$\text{VSWR} = \frac{E_{max}}{E_{min}} = \left(\frac{1+\rho}{1-\rho}\right) \tag{3.3}$$

ρ is the magnitude portion of gamma, the reflection coefficient.

The two-port S parameters are defined for the devices that have two ports, and the definitions of it are shown in the following Figure 3.1 and equations [57]:

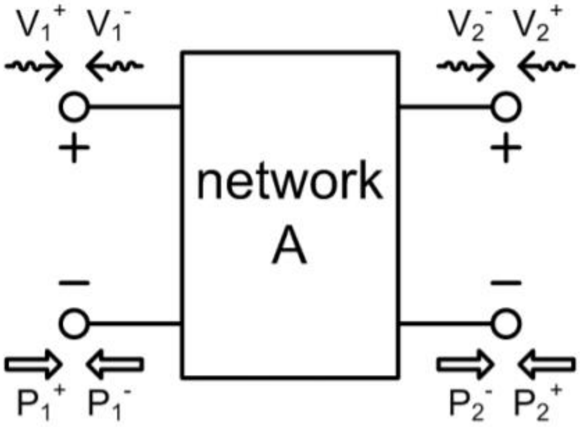

Figure 3.1 Two-port network with incident and reflected field variable definitions [57]

Two port matrix equations shown below [56-57]

$$\begin{bmatrix} V_1^- \\ V_2^- \end{bmatrix} = \begin{bmatrix} S_{11} & S_{12} \\ S_{21} & S_{22} \end{bmatrix} \begin{bmatrix} V_1^+ \\ V_2^+ \end{bmatrix} \tag{3.4}$$

$$V_1^- = S_{11} V_1^+ + S_{12} V_2^+ \tag{3.5}$$

$$V_2^- = S_{21} V_1^+ + S_{22} V_{12}^+ \tag{3.6}$$

The generalized scattering parameters can then be used to relate the incident and reflected waves, where the two port voltages by [56-57]

$$V_1 = V_1^+ + V_1^- \ \ and\ \ V_2 = V_2^+ + V_2^- \tag{3.7}$$

And S_{11} can be derived as below [56-57]

$$S_{11} = \left.\frac{V_1^-}{V_1^+}\right|_{V_2^+=0} = \frac{Reflected}{Incident} \tag{3.8}$$

Then S_{22} can be derived as below [56-57]

$$S_{22} = \left.\frac{V_2^-}{V_2^+}\right|_{V_1^+=0} = \frac{Reflected}{Incident} \tag{3.9}$$

And S_{21} can be derived as below [56-57]

$$S_{21} = \left.\frac{V_2^-}{V_1^+}\right|_{V_2^+=0} = \frac{Trasmitted}{Incident} \tag{3.10}$$

Then S_{12} can be derived as below [56-57]

$$S_{12} = \left.\frac{V_1^-}{V_2^+}\right|_{V_1^+=0} = \frac{Transmitted}{Incident} \tag{3.11}$$

3.2 Coplanar Waveguide

The coplanar waveguide (CPW) structure has been used in this research such as vanadium oxide thin-film variable resistor based-RF switches and undoped and W-doped VO_2 CPW fed patch antennas. The coplanar waveguide includes transmission line consisting of three metal lines above a dielectric substrate, and operates as either coplanar stripline or slotline. The CPW transmission line in Figure 3.2 is a coplanar stripline as it consists of a signal line and two ground planes. The characteristic impedance of the CPW transmission line is controlled by the signal line width, w, and the two gap spacing, S_1 and S_2 seen in Figure 3.2. Typically S_1 equals to S_2 in CPW structure.

The structure of coplanar stripline CPW is the mode utilized hereafter, and will be the type referred to when mentioning CPW. The type of CPW utilized does not use a ground plane on the bottom layer. One advantage of this CPW structure is better dispersion characteristics than microstrip. Additionally, as the three ends (which are signal and two grounds) exist in one plane, no via is needed to ground the transmission line. Because of this, the CPW has lower loss when dealing with shunt elements than microstrip.

Devices using this type of transmission line lie on the top of the dielectric, there may be coupling problems in the packaging of CPW structures. These effects may lead to additional losses at high frequencies. This problem can be solved by adding some ground planes around the transmission line to increase electrical isolation and avoiding noise [58].

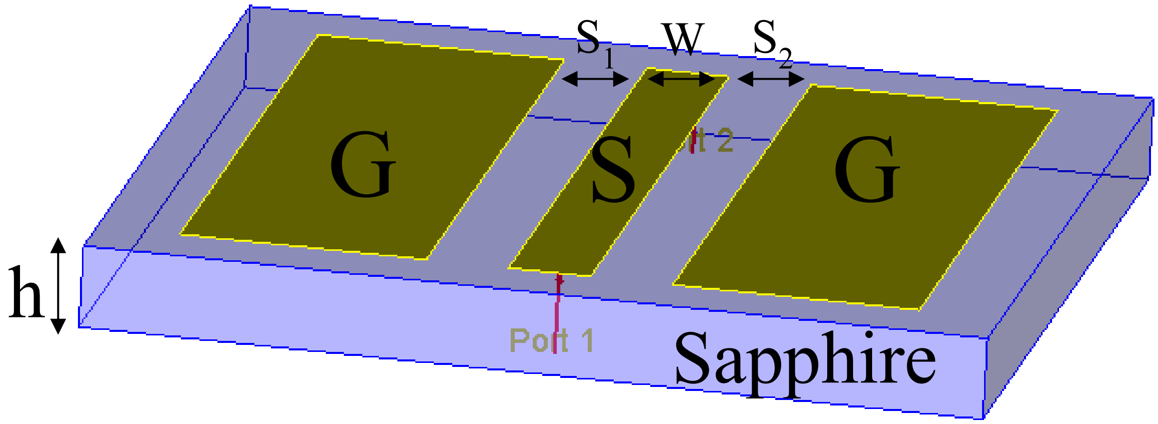

Figure 3.2 The basic structure of coplanar waveguide

3.3 Simulation Tools

The commercial microwave frequency simulation tools, NI AWR and Keysight Advanced Design System (ADS) were used to simulate the S-parameters of possible antenna structures and antenna radiation patterns. AWR and ADS are powerful software tools for simulating microwave devices including microwave antennas.

3.3.1 NI AWR

For AWR, the two 3D-planar EM Simulators, EMSight and AXIEM both are based on Method of Moments (MOM) solvers. AXIEM was used to simulate the switch and antenna, and Method of Moments was used to solve linear partial differential equations. The advantages of MOM are fast solutions because it is only calculating boundary values rather than values throughout the space. It is also efficient with problems with a small surface to volume ratio. However, the disadvantages of this method are that the results are not very accurate because MOM only estimates the outside of the parameter space. Another disadvantage is that it might take more time to do the calculation according to the device size.

For electromagnetic (EM) structure simulation, this process involves defining the enclosure size, material definitions, and dielectric layer definitions. The size of grid needs to be chosen as this affects how many solution points the software has to find. The smaller the size of the grid, the more accurate the results should be. However, decreasing the grid size will increase the simulation time as well. The shape of the antenna can be created after the size of the grid is set. Once the simulation is complete, AWR can provide results of antenna resonant frequencies and radiation patterns.

3.3.2 Keysight ADS

The ADS is an electronic design automation software for RF, microwave, high speed digital, and power electronics applications, and the functions of ADS include X-parameters, 3D EM simulators, radar, satellite and switched-mode power supply designs. ADS provides full, standards-based design and verification with wireless and other application-specific libraries and circuit-system-EM co-simulation in an integrated platform [59]. In this research, the ADS was used to do the EM, S parameters and far field radiation patterns simulation for antennas. For antenna far field, the ADS provides several simulations discussed below:

Polarization: The antenna waveguides can be referenced by the linearly polarized E-plane and H-plane. The E-plane contains electric field vector, and the H-plane contains the magnetic field vector, also the E-plane and H-plane are 90 degree apart. To better analyze the antenna patterns, the polarization can basically be decomposed in ($E_\theta, E_\emptyset$), but in linear polarized antennas, it is much easier to resolve the far-fields into (E_{co}, E_{cross}) which is another way for an antenna measurement set-up. The Eco is defined as colinear, and Ecross implies a component orthogonal to Eco. In Figure 3.3, the θ is the angle in the XZ-plane, $\emptyset$ is the angle in the XY-plane [59-60].

Furthermore, for a vertically polarized antenna, the E-plane usually coincides with the vertical/elevation plane (XZ-plane), and it usually coincides with the horizontal/azimuth plane (XY-plane) in a horizontally polarized antenna [59].

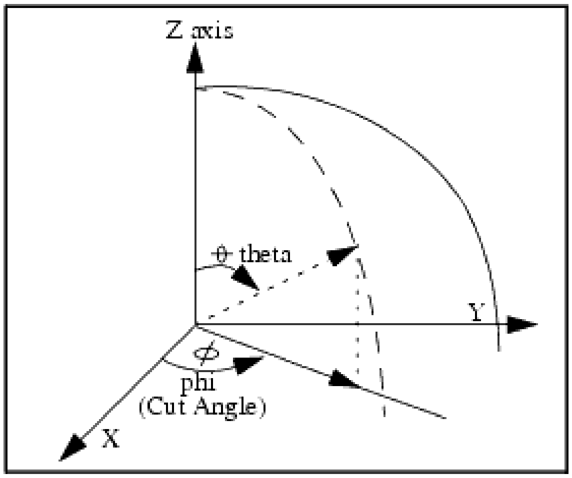

Figure 3.3 X-axis is horizontal, Y-axis is vertical, and Z-axis is normal to the XY-plane [59]

$$H_\varphi = \frac{E_\theta}{\eta} \tag{3.12}$$

$$H_\theta = -\frac{E_\varphi}{\eta} \tag{3.13}$$

$$\eta \; is \; intrinsic \; impedance \; of \; medium = \sqrt{\frac{\mu}{\varepsilon}}\Omega \tag{3.14}$$

$$max\left(\sqrt{\left(|E_\theta|^2 + |E_\varphi|^2\right)}\right) \tag{3.15}$$

Circular Polarization: For circular polarized antennas, the circular polarization axial ratio (AR_{cp}) can be calculated from the left and right hand polarized field components (E_{lhp}, E_{rhp}) as shown in equations (3.16-3.18). Therefore, the axial ratio describes how well the antenna is circular polarized. If the amplitude of the axial ratio equals one and the fields are linearly polarized, the fields are perfectly circularly polarized, and the axial ratio becomes infinite [59-60].

$$E_{lhp} = \frac{1}{\sqrt{2}}\left(E_\theta - jE_\varphi\right) \tag{3.16}$$

$$E_{rhp} = \frac{1}{\sqrt{2}}\left(E_\theta + jE_\varphi\right) \tag{3.17}$$

$$AR_{cp} = \frac{|E_{lhp}|+|E_{rhp}|}{|E_{lhp}|-|E_{rhp}|} \tag{3.18}$$

Linear Polarization: The Figure 3.4 shows that the E_{co} and E_{cross} are in $i\theta$ and $i\varphi\ plane$ and α is the co polarization angle. From the equations (3.19-3.21), a "linear polarization axial ratio" (AR_{lp}) can be derived from the far-fields into a co and cross polarized field E_{co} and E_{cross} [59-60].

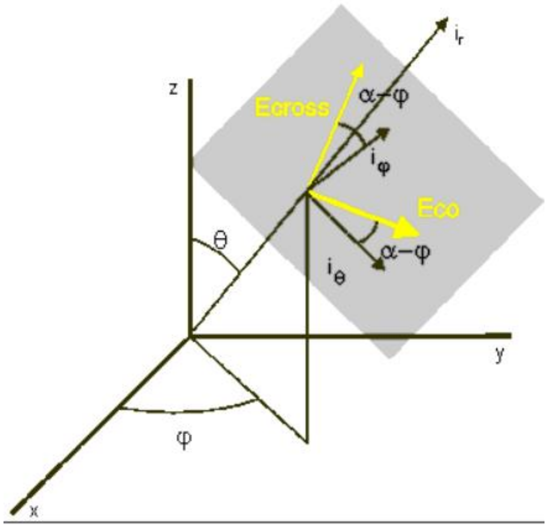

Figure 3.4 $E_{co} and\ E_{cross}$ are in $i\theta\ and\ i\varphi\ plane$ and α is the co-polarization angle [59]

$$E_{co} = E_{\theta}\cos(\alpha - \varphi) + E_{\emptyset}\sin(\alpha - \varphi) \tag{3.19}$$

$$E_{cross} = (-E_{\theta})\sin(\alpha - \varphi) + E_{\emptyset}\cos(\alpha - \varphi) \tag{3.20}$$

$$AR_{lp} = \frac{|E_{co}| + |E_{cross}|}{|E_{co}| - |E_{cross}|} \tag{3.21}$$

Radiation Intensity: Equations 3.22 and 3.23 show the radiation intensity in a certain direction in (W/steradian), and the radiation intensity will be maximal and equals in certain direction as shown in equation 3.24 [59-60].

$$P = \frac{1}{2\eta}\iint \left(|E_{\theta}|^2 + \left|E_{\varphi}\right|^2\right) r^2 d\Omega \tag{3.22}$$

$$U_{(\theta,\varphi)} = \frac{1}{2} RE(E \times H^{*}) r^2 \cdot \hat{\mathrm{r}} \tag{3.23}$$

$$U_{max} = U(\theta_{max}, \varphi_{max}) \tag{3.24}$$

Radiated Power: The total antenna radiated power in Watts is shown in equation 3.25 [59-60].

$$P = \iint U(\theta, \varphi) d\Omega \tag{3.25}$$

Effective Angle: The radiated beam of the antenna comes out from an angle at the antenna, and it is known as solid angle Ω_A, and it can be derived by equation 3.26 [59-60].

$$\Omega_A = \frac{P}{U_{max}} \tag{3.26}$$

Directivity: The antenna directivity can be derived by equation 3.27, and the p is the radiated power [59-60].

$$D = 4\pi \frac{U_{max}}{P} \tag{3.27}$$

Gain: The antenna gain can be derived by equation 3.28. The p is power injected into the antenna [59-60].

$$G = 4\pi \frac{U_{max}}{P} \tag{3.28}$$

3.4 Fabrication

From the related researches, the unique property of insulator to metal transition of vanadium dioxide has been studied. Also, there are different studies that have shown the transition temperature of VO_2 can be modified by doping [61-69]. The materials of tungsten (W) and molybdenum (Mo) are mostly used to dope with vanadium dioxide due to the transition temperature has large shifts to nearer room temperature [61-63]. However, the fabricated method in [66] was doping of VO_2 thin films by sputtering, sol-gel methods and high-energy ion implantation [66]. The pulse laser deposition (PLD) was used to fabricate the VO_2 thin film SPST switch and VO_2/W-doped VO_2 based antenna, and the S-parameters and resistivity of those devices will be analyzed as well.

In this research, the study of achieving high-quality single-phase W-doped VO_2 thin film using the pulse laser deposition (PLD) technique is presented. To obtain pristine

W-doped VO_2 thin film is critical to tunable device fabrication, a typical W-doped VO_2 deposition uses a 248-nm excimer laser, striking a target of vanadium disk, with the laser energy density of 3.5 J/cm^2 at 10-Hz repetition rate. A reactive deposition is performed at a substrate temperature of 500℃ in an optimized oxygen partial pressure. In the pulse laser deposition (PLD) of W-doped VO_2, oxygen partial pressure determines the quality of the film. Three different oxygen pressure conditions were studied, which are 25, 35, and 45 mTorr. Grain size and film composition were compared for these conditions. Samples fabricated on silicon with exactly the same deposition conditions were used, for better imaging in a scanning electron microscope (SEM). X-ray diffraction (XRD) is used as another metrology tool to identify the crystal structure of the W-doped VO_2 film.

Figure 3.5 shows the target of tungsten vanadium (W-doped VO_2) of the PLD system. The tungsten wires are put on the vanadium target. The size of the tungsten wire is 0.2mm diameter, and the gap between tungsten wires is 5mm. The amount of tungsten wires will provide around 0.4% tungsten in W-doped VO_2.

A Pioneer 180 large area PLD system (Neocera) was utilized for fabricating undoped and W-doped VO_2 thin films. In this system, the output of a KrF eximer laser ($\lambda = 248$ nm) was used to ablate the target material, and inside the PLD chamber, the distance between the target and substrate was 50 mm. The laser energy density was set to approximately 2.5 J/cm^2 at the target surface, and the laser repetition rate was kept in 10 Hz. During the deposition process, the ambient oxygen pressure was set as 25 mTorr, and the substrate temperature were fixed to 500 °C [51]. For each undoped and W-doped VO_2 film, the 30,000 laser pulses were used to produce 180 nm thickness films, and C-cut sapphire wafers were used as the substrates. For fabricating the undoped films, a metallic vanadium disk target was used to develop the thin film. On the other hand, for W-doped VO_2 films deposition, the 0.5 mm-dimeter W-wires were set on the surface of the vanadium disk with various separation distances to decide W percentage in the film structures. In this study, three wire separation distances were used, and those were 15, 10, and 5 mm [51].

When the film layer on the wafer was deposited, the film layer was patterned by the photolithography process and dry etched to remove unwanted film area. Then, the standard lift-off process was performed for the thin metal electrode layer (330 nm Au / 20 nm Ti) to fabricate the CPW bowtie antenna structure [51].

X-ray photoelectron spectroscopy (XPS), PHI 5500 spectrometer (Perkin-Elmer) equipped with a hemispherical analyzer was used to determine the atomic compositions of W-doped VO_2 films, and an Mg Kα X-ray source was operated at 350W [51]. A PANalytical X-Pert diffractometer with a hybrid monochromator for Cu Kα_1 radiation ($\lambda = 1.5406$ Å) was used for the X-ray diffraction (XRD) analysis of the undoped and W-doped VO_2 films. The wafer fabrication process is shown in Figure 3.6.

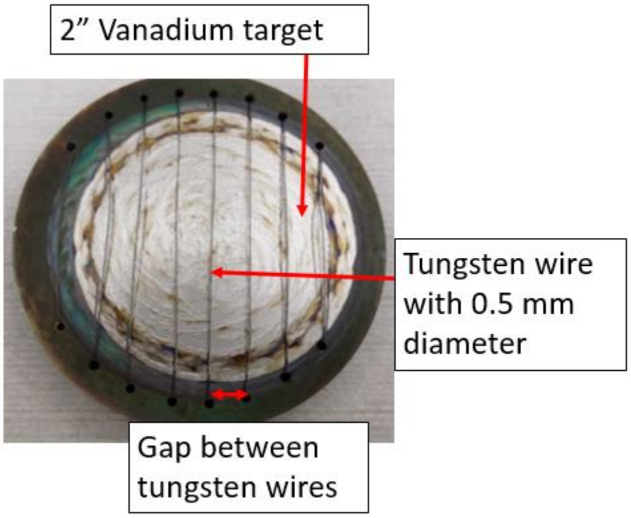

Figure 3.5 A 2" VO_2 target with 0.5mm diameter tungsten wires on it, and the gap between tungsten wires is 5mm

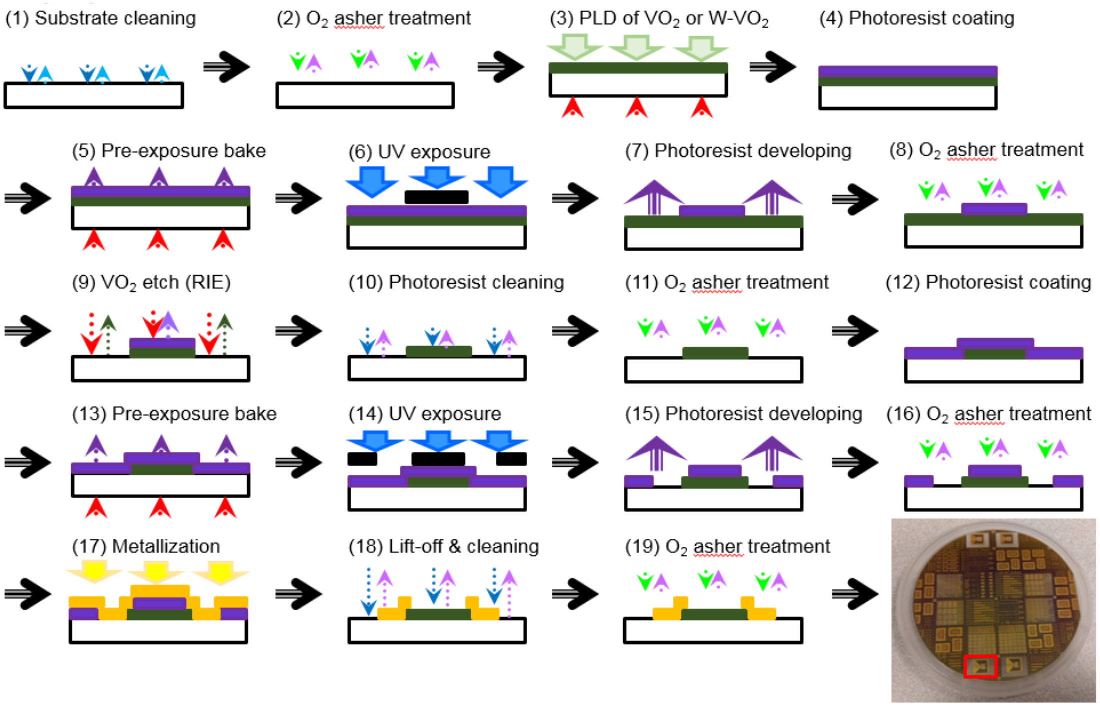

Figure 3.6 Fabrication process of the undoped and W-doped VO_2 thin film based devices, and the red marker shows one of the devices, W-doped VO_2 antenna

3.5 Measurement Set Up

The undoped and tungsten doped vanadium thin films have been fabricated and measured. Next step was to discuss how the resistance of each undoped and W-doped VO_2 thin film was measured.

According to get the resistance of undoped and W-doped VO_2 thin films, the Keithley 2400 source meter, S-725 Micropositioner, Jmicro Technology LMS-2709 microscope and LMS-91A thermal module system as shown in Figure 3.7 were used to measure the devices. The MELCOR MTTC 1410 temperature controller and Thermaltake coolant flow control system were used to control the temperature as shown in Figure 3.8. Vanadium dioxide calibration wire in Figure 3.9 and the series SPST switch in Figure 3.10 were used to find out the resistance of the VO_2/W-doped VO_2 thin films. The dimension of vanadium dioxide calibration wire is L1:0.5mm, W1:0.5mm, L2: 1mm, W2: 0.1mm. The temperature range was measured from 10℃ to 90℃.

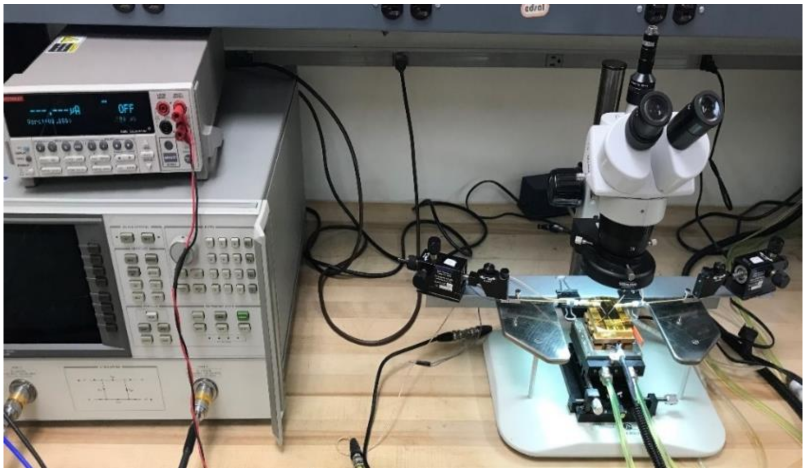

Figure 3.7 Keithley 2400 source meter, Jmicro Technology LMS-2709 microscope, S-725 micropositioner and LMS-91A thermal module system

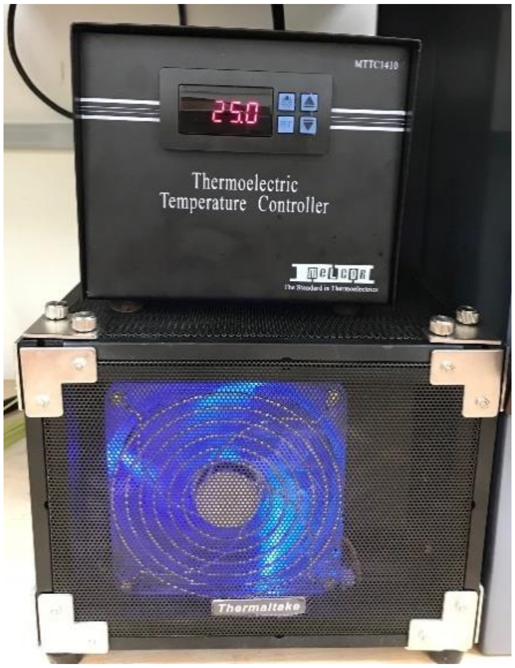

Figure 3.8 MELCOR MTTC 1410 temperature controller and thermaltake coolant flow control system

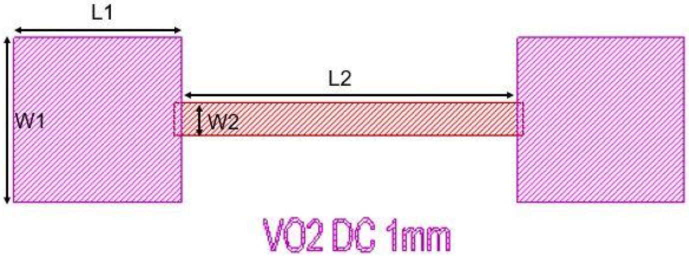

Figure 3.9 Vanadium dioxide calibration wire: The VO_2 wire connected with rectangular metal patch

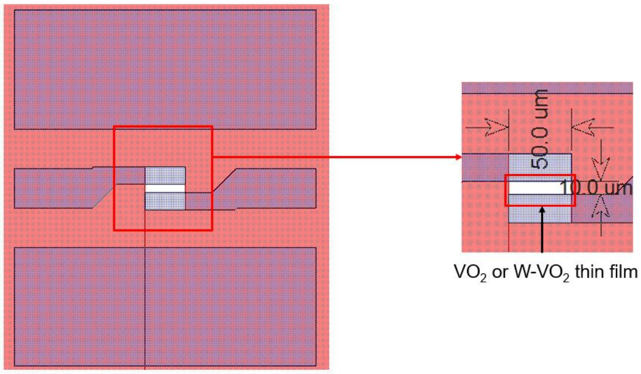

Figure 3.10 The series SPST switch with gap size of $50\mu m \times 10\mu m$

The Figure 3.7 shows the DC bias measurement setup procedure for the VO_2 thin films. The undoped and W-doped VO_2 devices on the 3” wafer was set on the heat station (LMS-91A thermal module system), and the S-725 micropositioner with magnetic base was placed on the metal part on both sides of the measuring station. The S-725 micropositioner is designed primarily for probing targets that are approximately 0.5 mil (12.7 microns) and larger, with 80 TPI resolution. The equations below show how the resistivity and the conductivity σ were calculated after the resistance being measured.

$$\text{Resistivity } \rho = A \times \frac{R}{l} \ (\Omega \cdot \mathrm{m}) \tag{3.29}$$

$$\mathrm{A} = \mathrm{W} \times \text{thickness} \tag{3.30}$$

$$\sigma = \frac{1}{\rho} \ (\mathrm{S/m}) \tag{3.31}$$

W is the width of the piece of VO_2/W-doped VO_2;

R is the electrical resistance of a uniform specimen of VO_2/W-doped VO_2;

l is the length of the piece of VO_2/W-doped VO_2;

A is the cross-sectional area of VO_2/W-doped VO_2

CHAPTER IV

VANADIUM OXIDE THIN FILM VARIABLE RESISTOR BASED RF SWITCHES

4.1 The Introduction of Vanadium Oxide Thin-Film Variable Resistor based RF Switches

The VO_2 thin film has been applied in many applications like reconfigurable antennas, actuators and tunable filters [15-21]. Those RF devices are achieved based on unique insulator to metal transition of VO_2 at the critical temperature of 68 ℃.

A common method in modern semiconductor devices to activate or deactivate switchable devices is by moving parts of the devices. One such implementation is micro-electro-mechanical-systems (MEMS) [70-71]. The MEMS device is actively controlled by adjusting the parts to connect or disconnect with each other. A basic MEMS device is composed of a thin-metal “bridge” membrane that can be electrostatically actuated to the RF signal line by applying a DC bias [70-71]. Even though MEMS devices have many advantages such as low insertion loss (<1dB), high isolation (>30dB), very low power consumption, good linearity (third order intercept point > 66dBm), and wide frequency bandwidth (dc-40 GHz), but they also have several limitations such as low speed, low power handling capabilities, low mechanical lifetime, high actuation voltage, low reliability, high packaging cost, and fabrication complexity [70-71]. Therefore, it is desired to have a switchable antenna that can be actively controlled without physically altering the antenna.

RF or microwave switches are commonly used in microwave system to control the RF signal to go through transmission lines between devices, especially in microwave test systems, they allow the signal routing between instruments and devices under test (DUT). Incorporating a switch into a switch matrix system enables engineers to route signals from multiple instruments to single or multiple DUTs. Therefore, those switches can help engineers to control the signal going through different routes, and allows multiple tests to be performed with the same setup, eliminating the need for frequent connects and disconnects the cables or connectors. This also help the engineers to protect the testing equipment.

The VO_2 property used in this research focuses on varistor RF/microwave applications. Currently, the resistance change in terms of the insulator to metal transition material has been researched [72-74]. The resistance of VO_2 has been measured in different kinds of experiments. First, the resistance of VO_2 was measured at hydrostatic pressures up to 2 GPa and room temperature using electric-field-induced resistance switching of VO_2 planar-type junctions [75]. Second, the VO_2 was fabricated in number of parallel strip patterns in the varistor, and the resistance of the VO_2 thin film has been measured [76]. Third, the resistance of the VO_2 was measured by VO_2 thin-film-based RF shunt resonator, and the VO_2 thin film was deposited as shunt resistance in this device [77].

4.2 The Design of VO_2 Thin Film based Shunt RF Switch

There are two types Vanadium Oxide Thin-Film Variable Resistor Based- RF Switches will be discussed in this research. First type is VO_2 thin film based shunt RF switch, and this type of switch has been published by Dr. Guru Subramanyam in [77], and the structure of VO_2 thin film based shunt RF switch is shown in Figure 4.1.

The overall dimension of this CPW shunt RF switch is $300 \times 450\mu m^2$. The width of the transmission of this switch is $50\mu m$, and the gap between the ground and signal line is $50\mu m$. The VO_2 thin film is located under the transmission line, and connect to the ground as shown in Figure 4.1. The substrate is sapphire with $500\mu m$ thickness, and the thickness of the VO2 thin film is $0.18\mu m$. The thickness of the metal is $0.35\mu m$.

At room temperature, the VO_2 thin film acts like insulator, therefore the signal will go through the transmission line. In this state, the switch is in on status. When the temperature increases to above 68℃, the VO_2 thin film acts like conductor, and it will allow the signal line connect to ground. In this state, the switch is in off state, and there is not much signal can go to the output port. The Figure 4.2 shows that the schematic model of the VO_2 thin film based shunt RF switch.

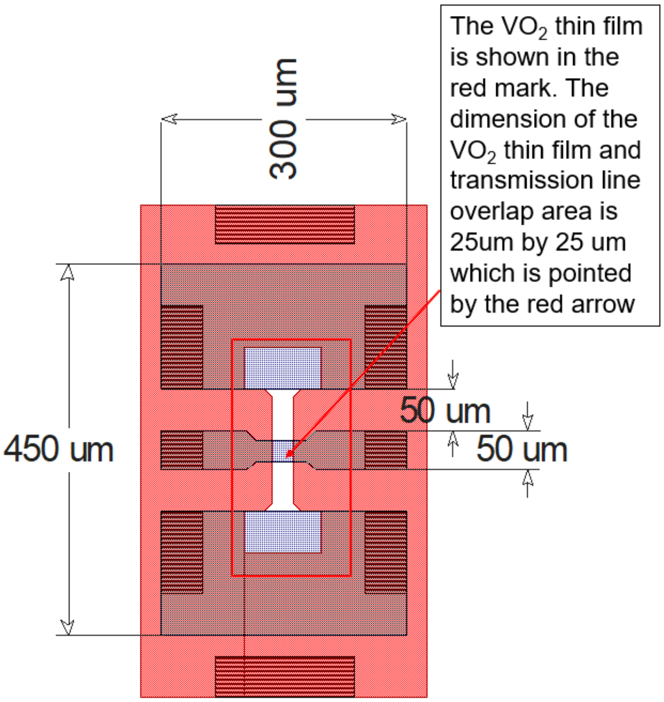

The VO_2 thin film is shown in the red mark. The dimension of the VO_2 thin film and transmission line overlap area is 25um by 25 um which is pointed by the red arrow

Figure 4.1 Top view of the VO_2 thin film based shunt RF switch, and the VO_2 thin film is beneath the signal line

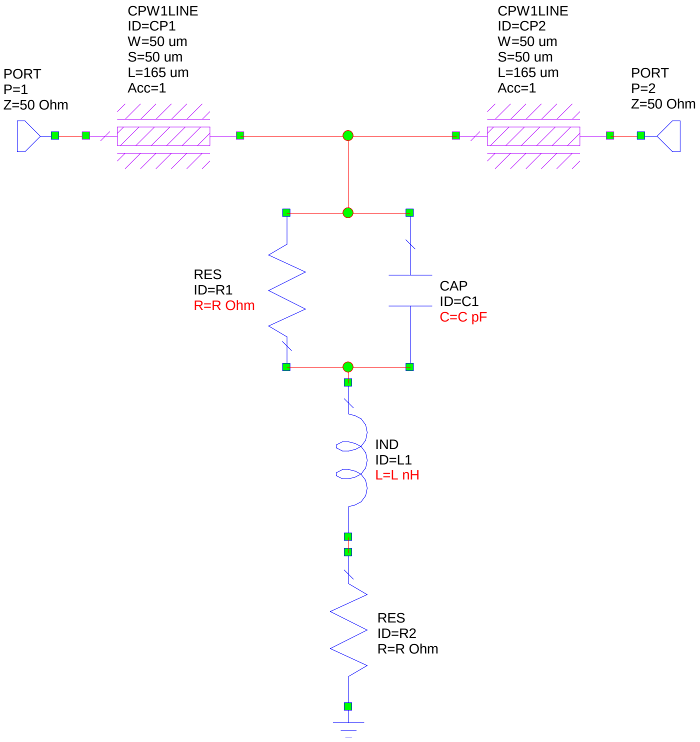

Figure 4.2 The schematic model of the VO_2 thin film based shunt RF switch

4.3 Measurements of the VO_2 Thin Film based Shunt RF Switch

The VO_2 thin film based shunt RF switches have been fabricated and measured in this research, and the measured results were shown in Figure 4.3 and 4.4. The Figure 4.3 shows the measured S_{11} at 20℃ and 80℃, and the Figure 4.4 shows the measured S_{21} at 20℃ and 80℃.

When the shunt RF switch is at 20℃, the VO_2 thin film is in insulator state. Therefore, the signal can go through from input port to output port. In this temperature condition, the switch is in on state. From the measurements in Figure 4.3 show that the S_{11} is around -21.96dB, and measured S_{21} in Figure 4.4 is around -0.91dB at 20℃. The measurements prove that the switch is in on state.

When the temperature increased to 80℃, the VO_2 thin film is in conductor state. In this temperature condition, ground and the signal line are connected together by the VO_2 thin film. Therefore, the signal goes back to ground, the switch now acts as off status. In Figure 4.3, the S_{11} is around -0.177dB, and S_{21} in Figure 4.4 is around -22.75dB. The measurements prove that the switch is in off state. The measured S_{21} and S_{11} clearly show the switching performance of the VO_2 thin film based shunt RF switch.

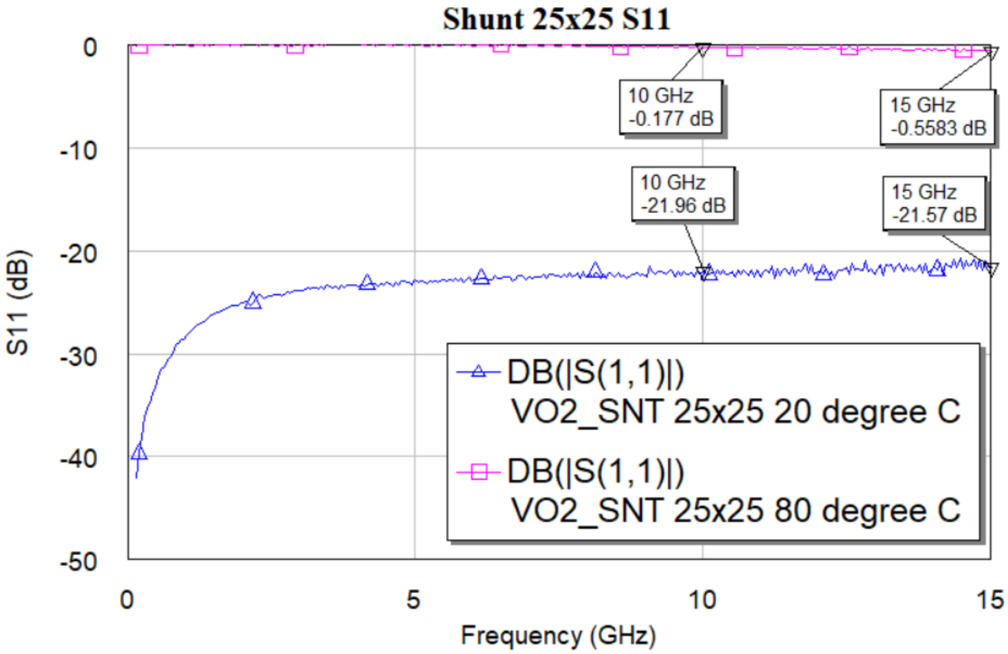

Figure 4.3 Measured S_{11} of VO_2 thin film based shunt RF switch at temperatures of 20℃ and 80℃

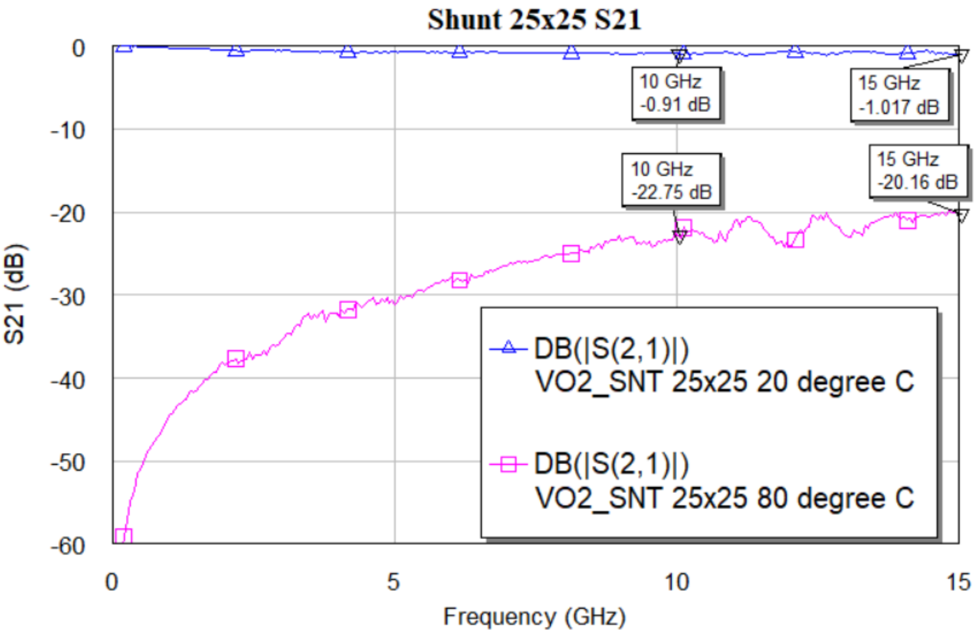

Figure 4.4 Measured S_{21} of VO_2 thin film based shunt RF switch at temperatures of 20℃ and 80℃

4.4 The Design of Series Single-Pole-Single-Throw Switch Devices

The other type of VO_2 thin film based switch is Series Single-Pole-Single-Throw Switch Devices. In this research, the study of achieving high-quality single-phase VO_2 thin film using the PLD technique is presented. A single-pole single-throw (SPST) device has been used as another example to demonstrate the effect of the VO_2 thin film in the RF device performance [41].

Series single-pole single-throw (SPST) switches with integrated VO_2 thin films were designed, fabricated, and tested. The overall size of the device is 380 μm × 600 μm. A series SPST switch is designed with the VO_2 thin film as well. The series SPST switch is implemented in a coplanar waveguide (CPW) transmission-line configuration. A coupled line structure is formed in the middle of the signal line of the CPW, with the VO_2 thin film designed to bridge between input and output signal lines.

At room temperature, the VO_2 film acts like an insulator making the device OFF. At temperatures above 68℃, the VO_2 film becomes a conductor, allowing signal to go through. For better impedance matching, the switch is designed to work with a transmission line characteristic impedance of 50 Ω.

The small rectangular dark region in the middle of Figure. 4.5 is the VO_2 thin-film layer introduced in the coupling gap of the input/output signal lines. The platinum (Pt) heating coil is introduced on the top of the VO_2 thin film using a SiO_2 isolation layer. The heating coil is shown as a meandering line (green). The marked G, S, G (stands for ground, signal, ground) in Figure 4.5 are part of the CPW line conductor, typically made of Au. The layers of the VO_2 thin-film switch are VO_2/Au/SiO_2/Pt on a sapphire substrate, shown in Figure 4.6, with the Pt layer as the top layer. The corresponding thicknesses are 0.35 μm for VO_2, 0.5 μm for Au, 0.3 μm for SiO_2, and 0.1 μm for Pt. The thickness of the sapphire substrate is 500 μm.

The Figure 4.7 shows the SPST switches without Pt heating coil. From the measurements, the SPST switch without heating coil works better than the switch with heating coil. The measurements between the switches with heating coil and without heating coil will be discussed in the measurement section.

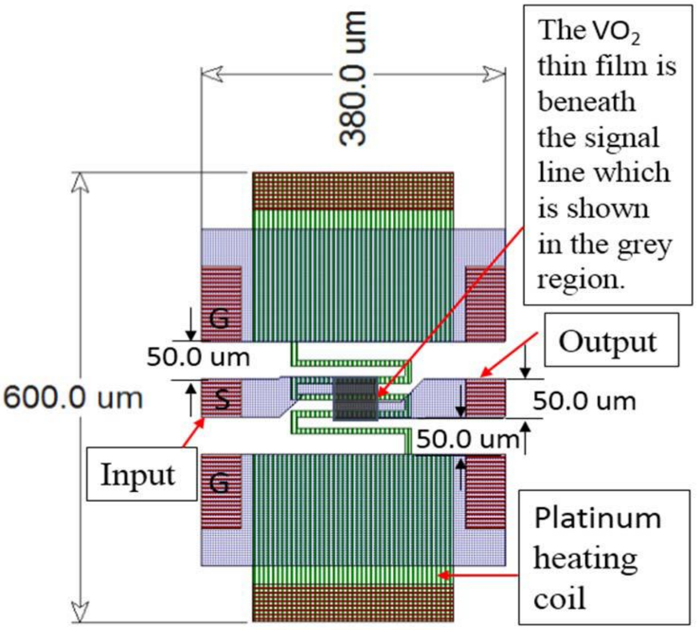

Figure 4.5 Top view of the VO_2 thin-film series SPST switch, showing the CPW structure. The VO_2 thin film is beneath the signal line, which is shown in the dark region, and this switch has 50-μm width and 10-μm gap between coupled lines [41]

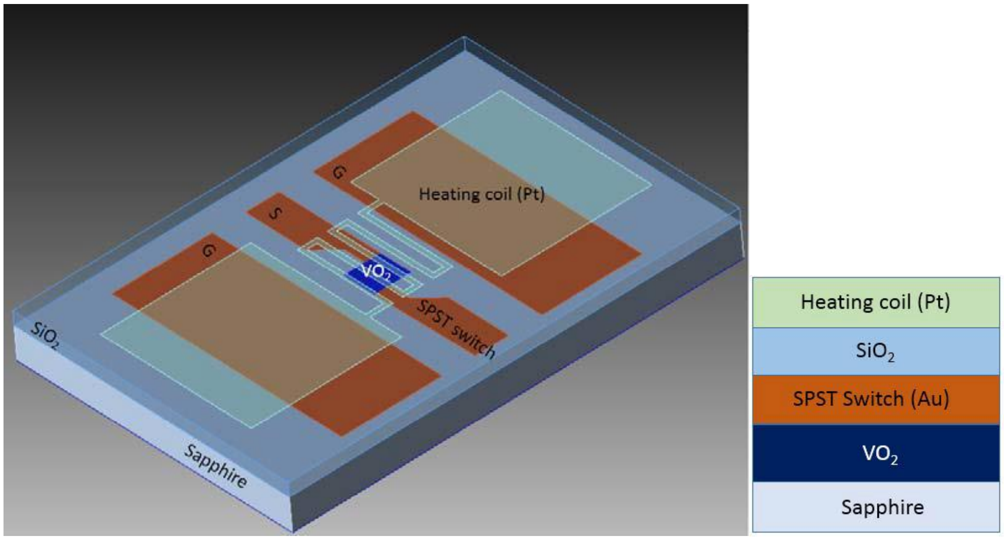

Figure. 4.6 (a) Top view of layers of the VO_2 thin-film switch. (b) Cross-sectional view showing the Pt heating coil on the top layer, then SiO_2, Au, VO_2, and sapphire substrate [41]

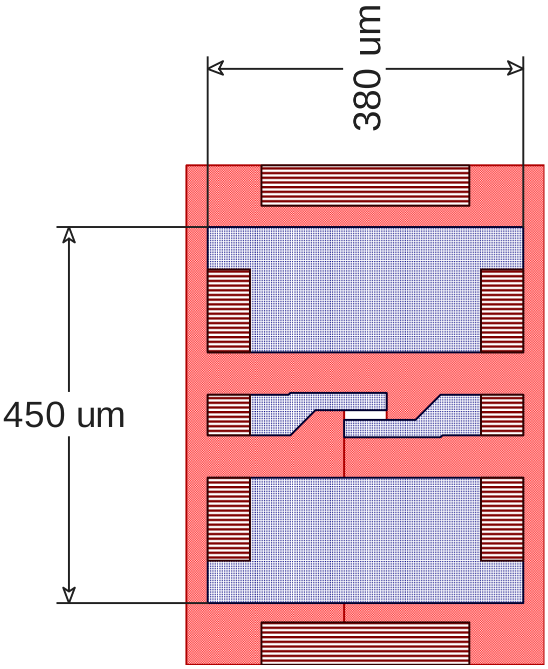

Figure 4.7 The structure of the SPST switch without SiO_2 and heating coil Pt layers. The overall dimension is 380 μm × 450 μm

4.5 Measurements of Series Single-Pole-Single-Throw Switch Devices

The measured results show that the resistivity of the VO_2 films is substrate dependent as well. Compared with glass substrates, sapphire substrate has even better phase transition performance with less hysteresis between room temperature and high temperature [41]. Therefore, for the better quality, sapphire substrate was selected to fabricate the RF devices in this research.

The VO_2 thin-film series SPST switch is a multilayered device. To carefully study the VO_2 performance throughout the fabrication process, the measurements were separated into two stages. The first stage was to measure the S-parameter only when VO_2 and Au layers were deposited. Figure 4.1 shows the structure of the SPST with the SiO_2 and the Pt heating coil layer.

The measured S_{11} is greater than −1 dB at 20℃, and it is less than −20 dB at 80℃, as shown in Figure 4.8. The measured S_{21} is less than −30 dB at 20℃, and it is greater than −4 dB at 80℃, as shown in Figure 4.9. When the temperature was at 20℃, VO_2 acted like an insulator, and the RF signal would not pass through the transmission line. When the temperature was increased to 80℃, the VO_2 acted like a conductor, and most input signal was able to pass through it. The VO_2 thin-film series SPST switch showed that the phase transition was achieved by integrating the VO_2 thin film with the SPST switch [41].

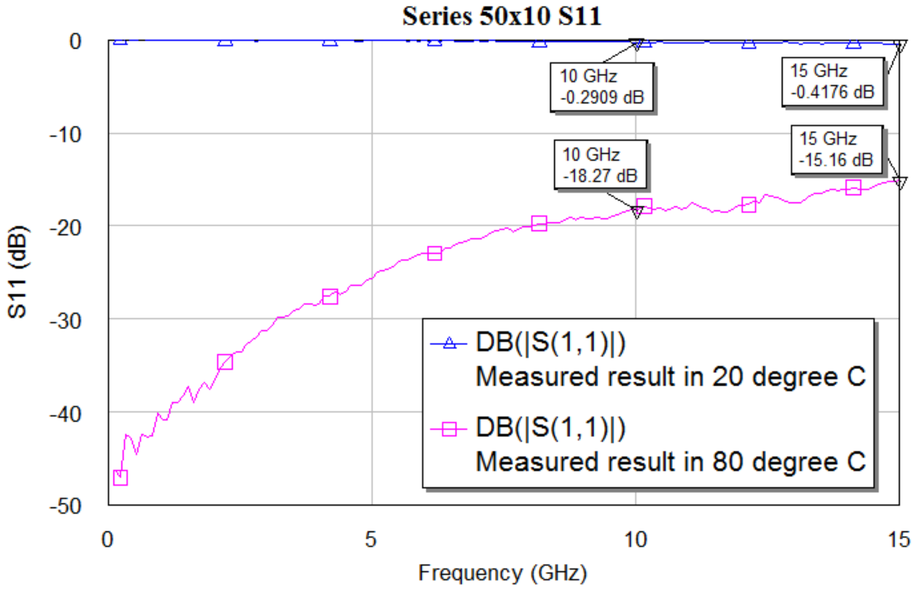

Figure 4.8 Measured S_{11} of VO_2 coupled line series SPST switch without SiO_2 and heating coil Pt layers at temperatures of 20℃ and 80℃ [41]

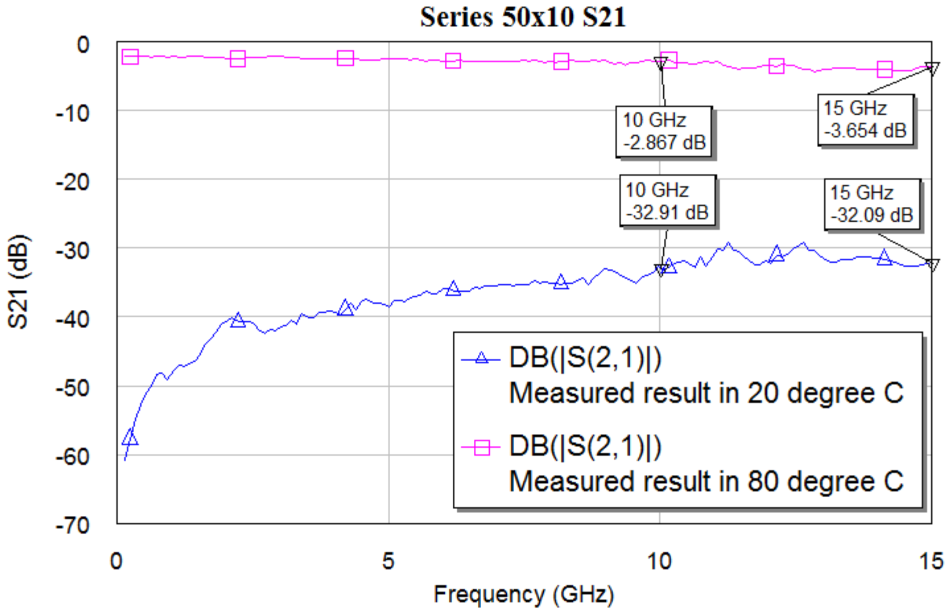

Figure 4.9 Measured S_{21} of VO_2 coupled line series SPST switch without SiO_2 and heating coil Pt layers at temperatures of 20℃ and 80℃ [41]

The next step was to measure the S-parameters when VO_2, Au, SiO_2, and Pt layers were deposited. Figure 4.10 shows the SiO_2 and Pt heating coil layers have been fabricated with the series SPST switch. The measured result of the S_{11} is worsened at 20°C, and it is below −15 dB at 80°C, as shown in Figure 4.10. The S_{21} is less than −20 dB at 20°C, and it is greater than −5 dB at 80°C, as shown in Figure 4.11.

Compared to the measured S_{11} and S_{21} in the first stage, the measured results of S_{11} with SiO_2 and Pt layers are ~6 dB worse than the measured S_{11} without SiO_2 layer, and the measured results of S_{21} with SiO_2 and Pt layers are ~10 dB worse than the measured S_{21} without SiO_2 layer. Therefore, such experimental results have showed that the addition of SiO_2 has some negative effect on the performance of VO_2. However, the XRD measurement on the substrate at this stage shows no sign of VO_2 crystal structure change. Further study will be conducted on understanding the effects of SiO_2 deposition on VO_2.

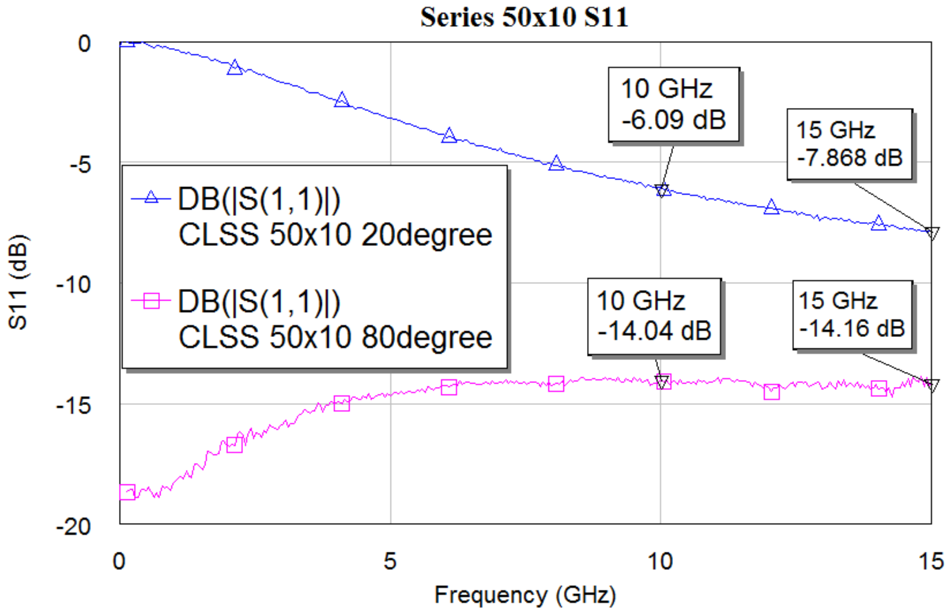

Figure 4.10 Measured S_{11} of VO_2 coupled line SPST switch with SiO_2 and heating coil Pt layers at temperatures of 20℃ and 80℃ [41]

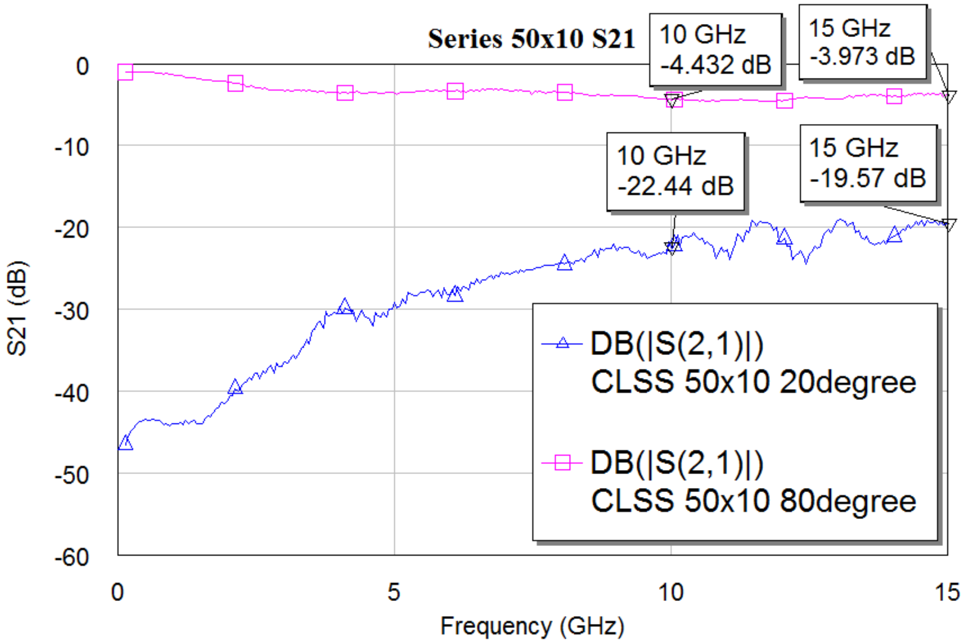

Figure 4.11 Measured S_{21} of VO_2 coupled line SPST switch with SiO_2 and heating coil Pt layers at temperatures of 20℃ and 80℃ [41]

4.6 Electrical Models

The electrical model in Figure 4.12 is used to match the S_{11} and S_{21} at 20℃. The resistor R3 in this electrical model is used to determine the resistance of VO_2 thin-film varistor, and the capacitor C_3 is used to represent the capacitance between the transmission lines. The resistance of VO_2 is ~73.3 kΩ, and the capacitance of C_3 is 0.0058 pF in the insulating state of VO_2 at 20℃. The capacitors of C_1, C_2 and the resistors of R_1, R_2 represent the capacitance and resistance between the signal line and the ground plan of the CPW structure. The corresponding capacitance of C_1 is 0.033 pF and C_2 is 0.237 pF, and the resistance of R_1 is 784 Ω and R_2 is 867 Ω based on fabricated device structure. The matched results are shown in Figure 4.13.

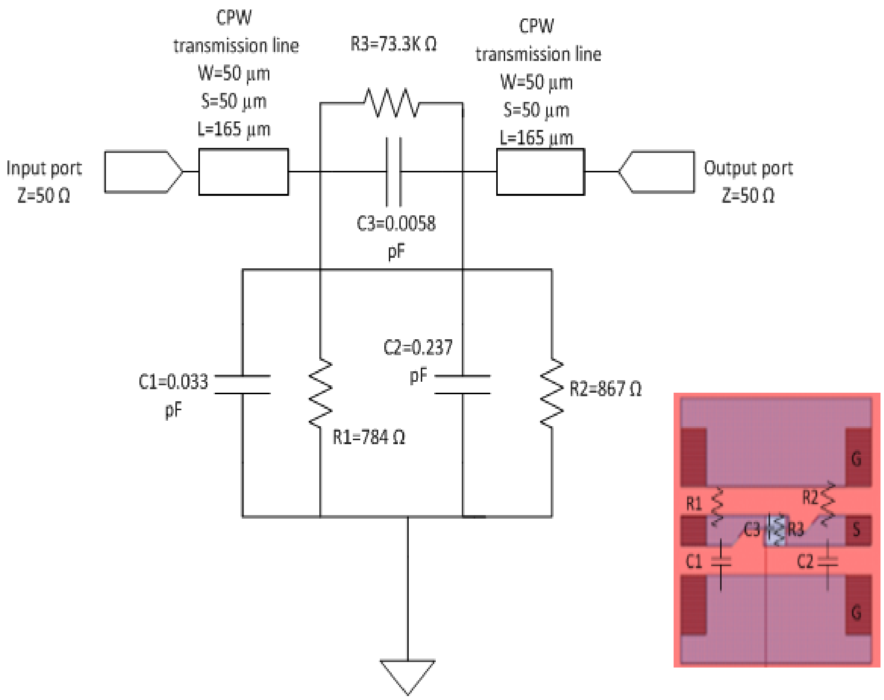

Figure 4.12 S_{11} and S_{21} of electrical model matching results for 20℃ [41]

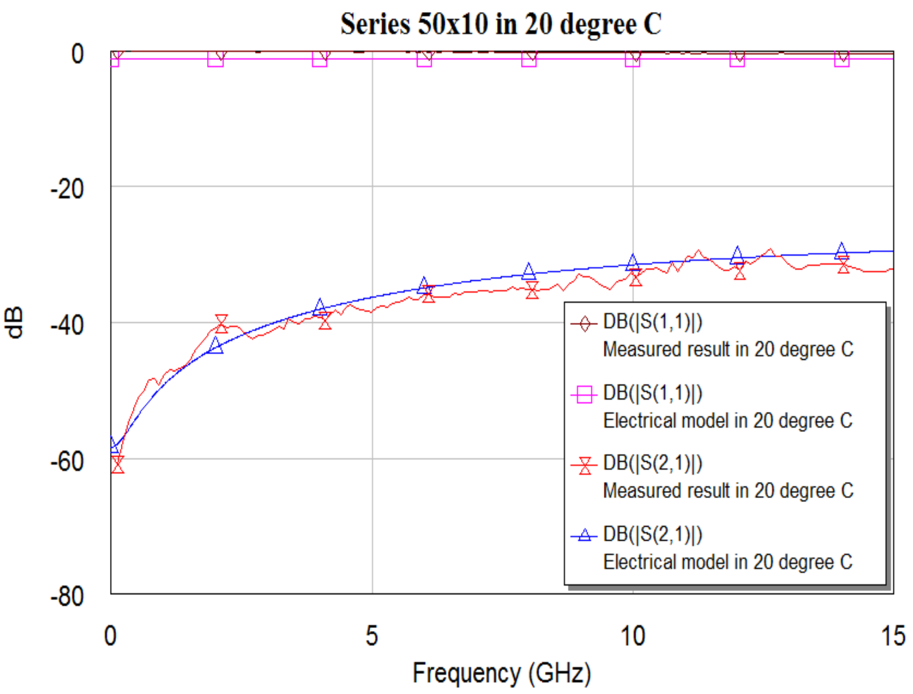

Figure 4.13 S_{11} and S_{21} of measured results and S_{11} and S_{21} of electrical model matched results at 20℃ [41]

Figure 4.14 shows the other electrical model, which is used to match S_{11} and S_{21} at 80 °C. Compared with the electrical model in Figure 4.12, there is no capacitance between the two transmission lines in the electrical model of Figure 4.14, because VO_2 becomes conducting when the temperature is increased to 80 °C, and the two transmission lines are connected by the VO_2. In this electrical model, the resistor R_3 represents the resistance of VO_2 in the conducing state, which is ~13 Ω. The capacitors of C_1, C_2 and the resistors of R_1, R_2 represent the capacitance and resistance between the signal line and the ground plane of the CPW structure. In this case, the capacitance of C_1 is 0.0165 pF, C_2 is 0.117 pF, and the resistance of R_1 is 300 Ω, and R_2 is 866 Ω. The matched results are shown in Figure 4.15.

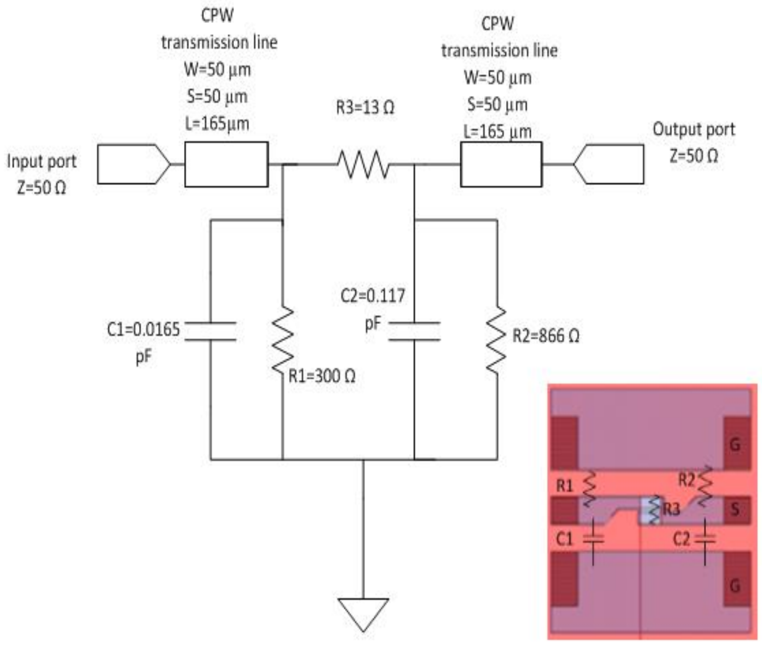

Figure 4.14 S_{11} and S_{21} of electrical model matching results for 80℃ [41]

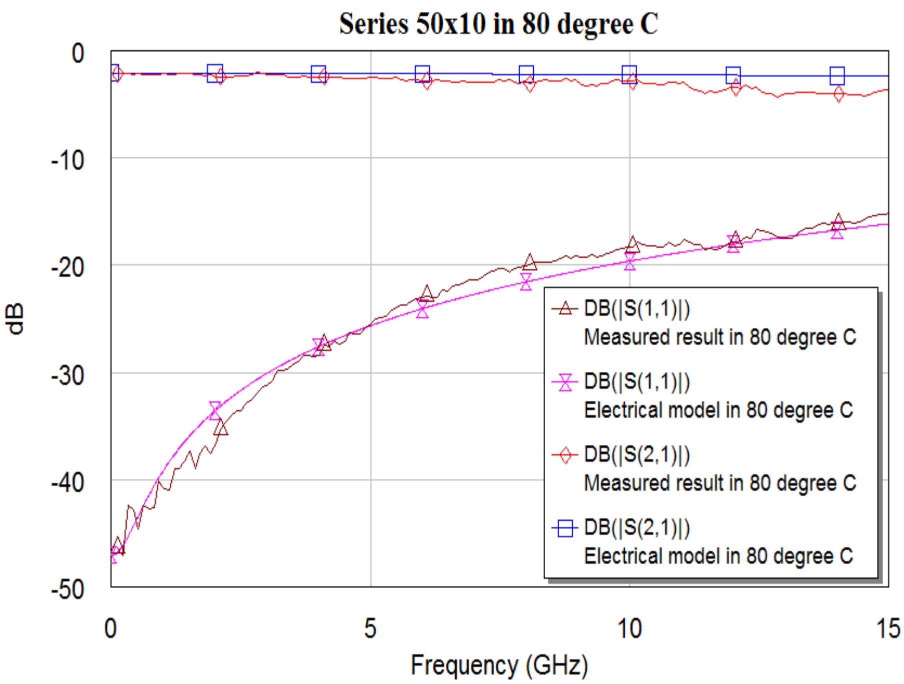

Figure 4.15 S_{11} and S_{21} of measured results and S_{11} and S_{21} of electrical model matched results at 80°C [41]

In this research, the impact of oxygen partial pressure on VO_2 thin-film deposition conditions were studied. High-quality VO_2 thin films were obtained for the oxygen partial pressure of 35 mTorr. The VO_2 thin films exhibited sharp insulator to metal transition at 68°C, with the resistance of the thin-film varistors changing by more than three orders of magnitude. A series SPST switch built using the VO_2 thin film showed that the isolation is better than 30 dB at room temperature, and the insertion loss is < 5 dB at temperatures above 68°C.

CHAPTER V

VANADIUM DIOXIDE THIN FILM BASED CPW FED RECONFIGURABLE BOWTIE ANTENNA

5.1 Introduction

Microwave antennas have been developed for a long time since the first antenna has been invented by Heinrich Hertz in 1887 [60], and the antennas have been applied in many areas, such as radar systems, mobile phones and satellite communications. Microwave antennas have different characteristics like narrow band and high quality factor. One example of narrowband microwave antenna is a microstrip antenna. Some types of the microwave antennas have broadband and high gain, and coplanar waveguide (CPW) fed antenna is one of these types of antennas.

There are different shapes of antennas, and they can affect the antennas characteristics as well. The patch antennas, spiral antennas and bowtie patch antennas are commonly used antenna shapes, and each shape of antennas has their own advantages. For the reconfigurable antenna in this research, a wide bandwidth was desired, so a bowtie antenna was chosen. The patch antenna acts similar to a dipole antenna and bowtie shape can make the antenna with wider bandwidth. As the name implies, a bowtie patch antenna resembles a bowtie shape. This antenna has two conical planar sections combined together, and the two triangular planes can be metal or dielectric. The bowtie antenna is fed in the center section where the two triangular planes are connected [78-83].

There are different ways to feed the bowtie antenna (coplanar waveguide, microstrip line, and parallel strip line), and the choice of feeding line can affect the input impedance to the antenna. Microstrip line is the most common transmission line to feed this antenna, but the coplanar waveguide is just as easy to use as a feed to the bowtie antenna.

The CPW antenna has several advantages, such as low dispersion, easy integration with active devices, and it has the ability to effectively control the characteristic impedance [84-88]. CPW fed antennas are simple to fabricate by using modern printed-circuit technology [89-90]. They also have the characteristic of broadband, and low radiation loss [84-88].

The input impedance can be matched with quarter wavelength transformers, $Z = \sqrt{Z_o Z_L}$. For an antenna, the reflections and ringing effects often happen at the feed points, and the way to reduce those effects is to load the antenna [91].

In this CPW fed bowtie antenna, sapphire is used as the substrate. The dielectric constant ε_r of sapphire is 9.7 with thickness 500 μm. There is no ground plane on the bottom of the CPW bowtie antenna.

5.2 Ideal Antenna Sizing

For an antenna to be useful, the return loss $|S_{11}|$ has to be lower than -10dB. The antennas in this research are CPW structure, and the inner patch is bowtie shape. In CPW structure, there is no ground plane on the bottom of the antenna, and the metal plane is around the bowtie shape patch. For AWR simulation, the size of the grid was set as 50 μm

to simulate the antenna. The conductivity of the Au is 2×10^6 (S/m) with thickness $0.35\mu m$, However, there is no ground on the bottom layer and top layer on CPW antennas. The bottom and top layers were set as open.

5.3 Reconfigurable Bowtie Antenna using Tungsten-Doped Vanadium Dioxide

In this study, two coplanar waveguide (CPW) bowtie antennas with undoped and W-doped VO_2 thin films were designed, simulated and fabricated. The structure of these antennas are exactly the same, the main difference between them is the antennas were integrated with different doped ratios of VO_2 thin film. As seen in Figure 5.1, the structure of antenna is ground, signal and ground with bowtie patch in the center, and the surrounded ground plane consists metal and VO_2 or W-doped VO_2 thin film. In Figure 5.2, it shows the different layers of the undoped and W-doped VO_2 bowtie patch antenna, the top layer is the Au material, the middle layer is undoped and W-doped VO_2, the bottom layer is substrate (sapphire). The thin film area is used to extend ground area around the bowtie patch. The overall size of this thermally controllable antenna dimension is 6450 μm x 6000 μm which is on the 500μm thickness sapphire substrate. The thickness of the phase change material is 0.18μm and the metal plane is 0.35μm thickness which is the top layer. The structures of the antenna are shown in Table 5.1. The film acts as an insulator at a temperature lower than the transition temperature and as a conductor at a temperature higher than the transition temperature of the film [51].

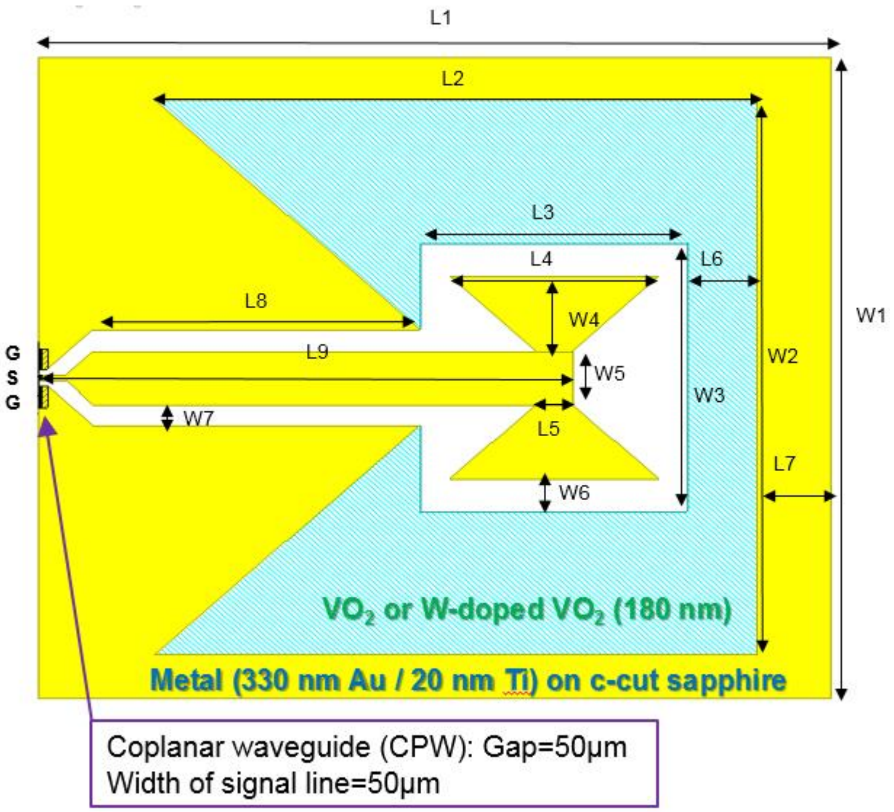

Figure 5.1 Schematic of the undoped and W-doped VO_2 thin film based CPW bowtie antenna [51]

Table 5.1 The dimensions of the undoped and W-doped VO_2 thin film based CPW bowtie antenna

Length	L1	L2	L3	L4	L5	L6	L7	L8	L9
μm	6450	4900	2175	1700	300	575	600	2650	4350
Width	W1	W2	W3	W4	W5	W6	W7		
μm	6000	5200	2500	700	500	300	200		

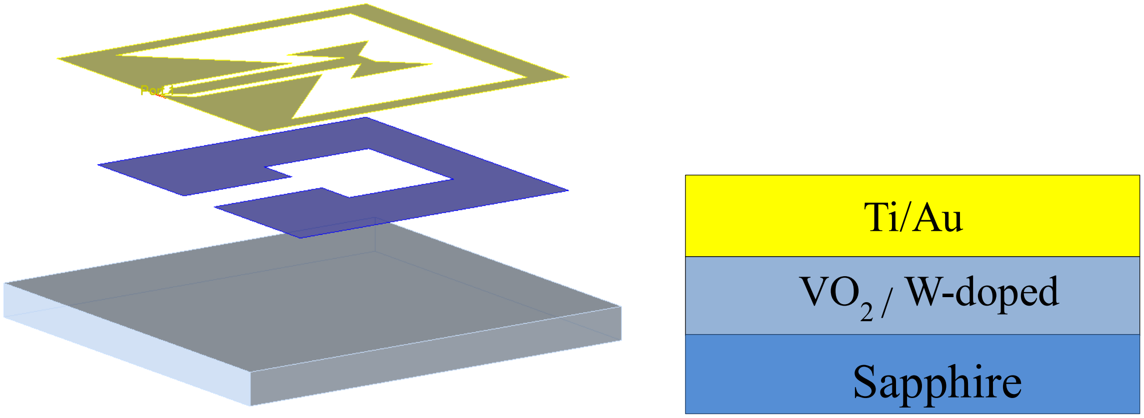

Figure 5.2 Different layers of VO$_2$ antenna, the thickness of Ti $0.02\mu m$/Au $0.33\mu m$, VO$_2$/W-doped VO$_2$ is $0.18\mu m$ and sapphire is $500\mu m$

5.4 The Optimized or Best Resulting Antenna

The simulated resonant frequency of the miniaturized CPW bowtie antenna is 7 GHz. To calculate the dimension, the formula $f = c/\lambda_{freespace}$ can be used. The f is resonant frequency of the antenna 7 GHz, c is the speed of light $3 \times 10^8 m/s$, and λ is the free space wavelength which is $0.043m$. In this antenna, the dimensions of the inner bowtie patch structure are $L = 1.7\ mm = 0.0017m$ and $W = 1.9\ mm = 0.0019m$, so the dimensions in units of wavelength are to divide the lengths in meters by the wavelength λ_o, $0.0017/0.043 = 0.0425\lambda_o$, $0.0019/0.043 = 0.044\lambda_o$, therefore, the size of the antenna is approximately $0.0425\lambda_o \times 0.044\lambda_o$. The width of the transmission line is set as 500 μm, and the gap between the transmission line and ground plane is set as 200 μm.

Compared to conventional CPW bowtie antennas; those antennas are twenty times smaller because the substrate with a high permittivity is used in this design [92-93]. The antennas are matched to the CPW line with characteristic impedance around 50 ohms.

An approximate formula [91], for the characteristic impedance of the coplanar waveguide,

$$Z_o = \frac{30\pi^2}{\sqrt{(\varepsilon_r + 1)/2}} \left[\ln \left(2 \, \frac{1 + \sqrt{k}}{1 - \sqrt{k}} \right) \right]^{-1} \tag{5.1}$$

$$k = \frac{w}{w + 2s} \tag{5.2}$$

w = center transmission line width, and *s* = the slot width between the transmission line and ground. $w = 500\ \mu m$, $s = 200\ \mu m$, the $Z_o = 51.37\ \Omega$. ε_r= relative dielectric constant of the dielectric substrate. The substrate of this antenna is sapphire, and its dielectric constant $\varepsilon_r = 9.7$. A website “Microwave 101” in [94] was used to do the impedance matching for CPW structure transmission line by providing the ground plane gap spacing, transmission line width, ε_r of the substrate and substrate thickness. The concept of aperture reconfiguration can be extended to include control of radiation pattern through changing the receiving/transmitting elements of the antenna in near real time.

5.5 Simulations of S Parameters

A commercial microwave frequency simulation tool AWR was used to develop the undoped and W-doped VO_2 thin film based CPW bowtie antenna structure in this dissertation. In the simulations, the varied conductivities of the ground area was used to simulate the undoped and W-doped VO_2 thin film, and the suitable range of the conductivity values was converted from the resistivity data of the film. In Figure 5.3, the thin film conductivity was set to 1,900 S/m to simulate the thin film that was in insulator state, and the resonant frequency of the antenna was 7 GHz with return loss S_{11} -11.45 dB. Once the conductivity of the film increased up to 4,470 S/m, the resonant frequency was shifting down to 6.704 GHz, and the S_{11} changed to -16.44 dB. After that, the notch point of the antenna was leveling off when the conductivity was increased to 72,700 S/m. These results indicate that the operating frequency range of this antenna is from 7 GHz to 6.704 GHz, and the antenna becomes inactive when the conductivity of the film is higher than 72,700 S/m.

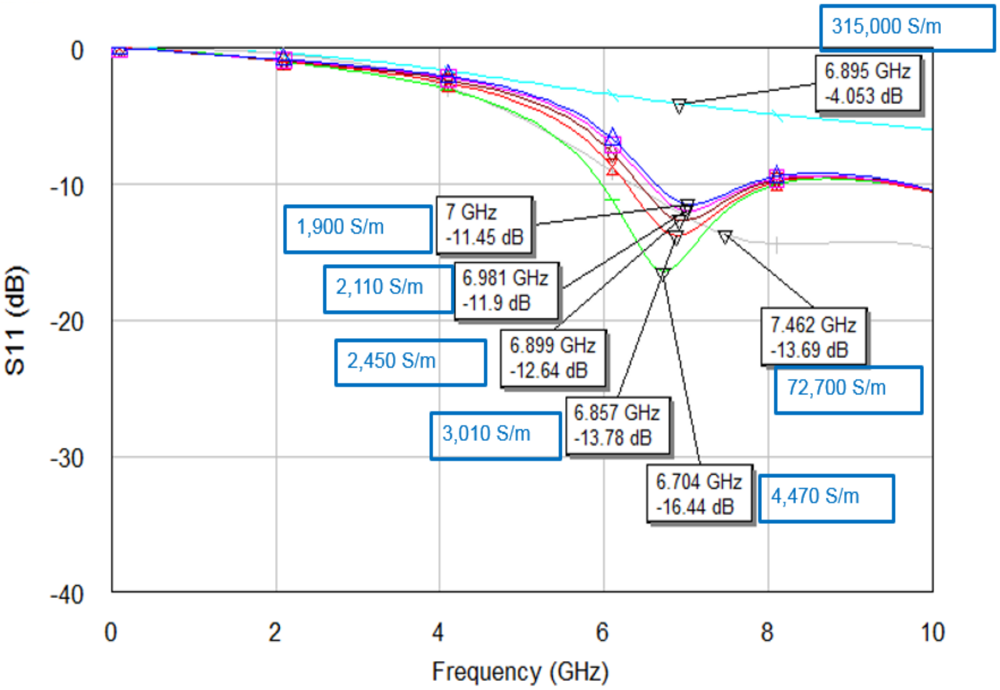

Figure 5.3 Simulations of the VO_2 thin film based CPW bowtie antenna [51]

5.6 Measurements of S Parameters

For the antenna measurements, four different tungsten-doped VO_2 thin film based CPW fed bowtie antennas were fabricated, and the undoped VO_2 thin film, 0.34 at. % W-doped VO_2 thin film, 0.54 at. % W-doped VO_2 thin film and 1.1 at. % W-doped VO_2 thin film based antenna have been measured, and the analyzed results are shown below:

5.6.1 Undoped VO_2 Thin Film Based Antenna

First, an undoped VO_2 thin film based antenna structure was fabricated, and the S_{11} measurements of the antenna structure with various temperature conditions from 20℃ to 80℃ were carried out.

As shown in Figure 5.4, at 20℃, the resonant frequency was 7.172 GHz with S_{11} -11.2dB, and the resonant frequency shifted to lower range as the temperature increased. At 73℃, the frequency became 6.678 GHz, and the return loss was in -25.34 dB. Then, the antenna became inactive at temperature higher than 74℃.

Although the frequency tuning range and minimum return loss of this real antenna showed somewhat different values, it can be clearly mentioned that these results from the real device are very consistent with the expectation that was made from the simulation results [51].

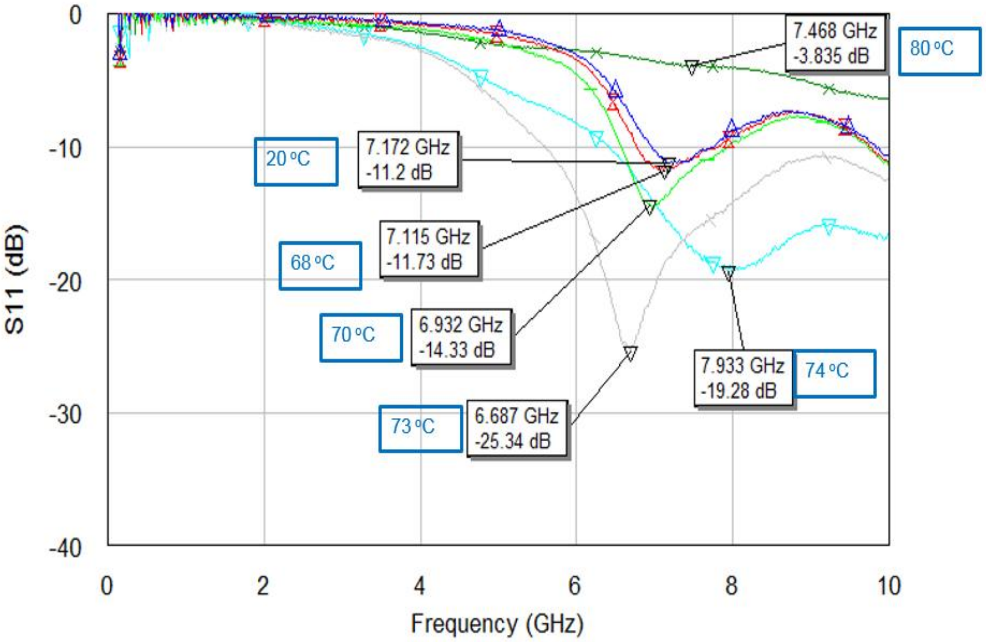

Figure 5.4 Measurements of the undoped VO_2 thin film based CPW bowtie antenna [51]

5.6.2 0.34 At. % W-Doped VO_2 Thin Film Based Antenna

Second, a 0.34 at. % W-doped VO_2 thin film was utilized to fabricate an antenna structure, and the measurement results of the antenna structure are in Figure 5.5. Compare with undoped VO_2 thin film, the phase transition temperature of this W-doped thin film reduced to 49℃ from that of undoped VO_2 film, 68℃.

As a result, a -45.11 dB of the signal return loss was achieved in frequency 6.631 GHz at 40℃ from the frequency 6.966 GHz with S_{11} -18.57 dB measured at 20℃ , and then, the antenna became inactive at the temperature higher than 50℃. This data suggests that W-doping introduces not only the decrease of the device working temperature, but also the reduction of the signal return loss of the device [51].

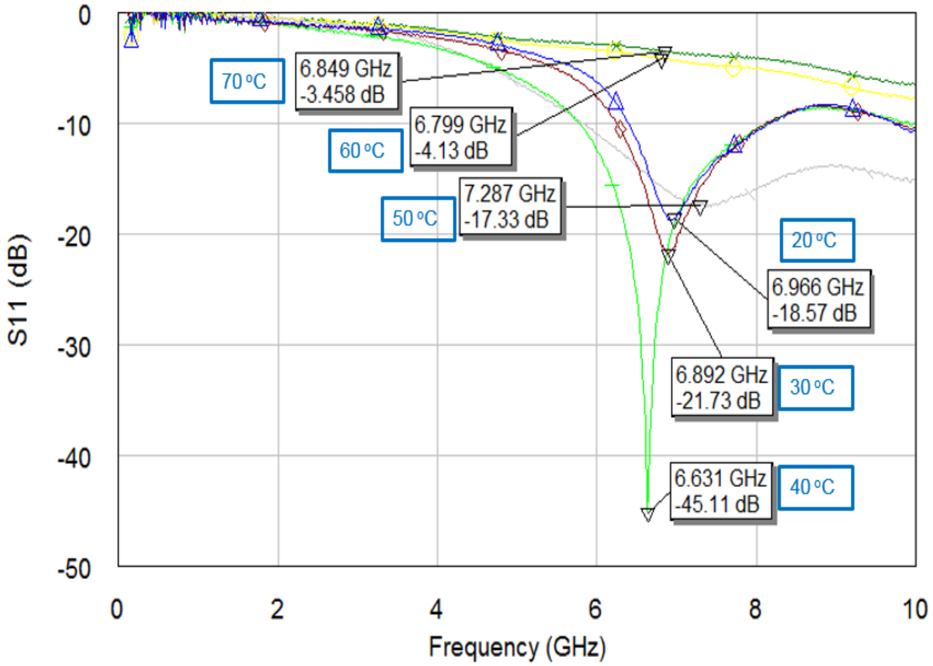

Figure 5.5 Measurements of 0.34 at. % W-doped VO_2 thin film based CPW bowtie antenna [51]

5.6.3 0.54 At. % W-Doped VO_2 Thin Film Based Antenna

Third, a 0.54 at. % W-doped VO_2 thin film based antenna was measured, and the measurement is shown in Figure 5.6. In this measurement, the ratios of the W-doped VO_2 thin film was higher than previous one, therefore, this 0.54 at. % W-doped VO_2 thin film based antenna was measured from temperature 10℃. The better signal transmission was obtained at the temperature 20℃ since the signal return loss at the temperature reached to -54.57 dB with the resonant frequency of 6.568 GHz. This suggests that the antenna made with 0.54 at. % W-doped film is showing better performance than those made with undoped and 0.34 at. % W-doped films under room temperature operation conditions (around 20℃), and the resonant frequency was shifted from 6.753GHz at 10℃ to 6.346 GHz at 30 ℃ [51].

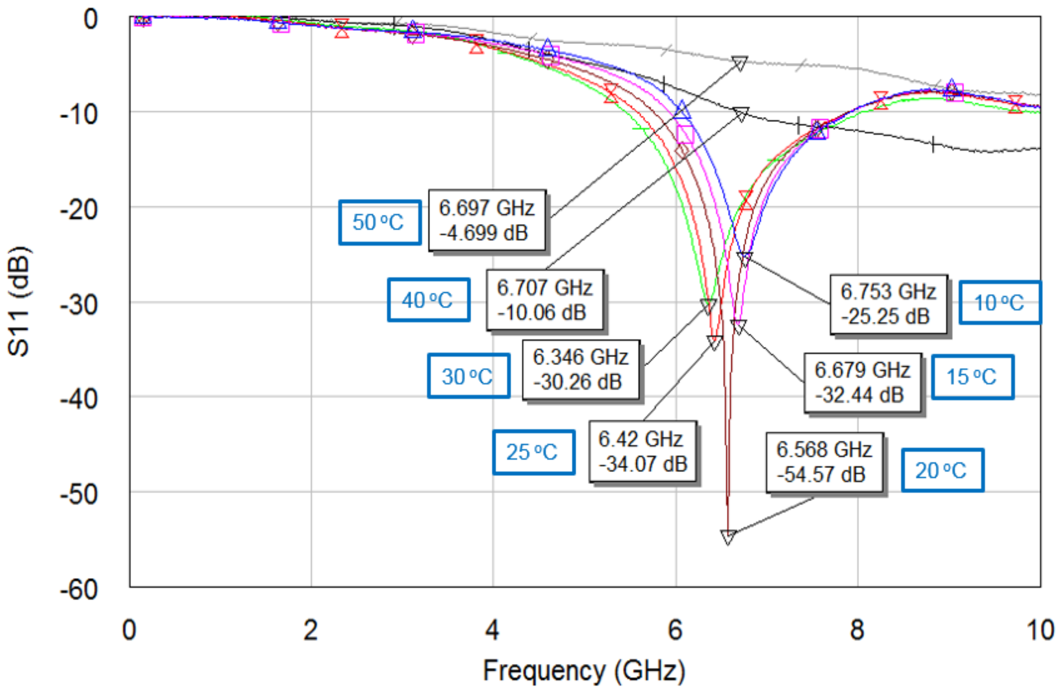

Figure 5.6 Measurements of 0.54 at. % W-doped VO_2 thin film based CPW bowtie antenna [51]

5.6.4 1.1 At. % W-Doped VO_2 Thin Film Based Antenna

Finally, a 1.1 at. % W-doped thin film based antenna was also fabricated and tested, and the measured results are shown in Figure 5.7. However, S_{11} measurement results showed that the device was not functional at room temperature, and neither at 80°C. The reason is that the conductivity of the film already reached over 100,000 S/m at 20℃, and this conductivity is close to a regular conductor. This caused the antenna radiation was effected by the 1.1 at. % W-doped thin film ground plane, and the antenna was inactive at temperature 20℃ to 80℃. The Table 5.2 shows the antenna performance comparison with different ratios of W-doped thin film based antenna [51].

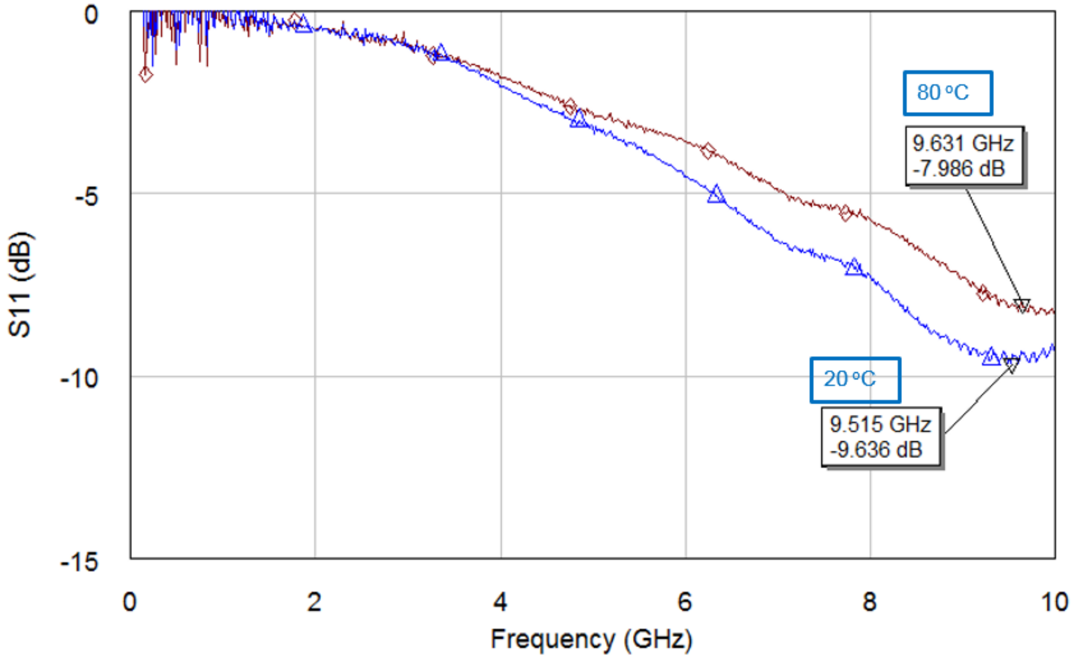

Figure 5.7 The measurements of 1.1 at. % W-doped VO_2 thin film based CPW bowtie antenna [51]

Table 5.2 Undoped and W-doped VO_2 thin films based CPW bowtie antenna performance comparison

	Frequency range	**Best matched S_{11} condition**	**Inactive Condition**
Simulation	6.7 – 7 GHz	σ = 4,470 S/m	σ > 72,700 S/m
Undoped	6.7 GHz (73°C)– 7.2 GHz (20°C)	T = 73 °C	T > 74 °C
0.34 at.% W-Doped	6.6 GHz (40°C)– 7 GHz (20°C)	T = 40 °C	T > 50 °C
0.54 at.% W-Doped	6.3 GHz (30°C)– 6.8 GHz (10°C)	T = 20 °C	T > 40 °C
1.1 at.% W-Doped	Non	Non	20°C to 80°C

5.7 Experimental

The Figure 5.8 shows the VO_2/W-doped VO_2 CPW bowtie antenna on 3” wafer. The both sides of the wafer have been diced due to taking the antennas out from the wafer. In order to measure the radiation patterns for the CPW bowtie antenna, the CPW bowtie antenna was removed from the wafer and packaged with a Printed Circuit Board (PCB).

The material of the PCB is FR4 that its dielectric constant is 4.4. There is copper layer on the PCB. The SMA connector was connected with the copper layer on the edge of the PCB, and the CPW bowtie antenna was connected with the copper layer by wire bonding as shown in Figure 5.9(a). The antenna was measured and placed on LMS-

91A thermal module system, the antenna was moved to outside of the station to avoid the metal effect from the thermal module system as shown in Figure 5.9(b). In Figure 5.9(b), the blue wire was connected to thermo meter to make sure the temperature of PCB is the same as temperature controller.

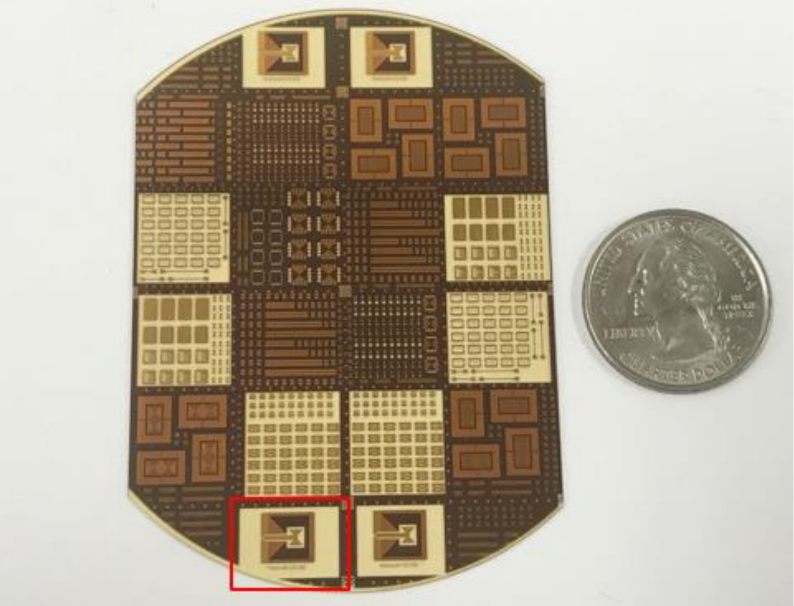

Figure 5.8 The undoped and W-doped VO_2 CPW bowtie antenna on 3” wafer as shown with red mark. Both sides of the wafer have been diced for taking the undoped and W-doped VO_2 CPW bowtie antennas out from the wafer

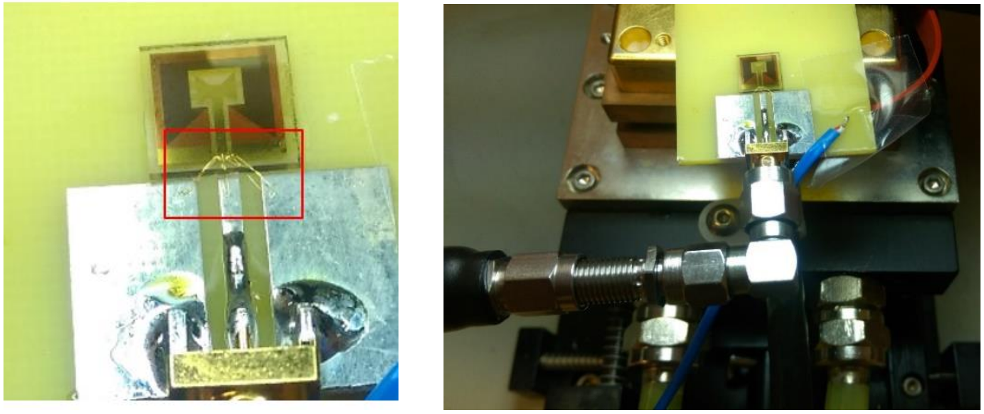
(a) (b)

Figure 5.9 (a) The red mark shows the CPW bowtie antenna wire bonding part, the antenna was placed on PCB. (b) The antenna was measured on LMS-91A thermal module system, the antenna was moved to outside of the station

5.8 Radiation Patterns

The simulation tool ADS was used to simulate the antenna radiation patterns. In CHAPTER II, the simulation tool ADS has been discussed, and the antenna pattern simulation is based on the far fields, polarization and other antenna characteristics such as gain, directivity, and radiated power.

Figure 5.10 shows the antenna EM structure in ADS, and the antenna layers set-up in ADS is shown in Figure 5.11. The Au layer (cond) and undoped and W-doped VO_2 thin film (cond2) layer were put on the top of sapphire substrate, the conductivity of the Au is $2 \times 10^6\ S/m$, and the conductivity of undoped and W-doped VO_2 thin film is $4.47 \times 10^4\ S/m$. The conductivity of undoped and W-doped VO_2 $4.47 \times 10^4\ S/m$ is to simulate the antenna at room temperature condition. The thickness of the Au is $0.35\mu m$, and the thickness of VO_2/W-doped VO_2 thin film is $0.18\mu m$. The dielectric constant of sapphire is 9.7 and the thickness is $500\mu m$.

Figure 5.12 shows the S_{11} simulation result from ADS, and the resonant frequency is 6.979 GHz, and S_{11} is -16.212dB, and Figure 5.13 and 5.14 are the simulated 3D radiation patterns of the antenna in cross-polarization and co-polarization by ADS.

Both co-polarized and cross-polarized fields were collected for the azimuth and elevation sweeps of the antenna system.

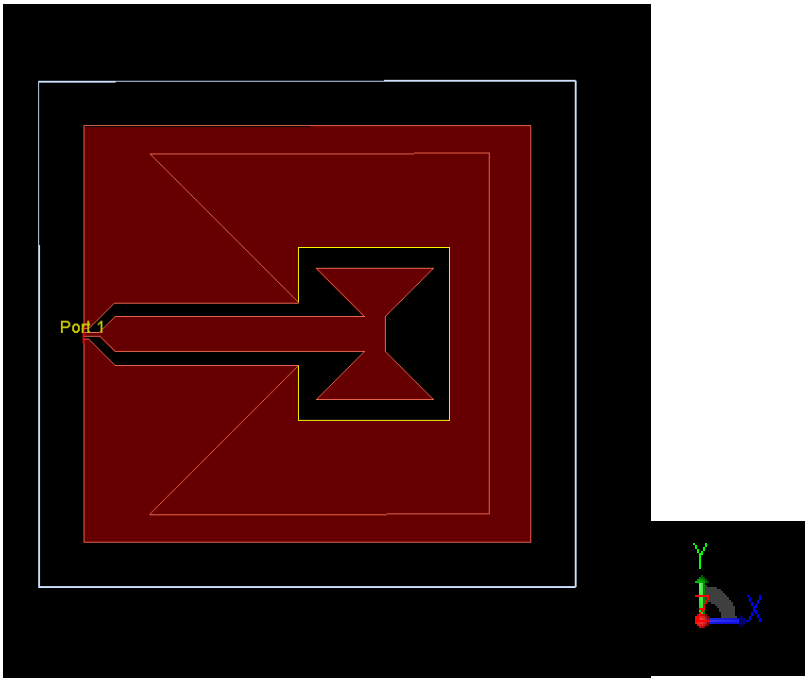

Figure 5.10 Undoped and W-doped VO_2 antenna EM structure in ADS

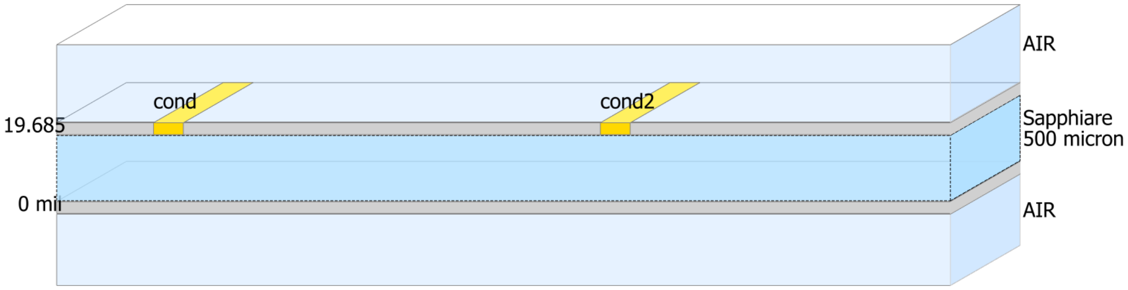

Figure 5.11 Substrate setting of antenna simulation in ADS. The cond is set as Au and the conductivity of it is $2 \times 10^6\ S/m$ with thickness $0.35\mu m$, cond2 is set for tungsten doped-VO_2 with thickness $0.18\mu m$, and the conductivity of it is $4.47 \times 10^4\ S/m$. The substrate is sapphire and the dielectric constant is set as 9.7 with thickness $500\mu m$

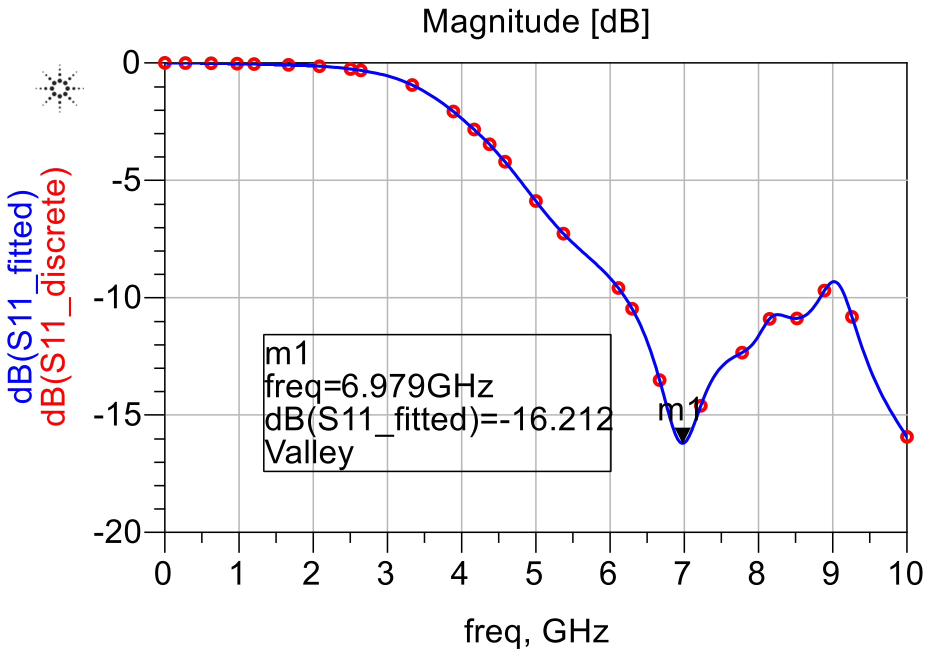

Figure 5.12 The S_{11} simulation in ADS, and the resonant frequency is 6.979 GHz, and S_{11} is -16.212dB

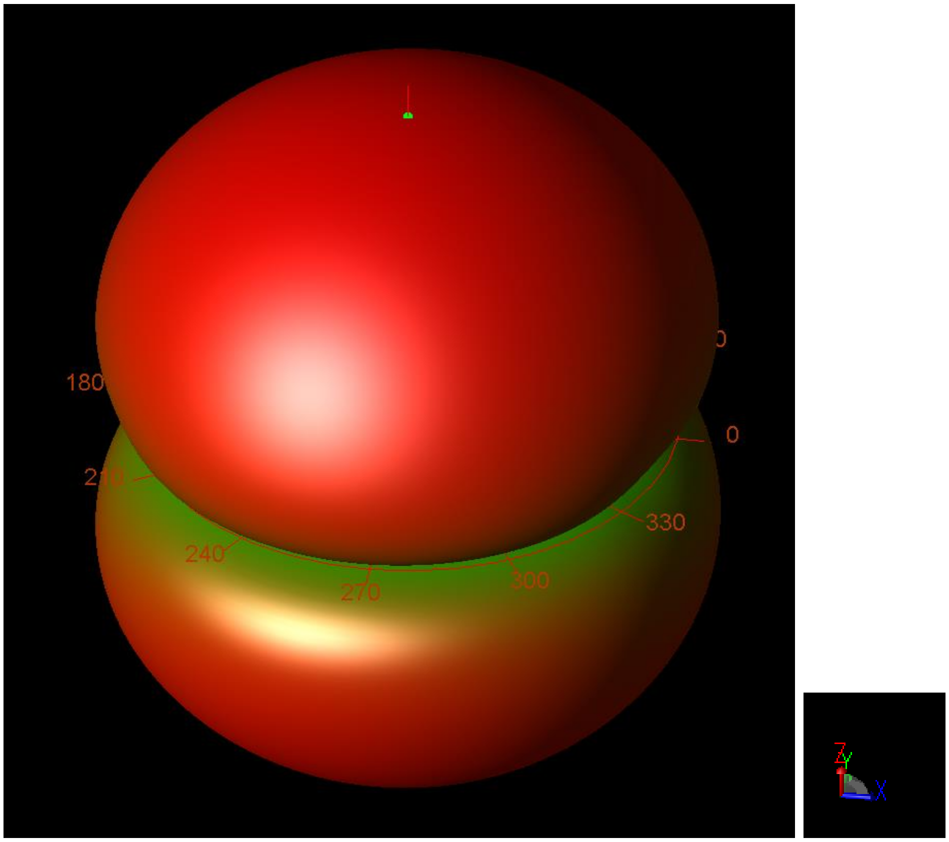

Figure 5.13 3D antenna pattern in Co-polarization using ADS

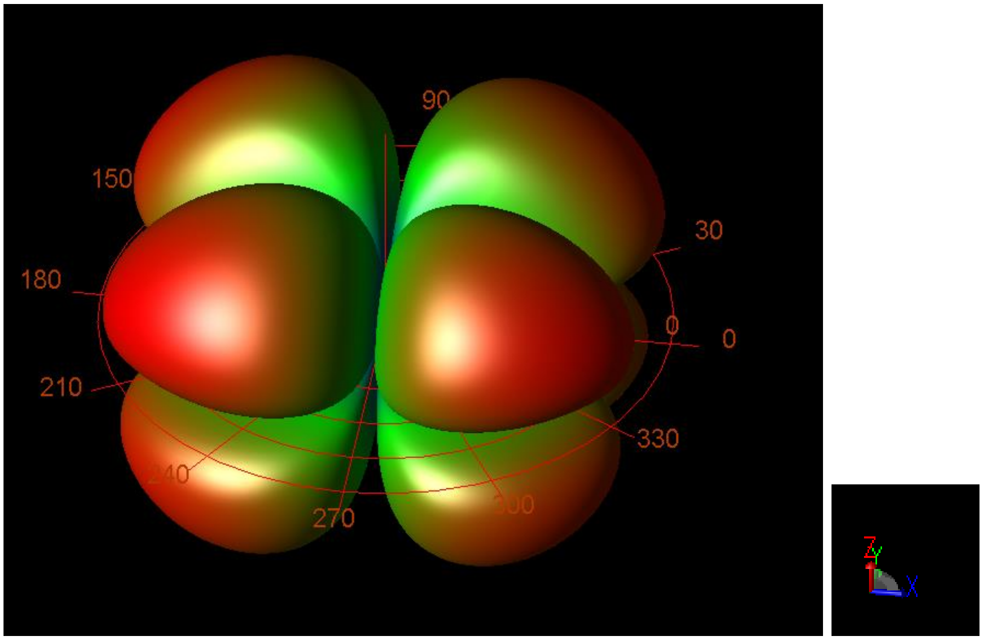

Figure 5.14 3D antenna pattern in Cross-polarization using ADS

The far field radiation patterns of the undoped and W-doped VO_2 reconfigurable antenna were measured at Radiation and Scattering Compact Antenna Laboratory (RASCAL) in the Air Force Research Laboratory. To measure the far field radiation patterns, the reconfigurable antenna was turned mechanically in an anechoic chamber. A rotating mast was in the center of the chamber, with a portable probe station connected to it. The probe station was used to hold the antenna as shown in Figure 5.15.

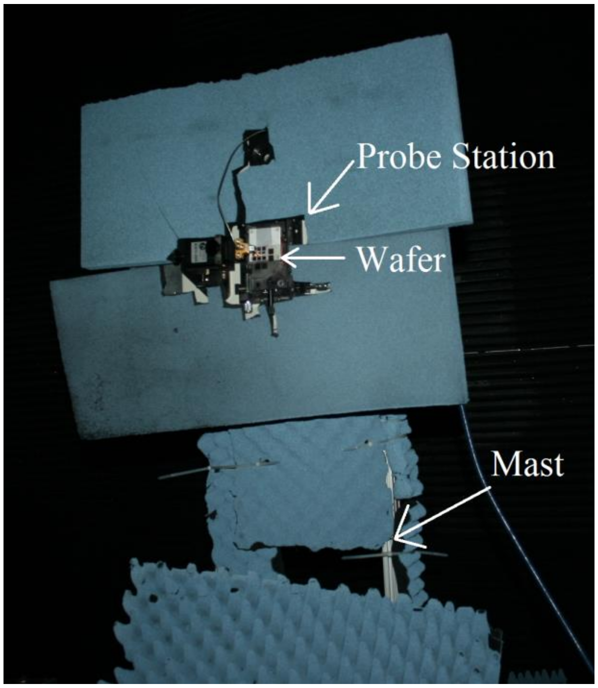

Figure 5.15 An anechoic chamber at RASCAL in the Air Force Research Laboratory

The antenna acted like a receiver and the signal traveled through the probe station's cable where the magnitude and phase data was collected and measured. For each mechanical sweep, both co-polarized and cross-polarized fields were used. The process was repeated for the other cut. The results of the co-polarized in azimuth, cross-polarized in elevation, co-polarized in azimuth, and cross-polarized in elevation were calibrated by comparing patterns from a calibration antenna. For the co-polarization antenna patterns in azimuth plane, the simulated maximum power is -0.187dBi, and the measured maximum power is -5.57dBi.

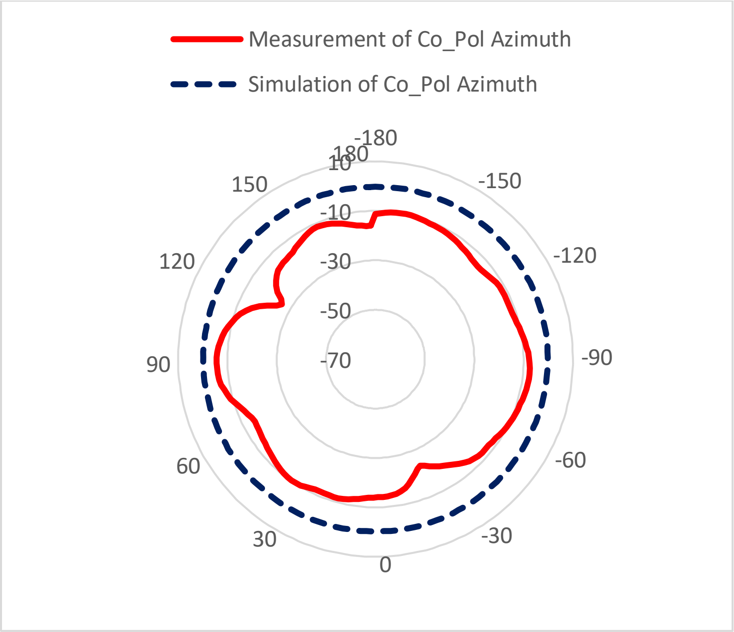

(a)

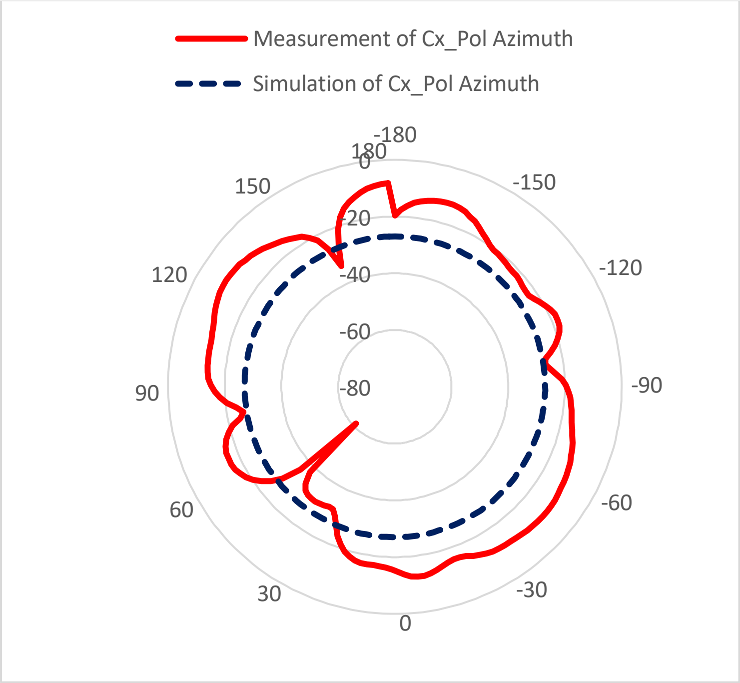

(b)

Figure 5.16 The simulation and measurement of antenna patterns of Co-polarization (a) and Cross-polarization (b) in Azimuth

For the co-polarization antenna patterns in elevation plane, the simulated maximum power is -27.002dBi, and the measured maximum power is -8.18 dBi. After these steps, the data shown is calibrated gain, and the radiation patterns of the reconfigurable antenna were shown in Figure 5.16 and 5.17.

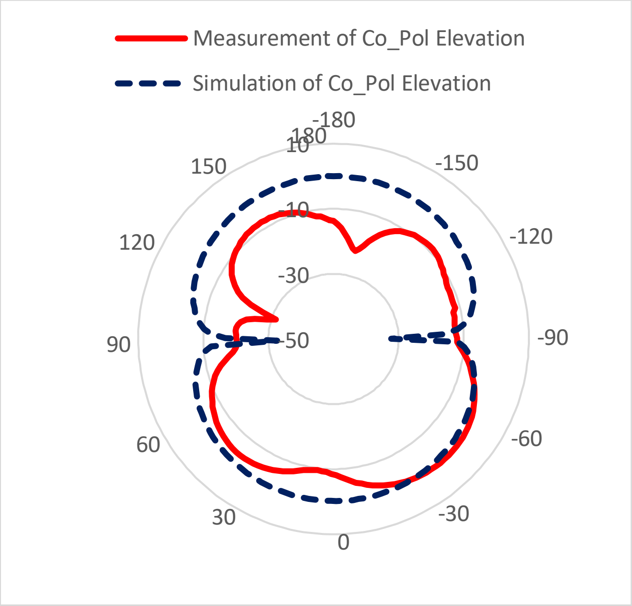

(a)

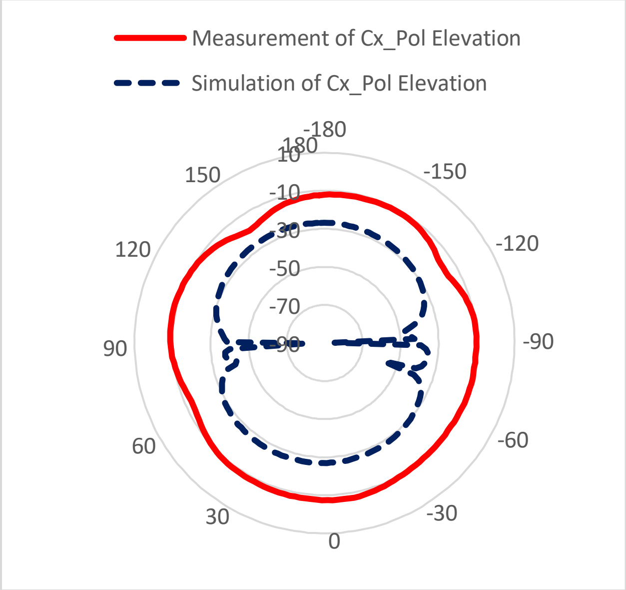

(b)

Figure 5.17 The simulation and measurement of antenna patterns of Co-polarization (a) and Cross-polarization (b) in Elevation

Figures 5.16 and 5.17 show the resulting simulations and measurements of radiation patterns at frequency of 7 GHz. Figure 5.16 shows the simulation and measurement of antenna patterns of co-polarization and cross-polarization in azimuth, and the Figure 5.17 shows the simulation and measurement of antenna patterns of co-polarization and cross-polarization in elevation.

From the radiation plots it is seen that the antenna does have a relatively wide beam-width. Also, the large differences between the co-polarized and cross-polarized curves in azimuth Figures 5.16 and in Elevation 5.17 indicate that the antenna operates under a highly linear polarization.

CHAPTER VI

VANADIUM DIOXIDE THIN FILM BASED W-BAND CPW FED RECONFIGURABLE PATCH ANTENNA

6.1 Introduction

In modern communication, the demand of the higher bandwidth for the wireless communication system has been increasing. The technology of the operating frequency of the communication system to the terahertz frequency range of the electromagnetic spectrum has shown great potential application [95].

The W-band radiation is a type of electromagnetic wave that its frequency is between 75 GHz and 110 GHz, and this frequency range is close to terahertz frequency range 0.1 THz to 10 THz. In some cases, the terahertz wave can be defined between 0.3 THz and 3 THz, in this frequency range, it is also known as submillimeter radiation [96].

Terahertz (THz) technology has been used in several applications such as imaging of medical, biological, and industrial [97]. The THz has been wildly used due to its both transmission and reflection have good penetrability on a lot of dielectric materials and non-polar liquids, and could be used for detecting explosives with expanded reflection [96-98]. Because of this, the THz wave can go through a lot of non-transparent objects and create perspective imaging [96-98]. The terahertz technology is not only interesting to the civilian manufacturers, but also to the military [96]. For military application, the terahertz technology can be used in security communication, anti-stealth radar, chemical and biological agent detection and the fields of national defense [97].

6.2 Thermally Controllable Rectangular Patch Antenna using Tungsten-Doped Vanadium Dioxide in W-Band

In this research, a W-doped VO_2 based W-band antenna was designed in 93 GHz, and the antenna has been simulated. The overall dimension of the antenna is 3000 µm×3000 µm shown in Figure 6.1, and the structures of the antenna is shown in Table 6.1. The substrate of this antenna is sapphire with 500 µm thickness, and the thickness of the W-doped VO_2 is $0.18\mu m$.

The top layer of the antenna is metal with $0.35\mu m$ thickness (Ti $0.02\mu m$/Au $0.33\mu m$). The antenna is CPW structure ground, signal, and ground with inner rectangular patch connected to the transmission line, and the inner patch is surrounded by metal ground plane. There is a pair of W-doped VO_2 wires between the transmission line and the ground plane. The AWR was used to simulate the resonant frequency of the antenna, and the varied conductivities of W-doped VO_2 were used to simulate the thermally controllable patch antenna at different temperature ranges.

The W-doped VO_2 lines are in high resistance at room temperature, at this point, the most of signal will go through to the patch of the antenna from the feed line. When the temperature increases, the resistance of the W-doped VO_2 gets lower, and W-doped VO_2 line starts to allow more signal going through to the ground plane from the transmission line. The resonant frequency of the antenna shifts to lower frequency range once the temperature increases.

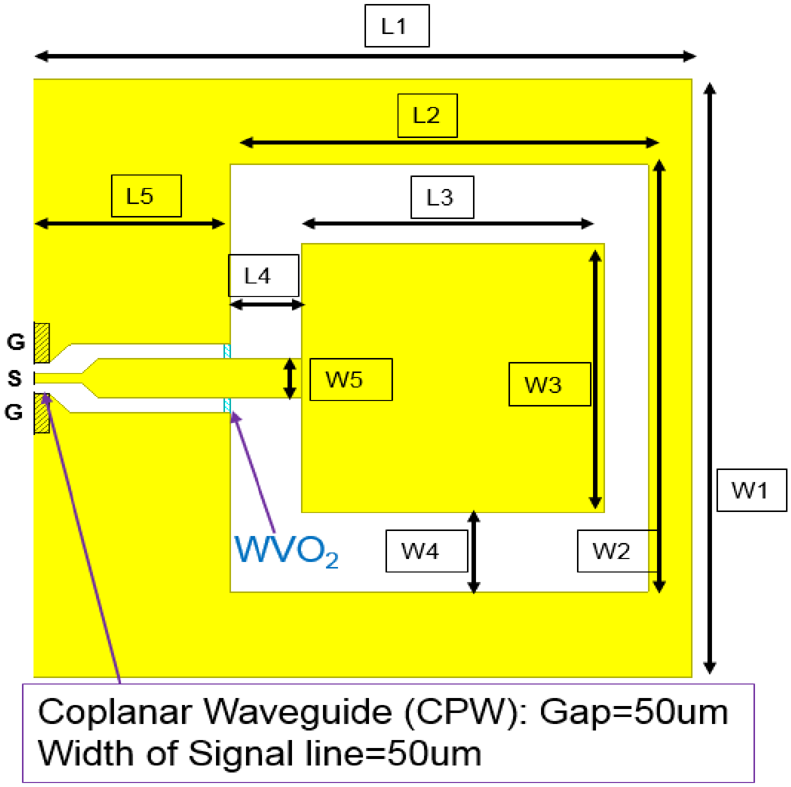

Figure 6.1 Coplanar waveguide (CPW): Gap=50µm, Width of Signal line=50µm. Tungsten-doped vanadium dioxide (W-doped VO_2) size: Width=75µm, Length=25 µm in each gap. The thickness metal layer is Ti 0.02μm/Au 0.33μm, and the thickness of W-doped VO_2 layer is 0.18μm and substrate Sapphire thickness is 500μm

Table 6.1 The dimension of the thermally controllable patch antenna

Length	L1	L2	L3	L4	L5
µm	3000	1900	1375	325	900
Width	W1	W2	W3	W4	W5
µm	3000	2150	1350	400	200

6.3 Simulations

The simulated resonant frequency of the W-band CPW patch antenna is 92.9 GHz and the return loss S_{11} is -51.4dB as shown in Figure 6.2. To calculate the dimension, the formula $f = c/\lambda_{freespace}$ can be used. f is the resonant frequency of the antenna which is 92.9 GHz, c is the speed of light $3 \times 10^8 (m/s)$, and λ is the free space wavelength which is $0.0032m$. In this antenna, the dimensions of the inner bowtie patch structure are $L = 1.375\ mm = 0.001375m$ and $W = 1.35\ mm = 0.00135m$, so the dimensions in units of wavelength are to divide the lengths in meters by the wavelength λ_o , $0.001375/0.0032 = 0.43\lambda_o$, $0.00135/0.0032 = 0.42\lambda_o$, therefore, the size of the antenna is approximately $0.43\lambda_o \times 0.42\lambda_o$.

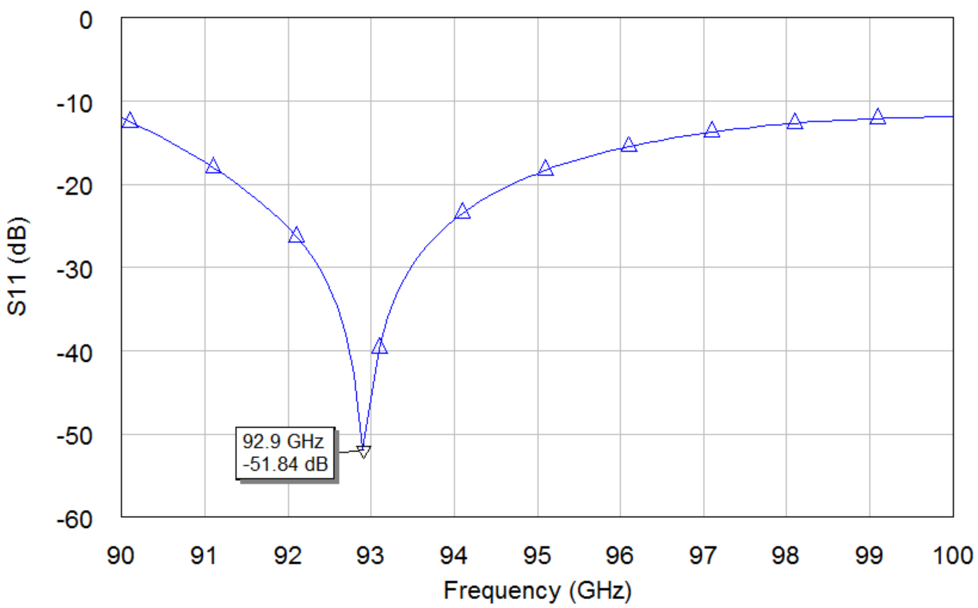

Figure 6.2 This simulated result of 93 GHz antenna, the resonant frequency is 92.9 GHz, and the return loss S_{11} is -51.84 dB

To achieve the reconfigurable antenna, the resonant frequency of the W-band CPW patch antenna moves from high frequency range to lower frequency range when the temperature increase from lower temperature to higher temperature. From the simulated results as shown in Figure 6.3, the resonant frequency of the antenna is 92.9 GHz with S_{11} -51.4dB when the W-doped VO_2 is in low conductivity, and the resonant frequency shifts to 91.4 GHz with S_{11} -43.03dB when the W-doped VO_2 is in high conductivity. The status of antenna switches to inactive eventually when the temperature keeps increasing and the conductivity of the W-doped VO_2 is close to Au which is 2×10^6 (S/m).

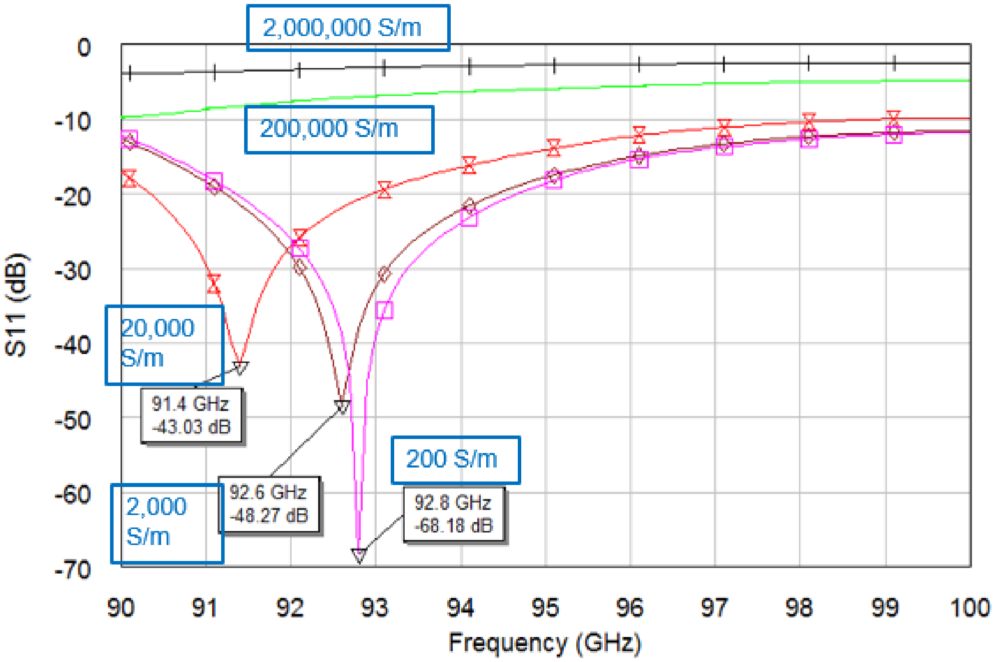

Figure 6.3 This simulated result of antenna is with W-doped VO_2 strip line in different values of conductivity. When the conductivity of the W-doped VO_2 gets higher, the resonant frequency of the antenna shifts to lower range. The status of antenna switches to inactive eventually when the temperature keeps increasing and the conductivity of the W-doped VO_2 is close to Au which is 2×10^6 (S/m)

6.4 Measurements

This 93 GHz antenna was simulated, fabricated and measured. The Figure 6.4 shows the W-doped VO_2 93 GHz antenna was fabricated on 3” wafer (UD VO_2-50 wafer). The red mark in Figure 6.4 shows where one of the 93 GHz antenna is located. The measured result is shown in Figure 6.5, and it indicates the resonant frequency of the antenna is in 90.975 GHz, and the S_{11} is in -31.85dB.

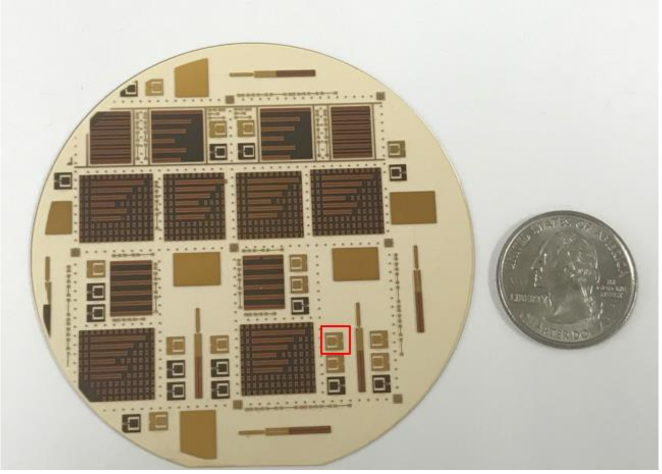

Figure 6.4. The red mark shows one of the W-doped VO_2 93 GHz antennas on UD VO_2-50 wafer

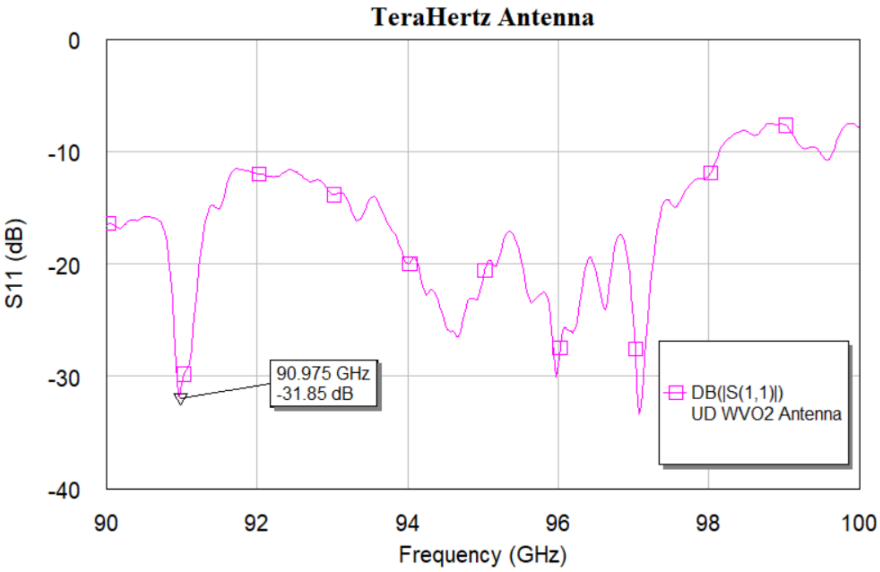

Figure 6.5 W-doped VO_2 93 GHz antenna measurement of S_{11}

6.5 Radiation Patterns

The simulation tool ADS was used to simulate the 93 GHz antenna radiation patterns as well. For this antenna, the measured antenna patterns are not available yet. Figure 6.6 shows the antenna EM structure in ADS, and the antenna layers set-up in Figure 6.7 is the same as the 7 GHz CPW bowtie antenna shown in CHAPTER V. The top layer was set as Au layer (cond) and W-doped VO_2 (cond2) layer was put on the same layer as Au layer. The Au and W-doped VO_2 layers were placed on the top of sapphire substrate, the conductivity of the Au is $2 \times 10^6\ S/m$, and the conductivity of W-doped VO_2 is $100\ S/m$. The thickness of the Au is $0.35\mu m$, and the thickness of W-doped VO_2 is $0.18\mu m$. The dielectric constant of sapphire is 9.7 and the thickness is $500\mu m$.

Figure 6.8 shows the S_{11} simulation result from ADS, and the resonant frequency is 92.4 GHz, and S_{11} is -18.507dB , and Figure 6.9 and 6.10 are the simulated 3D radiation patterns of the antenna in cross-polarization and co-polarization using ADS. Both co-polarized and cross-polarized fields were collected for the azimuth and elevation sweeps of the antenna system.

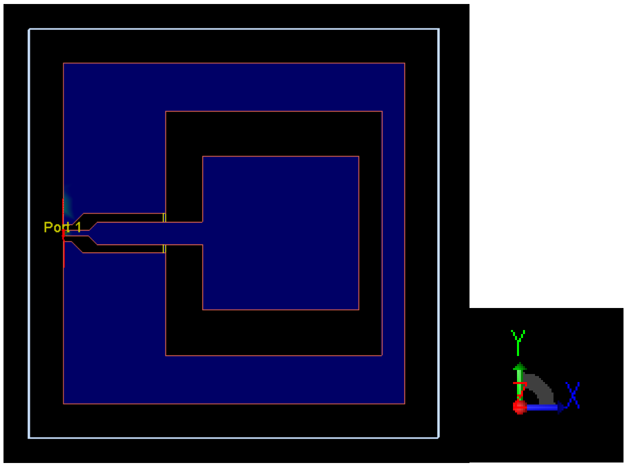

Figure 6.6 Simulation of EM structure in ADS

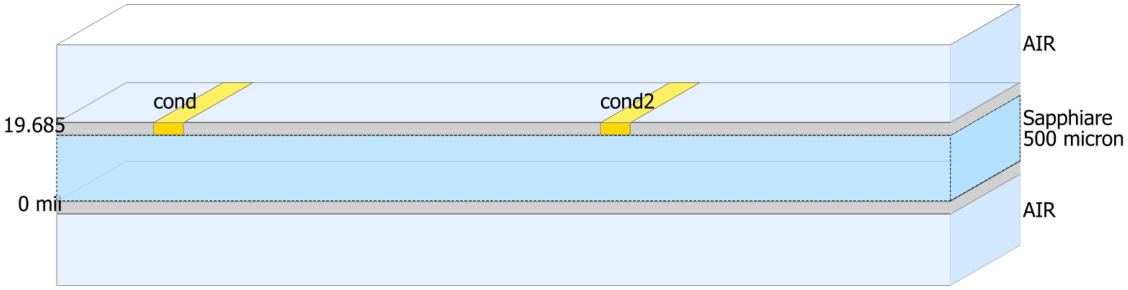

Figure 6.7 Substrate setting of antenna simulation in ADS. The cond is set as Au and the conductivity of it is $2 \times 10^6\ S/m$ with thickness $0.35\mu m$, cond2 is set for tungsten doped-VO_2 with thickness $0.18\mu m$, and the conductivity of it is $100\ S/m$. The substrate is sapphire and the dielectric constant is set as 9.7 with thickness $500\mu m$

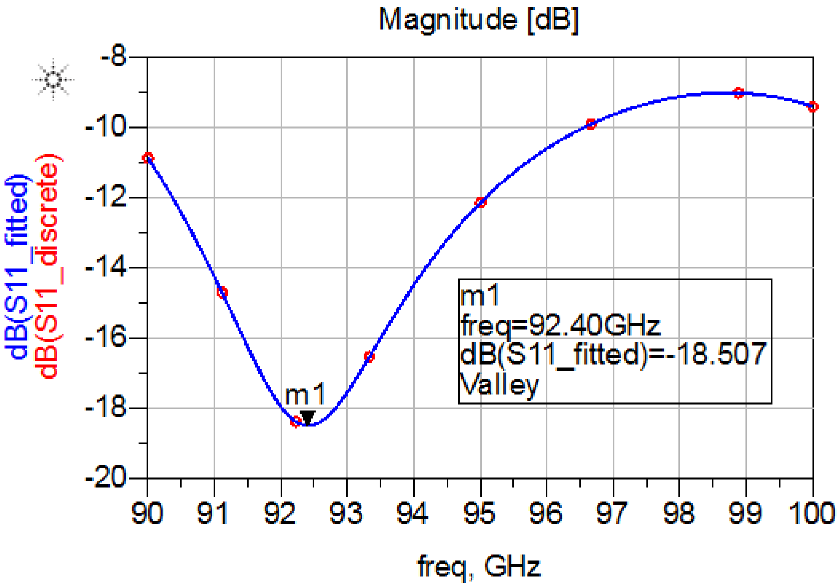

Figure 6.8 The S_{11} simulation in ADS, and the resonant frequency is 6.979 GHz, and S_{11} is -16.212dB

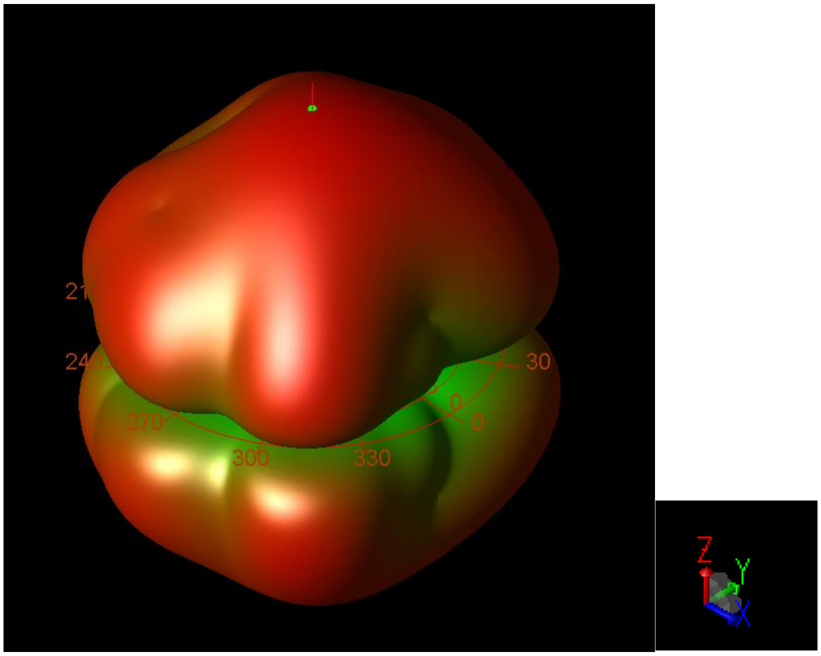

Figure 6.9 3D antenna pattern of 93 GHz antenna in Co-polarization using ADS

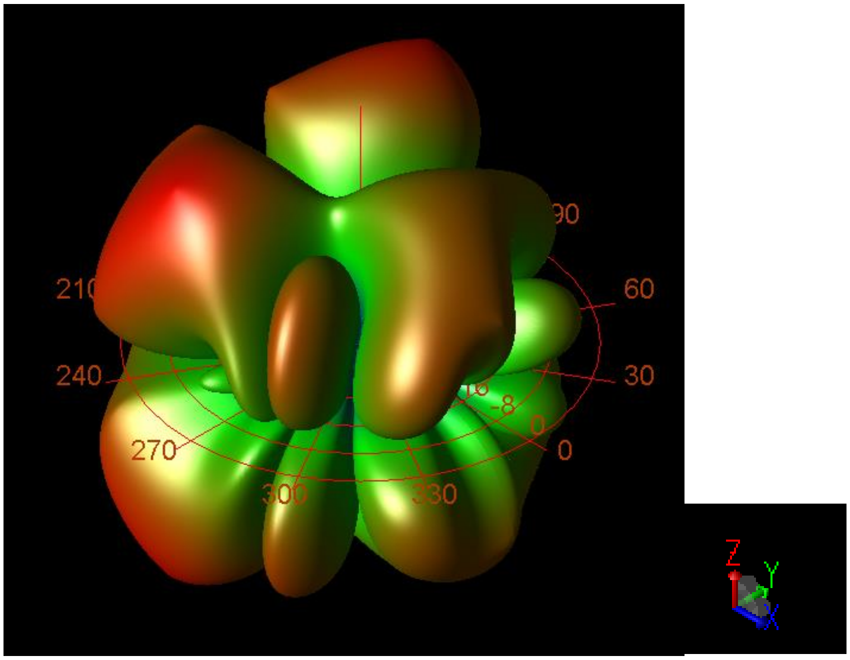

Figure 6.10 3D antenna pattern of 93 GHz antenna in Cross-polarization using ADS

Figures 6.11 and 6.12 show the resulting simulations of radiation patterns at frequency of 93 GHz. Figure 6.11 shows the simulation of antenna patterns of co-polarization and cross-polarization polarization in azimuth, and the Figure 6.12 shows the simulation of antenna patterns of co-polarization and cross-polarization polarization in elevation. The simulated maximum power of co-polarization antenna pattern in azimuth plane is 1.04×10^{-4}dBi, and the simulated maximum power of cross-polarization antenna pattern in azimuth plane is 1.18×10^{-6} dBi. The simulated maximum power of co-polarization antenna pattern in elevation plane is 0.221dBi, and the simulated maximum power of cross-polarization antenna pattern in elevation plane is 0.041dBi. After these steps, the data shown is calibrated gain, and the radiation patterns of the reconfigurable antenna were shown in Figure 5.16 and 5.17.

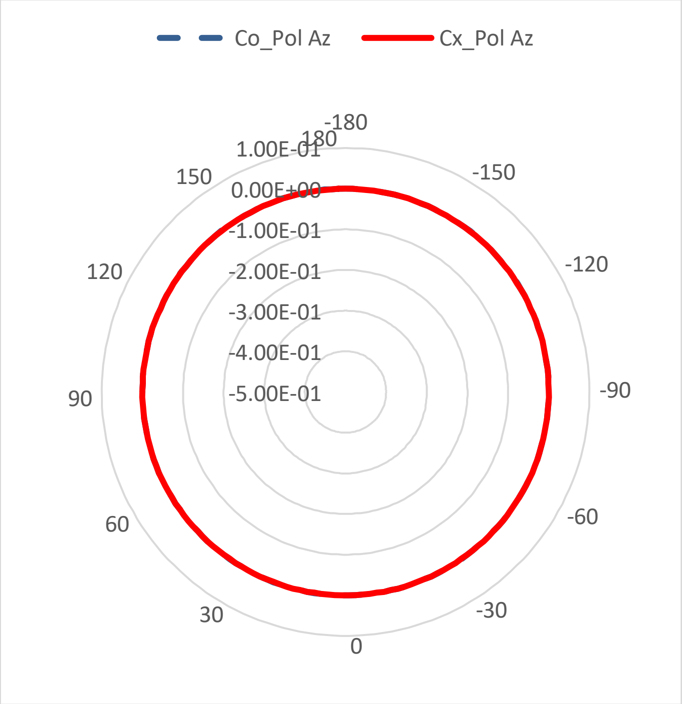

Figure 6.11 Simulations of Co-polarization and Cross-polarization in Azimuth

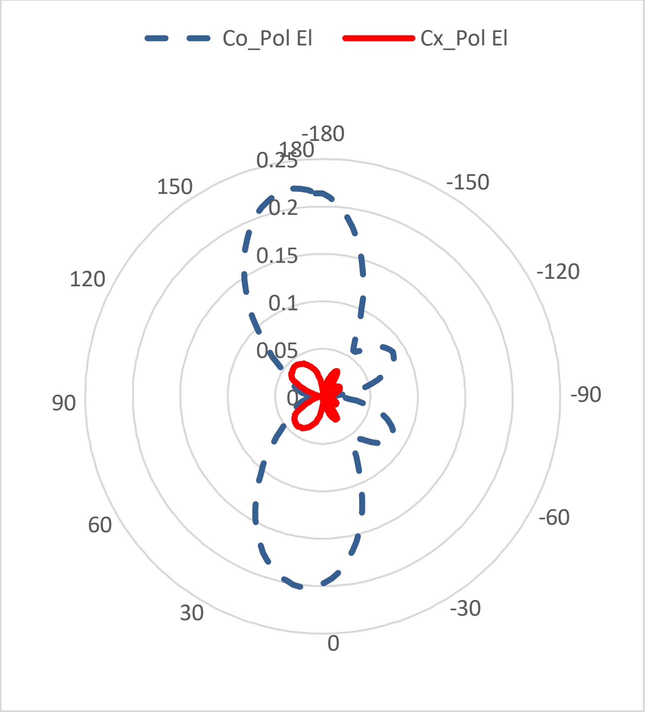

Figure 6.12 Simulations of Co-polarization and Cross-polarization in Elevation

CHAPTER VII

SUMMARY AND CONCLUSION

In this research, the impact of oxygen partial pressure on deposition conditions was studied for synthesis of single phase VO_2 thin films. The temperature dependent VO_2 based varistor devices can be used for reconfigurable RF or microwave applications. The results in this research presented so far have proved that the VO_2 thin films are suitable materials to be applied in different kinds of RF devices such as RF switches, RF filters, and reconfigurable antenna. The VO_2 thin films exhibited sharp insulator to metal transition at 68℃, with the resistance of the thin-film varistors changing by more than three orders of magnitude.

RF shunt switches, and series SPST switches were designed and built using the VO_2 thin film. A reconfigurable CPW bowtie antenna using insulator to metal transition in tungsten-doped vanadium dioxide were designed, fabricated and measured in this research. The series SPST switch using VO_2 thin films showed that the isolation is better than 30 dB at room temperature, and the insertion loss is < 4 dB at temperatures above 68℃.

VO_2 and W-doped VO_2 thin films were synthesized by the reactive PLD technique. By attaching W-wires on a metallic V target surface with various wire separation distances, the amount of W atoms in the VO_2 film structure was successfully controlled. The reconfigurable antenna is achieved by the undoped and W-doped VO_2, the resonant frequency shifts from high frequency range to low frequency range and then inactive when the temperature increases. As expected, the phase transition temperature decreased, the width of transition behavior broadened as the atomic % of W in the film structure increased. By using the films, thermally tunable and switchable bowtie RF antenna structures were designed, fabricated, and tested. According to the measurement results, it was clarified that these VO_2 and W-doped VO_2 thin film based RF antenna structures were fully functional with the successful frequency tuning capability. There were different ratios of W-doped VO_2 thin film based antennas fabricated, undoped, 0.34 at. % W-doped VO_2, 0.54 at. % W-doped VO_2 and 1.1 at. % W-doped VO_2. From the measured results in CHAPTER V, the 0.54 at. % W-doped VO_2 thin film based antenna provided the best tunability for the reconfigurable antenna, and the frequency tuning range was from 6.753 GHz (10℃) to 6.346 GHz (30℃). The best antenna performance of the 0.54 at. % W-doped VO_2 thin film based antenna was observed at 20 °C with the −54.57 dB of the signal return loss at the 6.568 GHz of the resonant frequency. This reconfigurable antenna also proved that the different ratios of tungsten doped with vanadium dioxide has the decent effect to the transition temperature. The measured radiation patterns of the 0.54 at. % W-doped VO_2 thin film based antenna was obtained in this dissertation. The co-polarized and cross-polarized curves in azimuth and in elevation were measured and indicate that the antenna operates under a highly linear polarization

Additional, the W-doped VO_2 based W-band CPW reconfigurable antennas have been designed, simulated, fabricated and measured as well. The S-parameters were simulated and measured, but this dissertation only provided the simulated antenna patterns for this antennas.

Although VO_2 based switches show less than ideal RF performance compared with the RF microelectromechanical systems (MEMS) switches [99-100], the switching time could be as fast as 5 ns [101-102] compared with 25 μs of MEMS switches [99], and such devices have no fatigue concern, which is typical in the RF MEMS switches. For the future work, first, we plan to design different structures and heater coil for the SPST VO_2 thin film based switches in order to improve the performance and decreasing the effect of heater coil. Second, the radiation patterns of W-doped VO_2 thin film based CPW bowtie antenna in CHAPTER V and the S-parameters of the W-doped VO_2 thin film based W-band CPW antenna in CHAPTER VI were only measured at room temperature. Third, the radiation patterns of W-doped VO_2 thin film based W-band CPW antenna in CHAPTER VI have not been measured yet.

The future work will be concentrated on improved the performance of the SPST VO_2 thin film based switches and acquiring the S-parameters and radiation patterns of those antenna structures at different temperatures.

BIBLIOGRAPHY

[1] R. Want, “RFID explained: A primer on radio frequency identification technologies”, Synthesis Lectures on Mobile and Pervasive Computing, vol. 1, Jan. 2006, pp. 1-94

[2] J. Landt, “The History of RFID”, IEEE Potentials, vol. 24, no. 4, Oct.-Nov. 2005, pp. 8 - 11

[3] A. R. Koelle, S. W. Depp, and R. W. Freyman, “Short-range radiotelemetry for electronic identification, using modulated RF backscatter”, Proceedings of the IEEE, vol. 63, no. 8, Aug. 1975, pp. 1260-1261

[4] K. Finkenzeller, RFID Handbook: Radio-Frequency Identification Fundamentals and Applications, 2nd ed.: Wiley, 2004.

[5] U. Karthaus, M. Fischer, “Fully integrated passive UHF RFID transponder IC with 16.7 uW minimum RF input power”, IEEE Journal of Solid-State Circuits, vol. 38, no. 10, Oct. 2003, pp. 1602 – 1608

[6] R. Glidden et al., “Design of ultra-low-cost UHF RFID tags for supply chain applications”, IEEE Communications Magazine, vol. 42, no. 8, Aug. 2004, pp. 140 – 151

[7] D. Vita and G. Iannaccone, “Design criteria for the RF section of UHF and microwave passive RFID transponders”, IEEE Transactions on Microwave Theory and Techniques, vol. 53, no. 9, Sept. 2005, pp. 2978-2990

[8] E. B. Joy, “Near-field qualification methodology”, IEEE Transactions on Antennas and Propagation, vol. 36, no. 6, Jun. 1988, pp. 836 - 844

[9] T. Lacoma, http://www.gadgetreview.com/2015/02/what-is-iot, *gadgetreview,* August 3, 2015

[10] L. Zhou "RF MEMS DC contact switch for reconfigurable antennas", MS Thesis San Diego State University, 2006. Web. May 11th, 2011

[11] E. Brown, "RF-MEMS switches for reconfigurable integrated circuits", *IEEE Trans Microwave Theory Tech* 46 (11), 1868 1998.

[12] F. J. Morin, "Oxides which show a metal-to-insulator transition at the Neel temperature," *Phys. Rev. Lett.*, vol. 3, no. 1, pp. 34–36, Jul. 1959.

[13] D. Adler, J. Feinleib, H. Brooks, and W. Paul, "Semiconductor-To-Metal Transitions in Transition-Metal Compounds", Phys. Rev. 155, 851 – Published 15 March 1967

[14] A. Zylbersztejn and N. F. Mott, "Metal-insulator transition in vanadium dioxide," *Phys. Rev. B*, vol. 11, no. 11, pp. 4383–4395, Jun. 1975.

[15] R.A. Rodriguez-Solis, H.L. Pacheco, N. Sepulveda, "Reconfigurable slotted microstrip patch using VO_2", *Antennas and Propagation Society International Symposium (APSURSI), 2012 IEEE*, pp. 1-2, July 2012

[16] R.A. Rodriguez-Solis, Y.M. Saade, "Cavity backed annular slot ring antenna with reconfigurable slots using VO_2", *Antennas and Propagation Society International Symposium (APSURSI), 2013 IEEE,* pp. 578 – 579**,** July 2013

[17] T. S. Teeslink, D. Torres, J. L. Ebel, N. Sepulveda and D. E. Anagnostou, "Reconfigurable Bowtie Antenna Using Metal-Insulator Transition in Vanadium Dioxide", *IEEE Antennas and Wireless Propagation Letters*, VOL. 14, Feb. 25, 2015

[18] N. Dávila, E. Merced, and N. Sepúlveda, “Electronically variable optical attenuator enabled by self-sensing in vanadium dioxide,” *IEEE Photon. Technol. Lett.*, vol. 26, no. 10, pp. 1011–1014, May 15, 2014.

[19] C. Aurelian, G. Julien, B. Pierre, O. Jean-Christophe, C. Corinne and C. Alain (2010). “Exploiting the Semiconductor-Metal Phase Transition of VO_2 Materials: a Novel Direction towards Tuneable Devices and Systems for RF-Microwave Applications”, *Advanced Microwave and Millimeter Wave Technologies Semiconductor Devices Circuits and Systems,* Moumita Mukherjee (Ed.), ISBN: 978-953-307-031-5.

[20] J. Givernaud, C. Champeaux, A. Catherinot,A. Pothier, P. Blondy,A. Crunteanu, “Tunable band stop filters based on Metal-Insulator Transition in vanadium dioxide thin films”, *Microwave Symposium Digest, 2008 IEEE MTT-S International,* pp. 1103-1106, June, 2008

[21] R. Cabrera, E. Merced, and N. Sepúlveda, “Performance of electrothermally driven VO_2-based MEMS actuators,” *J. Microelectromech. Syst.*, vol. 23, no. 1, pp. 243–251, Feb. 2014.

[22] M. J. Caruso, T. Bratland, C. H. Smith, R. Schneider, “A New Perspective on Magnetic Field Sensing”, *Sensors Magazine,* December 1998

[23] J.E. Lenz, “A Review of Magnetic Sensors”, Proceedings of the IEEE, vol. 78, no.6, 973-989, June, 1990

[24] B. L. Danner, “Characterization of Metal-Insulator-Transition (MIT) Phase Change Materials (PCM) for Reconfigurable Components, Circuits, and Systems”, Master Thesis Air Force Institute of Technology, March 2013

[25] M. Surface, "Photovoltaics: The Encyclopedia of Earth," June 10 April 2014. [Online]. Available: www.eoearth.org/article/Photovoltaics. [Accessed November 18 2015]

[26] K. Schubert and H. Fricke, Z. Naturforsch. 6a, 781 (1951).

[27] K. Schubert and H. Fricke, Z. Metallkunde 44, 457 (1953).

[28] T. Siegrist, P. Jost, H. Volker, M.Woda, P. Merkelbach, C. Schlockermann and M.Wuttig,"Disorder-induced localization in crystalline phase-change materials", *Nature Materials*, 10, 202–208, January 09, 2011

[29] A. H. Gwin, C. H. Kodama, T. V. Laurvick, R. A. Coutu, Jr., and P. F. Taday, "Improved terahertz modulation using germanium telluride (GeTe) chalcogenide thin films", *Applied Physics Letters*, 107, 031904, July 22, 2015

[30] L.J. van der Pauw, "A method of measuring specific resistivity and Hall effect of discs of arbitrary shape", Philips Res. Rep. 13, 1_9 (1958).

[31] J. Goldak,C.S. Barrett, D. Innes, and W. Youdelis, Structure of alpha GeTe. J. Chem. Phys. 44, 3323_3325 (1966).

[32] L. Perniola, V. Sousa, A. Fantini, E. Arbaoui, A. Bastard, M. Armand, A. Fargeix, C. Jahan, J. F. Nodin, A. Persico, D. Blachier, A. Toffoli, S. Loubriat, E. Gourvest, G. Betti Beneventi, H. Feldis, S. Maitrejean, S. Lhostis, A. Roule, O. Cueto, G. Reimbold, L. Poupinet, T. Billon, B. De Salvo, D. Bensahel, P. Mazoyer, R. Annunziata, P. Zuliani and F. Boulanger, "Electrical Behavior of Phase-Change Memory Cells Based on GeTe," *IEEE Electron Device Letters*, vol. 31, no. 5, pp. 488-490, 2010.

[33] N. Pashkov, G. Navarro, J. C. Bastien, M. Suri, L. Perniola, V. Sousa, S. Maitrejean, A. Persico, A. Roule, A. Toffoli, G. Reimbold, B. De Salvo, O. Faynot, P. Zuliani and R. Annunziata, "Physical and Electrical Characterization of Germanium or Tellurium rich GexTe1-x for Phase Change Memories," in *Solid- State Device Research Conference*, Helsinki, Finlad, 2011.

[34] P. Cintas, “The road to chemical names and eponyms: Discovery, priority, and credit,” *Angew. Chem. Int. Ed.*, vol. 43, no. 44, pp. 5888–5894, Nov. 2004.

[35] G. F. V. Voort, *Metallography: Principles and Practice*. Materials Park, OH, USA: ASM International, 1999.

[36] F. Cardarelli, *Materials Handbook: A Concise Desktop Reference*. New York, NY, USA: Springer-Verlag, 2008.

[37] N. N. Greenwood and A. Earnshaw, “Chemistry of the elements,” *Crystal Res. Technol.*, vol. 20, no. 5, p. 662, 1984.

[38] G. Brauer, *Handbook of Preparative Inorganic Chemistry*, 2nd ed. New York, NY, USA: Academic, 1963.

[39] J. Zhang, E. Merced, N. Sepúlveda, and T. Xiaobo, “Modeling and inverse compensation of nonmonotonic hysteresis in VO_2-coated microactuators,” *IEEE/ASME Trans. Mechatronics*, vol. 19, no. 2, pp. 579–588, Apr. 2014.

[40] R. A. Wood, “Use of vanadium oxide in microbolometer sensors,” U.S. Patent 5 450 053, Sep. 12, 1995.

[41] K.C. Pan, W. Wang, E. Shin, K. Freeman, and G. Subramanyam,“Vanadium Oxide Thin-Film Variable Resistor-Based RF Switches,” *IEEE Transactions on Electron Devices,* Vol. 62, No. 9, September 2015

[42] P. J. Hood and J. F. DeNatale, “Millimeter-wave dielectric properties of epitaxial vanadium dioxide thin films,” *J. Appl. Phys.*, vol. 70, no. 1, pp. 376–381, 1991.

[43] A. S. Barker, Jr., H. W. Verleur, and H. J. Guggenheim, “Infrared optical properties of vanadium dioxide above and below the transition temperature,” *Phys. Rev. Lett.*, vol. 17, no. 26, pp. 1286–1289, Dec. 1966.

[44] J. Wei, Z. Wang, W. Chen, and D. H. Cobden, “New aspects of the metal–insulator transition in single-domain vanadium dioxide nanobeams,” *Nature Nanotechnol.*, vol. 4, no. 7, pp. 420–424, 2009.

[45] J. F. De Natale, P. J. Hood, and A. B. Harker, “Formation and characterization of grain-oriented VO_2 thin films,” *J. Appl. Phys.*, vol. 66, no. 12, pp. 5844–5850, 1989.

[46] E. Merced, X. Tan, and N. Sepúlveda, “Strain energy density of VO_2-based microactuators,” *Sens. Actuators A, Phys.*, vol. 196, pp. 30–37, Jul. 2013.

[47] D. P. Partlow, S. R. Gurkovich, K. C. Radford, and L. J. Denes, “Switchable vanadium oxide films by a sol-gel process,” *J. Appl. Phys.*, vol. 70, no. 1, pp. 443–452, 1991.

[48] G. A. Rozgonyi and D. H. Hensler, “Structural and electrical properties of vanadium dioxide thin films,” *J. Vac. Sci. Technol.*, vol. 5, no. 6, pp. 194–199, Nov. 1968.

[49] S. Lysenko, A. Rua, F. Fernandez, and H. Liu, “Optical nonlinearity and structural dynamics of VO_2 films,” *J. Appl. Phys.*, vol. 105, no. 4, pp. 043502-1–043502-6, 2009.

[50] G. J. Kovács, D. Bürger, I. Skorupa, H. Reuther, R. Heller, and H. Schmidt, “Effect of the substrate on the insulator–metal transition of vanadium dioxide films,” *J. Appl. Phys.*, vol. 109, no. 6, p. 063708, 2011

[51] E. Shin, K.C. Pan, W. Wang, G. Subramanyam, V. Vasilyev, K. Leedy, T. Quach", Tungsten-doped vanadium dioxide thin film based tunable antenna", *Materials Research Bulletin 101 (2018) 287–290,* February 2018

[52] N. Émond, A. Hendaoui, and M. Chaker,"Low resistivity $W_xV_{1-x}O_2$-based multilayer structure with high temperature coefficient of resistance for microbolometer applications", *Applied Physics Letters,* October 07 2015

[53] T. Driscoll, H.-T. Kim, B.-G. Chae, B.-J. Kim, Y.-W. Lee, N. Marie Jokerst, S. Palit, D. R. Smith, M. Di Ventra, D. N. Basov, "Memory Metamaterials", *Science,* Vol. 325, Issue 5947, pp. 1518-1521, Sep 18, 2009

[54] J.-H. Cho, Y.-J. Byun, J.-H. Kim, Y.-J. Lee, Y.-H. Jeong, M.-P. Chun, J.-H. Paik, T. H. Sung , "Thermochromic characteristics of WO_3-doped vanadium dioxide thin films prepared by sol–gel method", *Ceramics International,* Volume 38, Supplement 1, Pages S589-S593, January 2012,

[55] X. Tan, T. Yao, R. Long, Z. Sun, Y. Feng, H. Cheng, X. Yuan, W. Zhang, Q. Liu, C. Wu, Y. Xie, S. Wei, "Unraveling metal-insulator transition mechanism of VO_2 triggered by tungsten doping", *Sci. Rep*., 2 (2012) 466.

[56] Keysight, https://www.keysight.com/upload/cmc_upload/All/BTB_Network_2005-1.pdf, Oct. 25th, 2018

[57] Keysight Technologies Two-port Measurements and S-Parameters, Application Note, https://literature.cdn.keysight.com/litweb/pdf/5992-2693EN.pdf?id=2941528, Oct. 25th, 2018

[58] M. Golio, The RF and microwave handbook, CPC press, 2001.

[59]http://edadocs.software.keysight.com/display/ads2009U1/Radiation+Patterns+and+Antenna+Characteristics+in+Momentum, Keysight Technologies, September 2018

[60]W. L. Stutzman, G. A. Thiele, Antenna Theory and Design 3rd EDITION, Wiley, 2013

[61] J. Livage, "Optical and electrical properties of vanadium oxides synthesized from alkoxides", *Coordination Chemistry Reviews*, *391*, 190-192. 1999

[62] S. Deki, Y. Aoi, A. Kajinami, "A novel wet process for the preparation of vanadium dioxide thin film", *Journal of Materials Science, 32,* 4269. 1997

[63] R. Lopez, L.A. Boatner, T.E. Haynes, R.F. Haglund, L.C. Feldman, "Enhanced hysteresis in the semiconductor-to-metal phase transition of VO_2 precipitates formed in SiO2 by ion implantation", *Appl. Phys. Lett. 79*, 3161-3163. 2001

[64] J.W. Ye, L. Zhou, F.J. Liu, J. Qi, W.T. Gong, Y. Lin, G.L. Ning, "Preparation, characterization and properties of thermochromic tungsten-doped vanadium dioxide by thermal reduction and annealing", *Journal of Alloys and Compounds,* Volume 504, Issue 2, Pages 503–507, 20 August 2010

[65] R. Binions, C. Piccirillo, I. P. Parkin, "Tungsten doped vanadium dioxide thin films prepared by atmospheric pressure chemical vapour deposition from vanadyl acetylacetonate and tungsten hexachloride", *Surface and Coatings Technology***,** Volume 201, Issues 22–23, Pages 9369–9372, 25 September 2007

[66] Z.F. Peng, W. Jiang, and H. Liu, "Synthesis and Electrical Properties of Tungsten-Doped Vanadium Dioxide Nanopowders by Thermolysis", *Journal of Physical Chemistry, 111* (3), pp 1119–1122, 2007

[67] O. Ya. Berezina, A. A. Velichko, L. A. Lugovskaya, A. L. Pergament, G. B. Stefanovich, D. V. Artyukhin, and A. N. Strelkov, "Properties of Tungsten-Doped Vanadium Oxide Films", Technical Physics Letters, Volume 33, Issue 7, pp 552-555, July 2007

[68] J.Q. Shi, S.X. Zhou, B. You, L.M. Wu, "Preparation and thermochromic property of tungsten-doped vanadium dioxide particles", *Solar Energy Materials and Solar Cells*, Volume 91, Issue 19, Pages 1856–1862, 23 November 2007

[69] Z.L. Huang, C.H. Chen, C.H. Lv, S.H. Chen, "Tungsten-doped vanadium dioxide thin films on borosilicate glass for smart window application", *Journal of Alloys and Compounds*, Volume 564, Pages 158–161, 5 July 2013

[70] L. Zhou, "RF MEMS DC contact switch for reconfigurable antennas", MS Thesis San Diego State University, 2006. Web. May 11th, 2011

[71] E. Brown, "RF-MEMS switches for reconfigurable integrated circuits", *IEEE Trans Microwave Theory Tech* 46 (11), 1868 1998.

[72] J. Givernaud *et al.*, "Microwave power limiting devices based on the semiconductor–metal transition in vanadium–dioxide thin films," *IEEE Trans. Microw. Theory Techn.*, vol. 58, no. 9, pp. 2352–2361, Sep. 2010.

[73] A. Crunteanu *et al.*, "Voltage- and current-activated metal–insulator transition in VO_2-based electrical switches: A lifetime operation analysis," *Sci. Technol. Adv. Mater.*, vol. 11, no. 6, p. 065002, Dec. 2010.

[74] H.-T. Kim *et al.*, "Mechanism and observation of Mott transition in VO_2-based two- and three-terminal devices," *New J. Phys.*, vol. 6, no. 1, p. 52, May 2004.

[75] J. Sakai and M. Kurisu, “Effect of pressure on the electric-field-induced resistance switching of VO_2 planar-type junctions,” *Phys. Rev. B, Condens. Matter*, vol. 78, no. 3, p. 033106, Jul. 2008.

[76] B.-J. Kim, Y. W. Lee, S. Choi, S. J. Yun, and H.-T. Kim, “VO_2 thin-film varistor based on metal-insulator transition,” *IEEE Electron Device Lett.*, vol. 31, no. 1, pp. 14–16, Jan. 2010.

[77] G. Subramanyam, E. Shin, D. Brown, H. Yue, “Thermally controlled vanadium dioxide thin film microwave devices”, *Circuits and Systems (MWSCAS), 2013 IEEE 56th International Midwest Symposium*, pp. 73-76, Aug. 2013

[78] A. A. Eldek, A. Z. Elsherbeni, and C. E. Smith, “Characteristics of bow-tie slot antenna with tapered tuning stubs for wideband operation,” *Progress In Electromagnetics Research* vol.49, pages 53-69, 2004.

[79] Lin, Y. D. and S.-N. Tsai, “Coplanar waveguide-fed uniplanar bow-tie antenna,” *IEEE Trans. Ant. Prop.*, Vol. AP-45, No. 2, 305–306, Feb. 1997.

[80] E.A. Soliman, S. Berbels, P. Delmotte, G. A. E. Vandenbosch, and E. Beyne, “Bow-tie slot antenna fed by CPW,” *Electron Lett.*, Vol. 35, 514–515, 1999.

[81] J, F. Huang, and C.-W. Kuo, “CPW-fed bow-tie slot antenna,” *Microwave Opt. Technol. Lett.*, Vol. 19, No. 5, 358–360, Dec. 1998.

[82] A.A. Eldek, A. Z. Elsherbeni, and C. E. Smith, “Wideband bow-tie slot antennas for radar applications,” *2003 IEEE Topical Conference on Wireless Communication Technology*, Honolulu, Hawaii, October 2003.

[83] E.A. Soliman, S. Brebels, P. Delmotte, G.A.E. Vandenbosch and E. Beyne, “Bowtie slot antenna fed by CPW,” *Electron. Lett.*, vol. 35, (7), pages 514-515, 1999.

[84] E.A. Soliman, S. Brebels, G.A.E. Vandenbosch and , E. Beyne, “Xband Brick Wall Antenna Fed by CPW,” *Electron. Lett.*, vol. 34, (9), pages 836-838, 1998.

[85] M.-E. Chen and J.-H. Wang, “CPW-fed crescent patch antenna for UWB applications,” Electron. Lett., vol. 44, (10), pages 613–614, 2008.

[86] H. Jiang, M. Patterson, C.H. Zhang and G. Subramanyam, “Frequency Agile Microstrip Patch Antenna Using Ferroelectric Thin Film Varactor Technology,” *Proc. IEEE AP-S Int. Symp. Dig.*, pages 1-4, 2009.

[87] A. A. Eldek, A. Z. Elsherbeni, C. E. Smith, and K-F Lee, “Wideband slot antennas for radar applications,” *Proc. IEEE Radar Conf.*, 79–84, Huntsville, AL, May 2003.

[88] M. Miao, B. L. Ooi, and P. S. Kooi, “Broadband CPW-fed wide slot antenna,” *Microwave Opt. Technol. Lett.*, Vol. 25, No. 3, 206–211, May 2000.

[89] G. Subramanyam, F. Ahamed and R. Biggers, “A Si MMIC Compatible Ferroelectric Varactor Shunt Switch for Microwave Application,” *IEEE Microwave and Guided Wave Lett.*, vol. 15, (11), pages 739-741, 2005.

[90] C.M. Bartsch, G. Subramanyam, J. Grote, F.K. Hopkins, L.L. Brott and R.R. Naik, “A New Capacitive Test Structure for Microwave Characterization of Biopolymers,” *Microwave Opt. Tech. Lett.*, vol. 49, (6), pages 1261-1265, 2007.

[91]C. A. Balanis, Modern antenna handbook, Wiley,2008

[92]A.K. Skrivervik, J.-F. Zurcher, O. Staub and J.R. Mosig, “PCS Antenna Design: The Challenge of Miniaturization,” *IEEE Trans. Antennas Propag.*, vol. 43, (4), pages 12-27, 2001.

[93] F. Namin, T.G. Spence, D.H. Werner and E. Semouchkina, "Broadband, Miniaturized Stacked-Patch Antennas for L-Band Operation Based on Magneto-Dielectric Substrates," *IEEE Trans. Antennas Propag.*, vol. 58, (9), pages 2817- 2822, 2010.

[94] https://www.microwaves101.com/calculators/864-coplanar-waveguide-calculator, Microwave101, September 2018

[95] K.um RanjanJha, G.Singh, "Terahertz planar antennas for future wireless communication: A technical review*", Infrared Physics & Technology,* Volume 60, Pages 71-80, September 2013

[96]B. Zhu, Y. Chen, K. Deng, W. Hu, and Z. S. Yao, "Terahertz Science and Technology and Applications", *PIERS Proceedings*, Beijing, China, March 23–27, 2009

[97] M. Shur, "Terahertz technology: Devices and applications," *Proceedings of ESSCIRC, 13–21*, Grenoble, France, 2005.

[98] Y, Chen, H, Liu, M. J. Fitch, R. Osiander, J. B. Spicer, M. Shur, X.-C. Zhang, "THz diffuse reflectance spectra of selected explosives and related compounds", *Proceedings of SPIE Volume: 5790,* Terahertz for Military and Security Applications III, May 18, 2005

[99] M. Daneshmand, S. Fouladi, R. R. Mansour, M. Lisi, and T. Stajcer, "Thermally actuated latching RF MEMS switch and its characteristics," *IEEE Transation. Microwave. Theory Techn.*, vol. 57, no. 12, pp. 3229–3238, Dec. 2009.

[100] R. Chan, R. Lesnick, D. Becher, and M. Feng, "Low-actuation voltage RF MEMS shunt switch with cold switching lifetime of seven billion cycles," *J. Microelectromech. Syst.*, vol. 12, no. 5, pp. 713–719, Oct. 2003.

[101] J. Leroy, A. Crunteanu, A. Bessaudou, F. Cosset, C. Champeaux, and J.-C. Orlianges, “High-speed metal-insulator transition in vanadium dioxide films induced by an electrical pulsed voltage over nano-gap electrodes,” *Appl. Phys. Lett.*, vol. 100, no. 21, pp. 213507-1–213507-4, May 2012.

[102] Y. Zhou, X. Chen, C. Ko, Z. Yang, C. Mouli, and S. Ramanathan, “Voltage-triggered ultrafast phase transition in vanadium dioxide switches,” *IEEE Electron Device Lett.*, vol. 34, no. 2, pp. 220–222, Feb. 2013.